

**ANALYSIS OF OPTICAL SUBSYSTEM AND LINKS USING  
STATISTICAL AND MACHINE LEARNING METHODS**

A Dissertation  
Presented to  
The Academic Faculty

by

Daniel Lippiatt

In Partial Fulfillment  
of the Requirements for the Degree  
Doctor of Philosophy in the  
School of Electrical and Computer Engineering

Georgia Institute of Technology  
May 2024

**COPYRIGHT © 2024 BY DANIEL LIPPIATT**

# ANALYSIS OF OPTICAL SUBSYSTEMS AND LINKS USING STATISTICAL AND MACHINE LEARNING METHODS

Approved by:

Dr. Stephen E. Ralph, Advisor  
School of Electrical and Computer  
Engineering  
*Georgia Institute of Technology*

Dr. Linke Guo  
Holcombe Department of Electrical and  
Computer Engineering  
*Clemson University*

Dr. John Barry  
School of Electrical and Computer  
Engineering  
*Georgia Institute of Technology*

Dr. Sorin Tibuleac  
System Architecture  
Adtran

Dr. David Anderson  
School of Electrical and Computer  
Engineering  
*Georgia Institute of Technology*

Date Approved: April 12, 2024

“Science is the acceptance of what works and the rejection of what does not.

That needs more courage than we might think.”

*Jacob Bronowski*

## ACKNOWLEDGEMENTS

While the journey has been challenging, it is through these experiences that you are forced to grow the most – this process has served as a catalyst for transformation, pushing me beyond my limits and encouraging changes that extend far past the confines of academia. I would like to express my sincerest gratitude to everyone who has played a role in the completion of this Ph.D. dissertation as I would not be here without all of you.

First and foremost, I am deeply thankful to my advisor, Dr. Stephen E. Ralph, for granting me the privilege to learn from him. His guidance, expertise, and support has been instrumental in both my academic growth and direction of this research. The valuable advice and insights have not only aided in this research but have also played a pivotal role in enhancing my overall capabilities as a researcher.

I am also grateful to the members of my dissertation committee, Dr. John Barry and Dr. David Anderson, for their insightful commentary and constructive criticisms which have guided and enhanced this work. I am thankful that Dr. Linke Guo took time out of his schedule and agreed to be my external committee member. I would like to extend further thanks to Dr. Sorin Tibuleac as he was not only a committee member, but also a central figure during the entirety of my research. My research benefited tremendously from his expertise as it ensured that the work was practical and worth pursuing.

I would like to acknowledge my colleagues Alex Kaylor, Arjun Khurana, and Joel Slaby for their aid. I am thankful for Dr. Siddharth Varughese who supported the beginning of my journey to a Ph.D., setting me up for success. Thanks to Dr. Varghese A. Thomas for his assistance whenever he was asked. The Chick-Fil-A Friday's with Dr. Jerrod Langston and Dr. Justin Lavrencik made the end of each week something to look

forward to. Additionally, I would like to thank Dr. Alirio Melgar, Dr. Hyung Joon Cho, and Dr. Gareeyasee Saha for the good times we shared during our respective journeys.

While my colleagues were crucial to this process, I cannot go without also expressing heartfelt appreciation to my all my friends and family who made this journey what it was, providing ample amounts of love and distractions to keep me sane. Jesse Balsiger who has gone from undergraduate roommate and gym partner to lifelong friend, Cody Achord who has always had an open ear, Christopher Ahn who was always eager to hang out, Daniel Garon for always being someone to debate which team would win the College Football Playoffs. My local RuneScape friends Paul Strapp and Christian “McRibs Back” Dodson for always supplying good vibes.

The unwavering encouragement, understanding, unconditional love from my parents and grandfather has been monumental in reaching my goals. Without their support, I would never have reached this far – from a first-generation college student to the completion of this Ph.D. dissertation. Their excitement at this achievement means the world to me.

Last but certainly not least, I would like to express my deepest gratitude to the love of my life, Alicia Nesmith. She has been my rock, my confidante, and my greatest cheerleader. Her beliefs in my abilities, even when I had doubts, have been a guiding light that has steered me to the completion of this Ph.D. Through many late nights, she stood by with patience and resilience that is beyond commendable. Her sacrifices did not go unnoticed, and her presence made even the most challenging moments bearable. She has not only witnessed the evolution of this dissertation, but has been an integral part of the narrative, shaping its pages with love and understanding.

# TABLE OF CONTENTS

<b>ACKNOWLEDGEMENTS</b>	<b>iv</b>
<b>LIST OF TABLES</b>	<b>viii</b>
<b>LIST OF FIGURES</b>	<b>ix</b>
<b>LIST OF SYMBOLS AND ABBREVIATIONS</b>	<b>xiv</b>
<b>SUMMARY</b>	<b>xviii</b>
<b>CHAPTER 1. INTRODUCTION</b>	<b>1</b>
<b>CHAPTER 2. BACKGROUND INFORMATION</b>	<b>4</b>
<b>2.1 Historical Overview of Fiber Optical Networks</b>	<b>4</b>
2.1.1 The Deployment of First-Generation Optical Networks	6
2.1.2 Amplifiers and Dispersion Management for Optical Networks	8
2.1.3 Coherent Optical Networks and Digital Signal Processing	11
<b>2.2 Fiber Optic Components and Hardware</b>	<b>14</b>
2.2.1 Optical Transmitters	15
2.2.2 Optical Fiber	20
2.2.3 In-Transit Optical Devices	32
2.2.4 Optical Receivers	36
<b>2.3 Digital Signal Processing for Optical Networks</b>	<b>42</b>
2.3.1 Transmitter-Side DSP for Coherent Optical Networks	42
2.3.2 Receiver-Side DSP for Coherent Optical Networks	46
<b>2.4 Machine Learning</b>	<b>56</b>
2.4.1 History of Machine Learning	56
2.4.2 Machine Learning Basics	59
2.4.3 Types of Machine Learning Algorithms	67
<b>CHAPTER 3. MACHINE LEARNING FOR TDECQ: ACCELERATING PAM-4 TRANSCEIVER CHARACTERIZATION</b>	<b>78</b>
<b>3.1 Methodology</b>	<b>79</b>
3.1.1 Experimental Setup	79
3.1.2 Machine Learning Architecture	83
<b>3.2 Results</b>	<b>86</b>
3.2.1 TDECQ Estimation via 2D-CNN	86
3.2.2 TDECQ Estimation via 1D-CNN	88
3.2.3 Impairment Identification via 2D-CNN	88
<b>3.3 Impairment Dependence for ML Performance</b>	<b>93</b>
<b>3.4 Oscilloscope Dependence for ML Performance</b>	<b>93</b>
3.4.1 Transfer Learning for Oscilloscope-Specific TDECQ Estimation	95
<b>3.5 Computational Complexity for TDECQ Estimation</b>	<b>98</b>

<b>CHAPTER 4. OPTICAL NETWORK MONITORING AND MANAGEMENT USING THE DIGITAL COHERENT RECEIVER</b>	<b>100</b>
<b>4.1 DSP Architectures with ML-Based Monitoring</b>	<b>102</b>
<b>4.2 Conventional Monitoring Parameters for Fiber Optic Networks</b>	<b>104</b>
4.2.1 Linear Noise in Optical Networks	104
4.2.2 Nonlinear Noise in Optical Networks	105
4.2.3 Generalized OSNR in Optical Networks	106
<b>4.3 Optical Performance Monitoring via Carrier Phase Recovery</b>	<b>107</b>
4.3.1 Methodology	107
4.3.2 Experimental Setup	110
4.3.3 Machine Learning Architecture Overview	112
4.3.4 Results	113
<b>4.4 Optical Performance Monitoring via Constellation Diagrams</b>	<b>115</b>
4.4.1 Experimental Setup	115
4.4.2 Machine Learning Architecture Overview	117
4.4.3 Results	118
<b>4.5 Impairment Detection and Identification for Fiber Optic Networks</b>	<b>120</b>
4.5.1 Experimental Setup and ML Architecture	121
4.5.2 Results	123
<b>CHAPTER 5. CONCLUSIONS</b>	<b>127</b>
<b>APPENDIX A. TRANSMITTER AND DISPERSION EYE CLOSURE QUATERNARY</b>	<b>130</b>
<b>REFERENCES</b>	<b>133</b>

## LIST OF TABLES

Table 2.1	General assumptions for photodiode noise model	38
Table 3.1	TDECQ Computational Complexity	99

## LIST OF FIGURES

- Figure 2.1 Bitrate-distance product evolution between 1840-2020 for communication systems. The evolution is plotted relative to key technological advancements. The invention of optical fibers and subsequent optical networking advancements facilitated a period of rapid growth [3]. 5
- Figure 2.2 Diagram of laser structure consisting of a pump source, gain medium, and optical resonator. Pump source adds energy to the system while the gain medium and optical resonator enhance the output optical beam. 16
- Figure 2.3 (a) Mach Zehnder Interferometer structure where intensity variations are generated via phase-induced constructive and destructive interference between the two different branches. (b) IQ modulator constructed using two MZIs and a phase shifter. IQ modulators are used to create advanced modulation formats. 18
- Figure 2.4 Transfer function for an MZI. Biasing the modulator to operate at the quadrature point enables both efficient and linear operation of the modulator. Quadrature biasing is such that it is biased at the voltage which corresponds to a phase shift of  $\pi/2$ . 19
- Figure 2.5 Cross-sectional diagram of a typical step-index optical fiber. The core is surrounded by cladding which has a slightly lower refractive index than the core (to abide by the principles of total internal reflection). Jacket layers are often included to protect the optical fiber from outside elements but do not affect its optical properties. 20
- Figure 2.6 Spectral loss profile of single-mode fiber for fundamental loss mechanisms such as Rayleigh scattering, and intrinsic absorption characteristics associated with electronic and vibrational resonances [36]. 26
- Figure 2.7 Noise as a function of incident optical power for a PIN photodiode. For low incident optical power, thermal noise dominates while for higher powers, shot noise dominates at the receiver. However, note that RIN noise dominates shot noise for high power systems under these constraints. 38
- Figure 2.8 (a) Balanced IQ coherent receiver constructed from power splitters (PS), directional couplers (DC), phase shifters ( $\pi/2$ ), and photodiodes (PD). 2x4 90° Hybrid architecture is shown. (b) Dual polarization IQ coherent receiver architecture which uses a combination of 2x4 90° hybrids and polarization beam splitters (PBS) to jointly receive the X and Y polarizations. 39
- Figure 2.9 Spectral depiction of single-carrier and multi-carrier formats [58]. Single-carrier formats utilize a single high baudrate signal while multi- 44

carrier formats use multiple lower baudrate signals to carry the data.

Figure 2.10	Examples of geometrically shaped 16QAM constellations [60].	45
Figure 2.11	Figure 2.11: Block diagram for frequency estimation algorithm for PSK modulation formats where $N$ is the number of constellation points (e.g., for QPSK, $N = 4$ ).	53
Figure 2.12	Training and validation example for ML algorithms. Underfitted models exhibit higher training error but relatively low validation accuracy while overfitted models exhibit low training accuracy but relatively high validation accuracy. Optimal fitting results in moderately low training error while maximizing validation accuracy [108].	61
Figure 2.13	Relationship between model capacity and generalization error for ML models. Generalization error is composed of bias and variance errors. Optimal capacity is the point in which these metrics are jointly minimized [108].	64
Figure 2.14	Polynomial regression fitting example using quadratic data and an ML model with degree 9. The regularization hyperparameter enables the over-capacity model to sufficiently fit the data as it controls the degree of learning possible [108].	65
Figure 2.15	FFNN with two hidden layers. Each node in the hidden and output layers acts as an activation function, or nonlinear transformation. Inputs of each hidden and output layer are a weighed multiplication of all outputs from the previous layer.	71
Figure 2.16	Activation functions used in ML. Selecting the correct activation function depends on the application. ReLU generally demonstrates sufficient performance and is most often used today. Swish is a lesser-known activation function discovered by researchers at Google with advantages over ReLU in deeper networks.	72
Figure 2.17	Typical CNN structure which maps from an $N$ -dimensional input to a feature map via convolutions, nonlinear transformations, and pooling. Feature maps are then used as the input to a FFNN to generate a relationship between these feature maps and the parameter of interest.	73
Figure 2.18	Structure of an LSTM cell. There are three main logic gates. The forget gate, depicted in blue, decides if information is passed to the cell state, $C_i$ . The input gate, labeled orange, quantifies the importance of new information. The output gate, shown in green, determines the output of the LSTM cell based on the cell state.	76
Figure 3.1	(a) The experimental setup consists of transmitter configured to emulate a variety of impairments, (b) example eye-diagrams from a real-time and equivalent-time oscilloscope from similar setup configurations. Quantization effects are visible in the real-time eye-diagram. Note that intermediate values are interpolated for eye-diagram plots.	80

Figure 3.2	Examples eye-diagrams impacted by impairments with varying severity: (a) bandwidth limitations which was generated using a filter at the transmitter, (b) signal compression which resulted from improper MZM biasing, (c) SNR degradations by digitally loading AWGN.	82
Figure 3.3	(a) Two-dimensional CNN architecture which uses eye-diagrams as input. The input image is an 80x160 matrix representing a histogram of the captured eye diagram. (b) One-dimensional CNN architecture which uses the digitally acquired waveform as the input. The raw waveforms consisted of consisted of 262,140 samples which correspond to an oversampling rate of 8.	85
Figure 3.4	Performance comparison between real- and equivalent-time oscilloscopes for eye-diagram-based TDECQ estimation. Equivalent-time oscilloscope demonstrates a better average performance for entire tested TDECQ range.	87
Figure 3.5	Performance comparison between real- and equivalent-time oscilloscopes for the signal-based TDECQ estimation demonstrating equivalent performance between the two oscilloscopes.	89
Figure 3.6	Confusion matrix depicting 100% impairment identification accuracy for the eye-diagram-based approach when TDECQ is greater than 3 dB. Bandwidth limitations, signal compression, and SNR limitations were all accurately identified. Note that 3 dB is the TDECQ threshold for compliance.	90
Figure 3.7	Impairment identification accuracy for real- and equivalent-time oscilloscopes when using the eye-diagram-based approach. All three emulated impairment types were jointly tested as a function of minimum TDECQ. The eye-diagram and waveform approaches demonstrated negligible performance differences, thus only one is shown.	91
Figure 3.8	(a) TDECQ estimation results for CNN trained on one impairment and tested on multiple impairments. Demonstrates good accuracy for trained impairments while untrained impairments show little correlation between measured and estimated TDECQ. (b) TDECQ estimation results for CNN trained and tested on all impairments. Demonstrates good accuracy for all tested cases.	92
Figure 3.9	Demonstration of scope-specific noise characteristics for equivalent-time trained, real-time tested cases for the (a) eye-diagram method where quantization effects have a discernible effect on accuracy, (b) waveform method where quantization effects have minimal impact. Note that both cases have an inherent offset which corresponds to the inherent noise characteristics of the oscilloscope which the ML algorithm learns during training.	94
Figure 3.10	(a) Equivalent-time oscilloscope TDECQ estimation using real-time oscilloscope trained ML. Increased error based on the inherent noise characteristics of the real-time oscilloscope. (b) Equivalent-time	96

oscilloscope TDECQ estimation using transfer-learning-based ML. Original CNN was initialized to a real-time oscilloscope dataset but retrained with a small subset of equivalent-time data.

Figure 3.11	Transfer learning model accuracy scaled by number of files used to train the CNN. Model accuracy within 0.25 dB after using only 25 training waveforms. Model approaches expected accuracy metrics after only 100 waveforms and thus requires a dataset that is ~10% of the original network.	97
Figure 4.1	Conventional demodulation flowchart for a long-haul coherent optical link	102
Figure 4.2	OSNR measurement using an OSA. Noise floor is estimated via the out-of-band noise. Conventionally, signal and noise power are integrated within a 0.1 nm band. Other integration	105
Figure 4.3	Demonstration of (a) the carrier phase estimate from a conventional CPR algorithm for OSNR of 11, 15, and 19 dB, (b) the resulting differential phase from each of the carrier phase estimates to be used as the feature of interest, (c) the autocorrelation of three differential phases with varying launch powers.	108
Figure 4.4	(a) Experimental setup used for verifying the proposed technique. The setup employed a 3-channel 32 Gbaud DP-QPSK signal over 270 km of SSMF. OSNR was varied via ASE noise loading, (b) example of channel spacing used for OSNR measurement, (c) demonstration of nonlinear penalties associated with increasing launch power for 12 dB OSNR.	111
Figure 4.5	Simple FFNN with one hidden layer used to jointly estimate the linear and nonlinear noise. The input features are the first 50 coefficients of the autocorrelation from the differential phase noise as well as the RMS value of this phase noise metric.	112
Figure 4.6	Minimum, average, and maximum error results for the proposed technique. Various test cases are shown: OSNR estimation error for launch power (a) 3 dBm, (b) 6 dBm, and (c) 9 dBm. Launch power estimation error for OSNR (d) 11 dB, (e) 15 dB, and (f) 19 dB.	114
Figure 4.7	(a) Experimental setup which consists of 8 spans used to collect data for training and testing the CNN to estimate OSNR, GOSNR, and BER. (b) Example constellation density with 60,000 symbols demonstrating common laboratory test conditions, (c) example commercial constellation density with 6,144 symbols scaled to the 60,000-symbol constellation.	116
Figure 4.8	CNN architecture consisting of three FEL and three FCL. There is an implied leaky rectified linear unit between convolution and pooling layers to generate a nonlinear mapping. The input image is a constellation density plot. The same architecture was used for OSNR,	118

GOSNR, and BER estimation.

Figure 4.9	CNN estimation accuracy for both QPSK and 16-QAM modulation formats when trained on eight configurations which span a variety of linear noise and nonlinear noise conditions. (a) BER estimation accuracy, (b) GOSNR estimation accuracy, (c) OSNR estimation accuracy.	119
Figure 4.10	Waveform clipping to emulate saturated amplifier nonlinearities. Waveforms were clipped on both in-phase and quadrature components. Clipping amount was varied as a percentage of the max.	122
Figure 4.11	Constellation density plots for fiber and amplifier nonlinearities. Both constellations exhibit EVM of $\sim 18.2\%$ and BER of $\sim 7 \times 10^{-3}$ . Visually apparent statistical density differences on a per-cluster basis are observed.	123
Figure 4.12	Confusion matrix for identifying amplifier and fiber nonlinearities. Impairment identification accuracy of 100% was demonstrated in this scenario.	124
Figure 4.13	Clipping estimation accuracy for constellation-based ML method. Accurate average estimation within $\pm 3.8\%$ was demonstrated.	125
Figure 4.14	Clipping estimation accuracy as a function of varying clipping percentage. Clipping estimation becomes less accurate as clipping decreases. (b) Clipping estimation accuracy as a function of LP. No dependence is shown.	126
Figure A.1	Algorithmic flow chart for TDECQ measurements. PAM-4 transmitters are qualified relative to the amount of additional noise needed to reach a target SER.	130
Figure A.2	Example sequences from SSPRQ pattern used to calculate the OMA. The central symbol of each batch is used as the minimum and maximum amplitudes [148].	132
Figure A.3	Example of PAM-4 eye-diagram used to calculate the SER for TDECQ measurements [148]. Important metrics such as left and right histograms are shown.	132

## LIST OF SYMBOLS AND ABBREVIATIONS

1D-CNN	One-dimensional CNN
ASE	Amplified spontaneous emission
ASIC	Application-specific integrated circuit
AWG	Arbitrary waveform generator
AWGN	Additive white Gaussian noise
BER	Bit error rate
BSS	Blind source separation
CD	Chromatic dispersion
CMA	Constant modulus algorithm
CNN	Convolutional neural network
DAC	Digital-to-analog converter
DBP	Digital backpropagation
DNN	Deep neural network
DSCM	Digital subcarrier multiplexing
DSF	Dispersion shifted fiber
DSP	Digital signal processing
DMT	Discrete multi-tone
EDFA	Erbium-doped fiber amplifier
ENoB	Effective number of bits
EVM	Error vector magnitude
FCL	Fully connected layer
FEC	Forward error correction
FEL	Feature extraction layer
FFT	Fast Fourier transform

FFNN	Feedforward neural network
FWM	Four-wave mixing
GaAlAs	Gallium aluminium arsenide
GN	Gaussian noise
GOSNR	Generalized optical signal-to-noise ratio
GS	Geometric shaping
ICA	Independent component analysis
IOT	Internet of things
I/Q	In-phase/Quadrature
ISI	Intersymbol interference
LMS	Least mean square
LO	Local oscillator
LSTM	Long short-term memory
ML	Machine learning
MMA	Multi-modulus algorithm
MMF	Multimode fiber
MSE	Mean square error
MZI	Mach-Zehnder interferometer
NLSE	Nonlinear Schrödinger equation
OSA	Optical spectrum analyzer
OSNR	Optical signal-to-noise ratio
OFDM	Orthogonal frequency-division multiplexing
PAM	Pulse amplitude modulation
PBS	Polarization beam splitter
PCA	Principal component analysis
PDL	Polarization dependent loss

PDM	Polarization-division multiplexing
PS	Probabilistic shaping
PSK	Phase shift keying
QAM	Quadrature amplitude modulation
QoT	Quality of transmission
QPSK	Quadrature phase shift keying
ReLU	Rectified linear unit
RIN	Relative intensity noise
RNN	Recurrent neural network
ROADM	Reconfigurable optical add-drop multiplexer
RRC	Root raised cosine
SDM	Space division multiplexing
SER	Symbol error rate
SNR	Signal-to-noise ratio
SPM	Self-phase modulation
SSFM	Split-step Fourier method
SSMF	Standard single mode fiber
SSPRQ	Short stress pattern random quaternary
SVM	Support vector machine
TDECQ	Transmitter and dispersion eye closure quaternary
TD-HMF	Time-domain hybrid modulation formats
TDM	Time division multiplexing
TDP	Transmitter and dispersion penalty
TR	Timing recovery
VC	Vapnik Chervonenkis
VOA	Variable optical attenuator

WDM Wavelength division multiplexing

WSS Wavelength-selective switch

XPM Cross-phase modulation

## SUMMARY

The internet has seen exponential growth of traffic demands in recent years as internet access has become more available and device connectivity has become an integral portion of the global market (e.g., “Internet of Things”). Optical networks serve as the backbone of the internet’s infrastructure and thus have received tremendous funding related to both deployment as well as research and development. To meet these increasing traffic demands, optical networks have continued to push the boundaries in terms of reach and data rates. This growth has been supported by the ongoing development of a variety of technologies such as optical amplifiers and optical filters as well as applications of these technologies such as wavelength division multiplexing. Likewise, computing power has increased and become more cost effective which has enabled the use of powerful digital signal processing algorithms to digitally compensate for optical impairments which previously limited link performance. However, performance monitoring of modern optical links has become a concern due to the increased complexity that results from these improvements – traditional monitoring methods have become obscured or difficult to realize. The objective of this research is to develop performance monitoring techniques for next generation optical subsystems and links that estimate key device and network parameters, identify the major impairments limiting performance, and localize these impairments to specific devices or locations within the optical link.

## INTRODUCTION

Data demands have grown exponentially since the inception of the internet. This trend is expected to continue as internet access becomes increasingly available and crucial to modern society. Projections indicate that the total internet users have increased from 3.9 billion to 5.3 billion users within the last 5 years [1]. Likewise, the meteoric rise of smart devices coupled with concepts such as the Internet of Things (IoT) has driven the market into further unprecedented connectivity: it is predicted that there will be a total of 500 billion devices connected to the internet by 2030. These demands have necessitated the rapid development of fiber optic networks which serve as the backbone of the internet: from record research demonstrations of 1 Tb/s in 1996 to commercial implementations of over 50 Tb/s in 2018 [2]. Many advancements in the last 20 years have contributed to this efficient increase of network throughput: wavelength division multiplexing (WDM), digital signal processing (DSP), advanced modulation formats as well as a plethora of crucial hardware-specific developments such as the erbium-doped fiber amplifier (EDFA), and application specific integrated circuits (ASICs).

The complexity of these modern optical networks has resulted in a multitude of challenges. As data rates have increased and system margins have shrunk, the impact of system impairments has been exacerbated which has created a dependence on performance monitoring to ensure reliable network operation. However, conventional techniques for measuring performance may no longer be possible and evaluating the performance of specific components has become difficult due to the interconnected nature of the electrical and optical domains alongside compensatory DSP. The objective

of this research is to lay the framework to solve these issues using statistical and machine learning based methodologies to monitor key performance metrics of next generation optical networks while identifying major impairments that are degrading the system performance. This extends from link level analysis to component performance monitoring to enable full-system characterization.

The PhD dissertation is organized into five chapters. Chapter 2 reviews relevant background information necessary to understand the works here within. A brief history of optical networks is presented to give context to the work and emphasize the continuing growth of optical networking. The theory behind the operation of optical devices and how they fit into an optical network is shown with an emphasis on potential impairments that may result from each. Similarly, a description of conventionally used DSP algorithms is explored to highlight the current approaches for compensating specific impairments. Lastly, an overview of machine learning (ML) is presented which covers the historical relevance, basic principles of operation, and common ML algorithms used. As a review of well-established concepts, Chapter 2 does not claim novelty and is thus heavily inspired by other works.

Chapter 3 is a presentation of ML-based transmitter and dispersion eye closure quaternary (TDECQ) estimation methods which also serves as an impairment identification paradigm. The ML-based method provides advantages over the traditional method to calculate TDECQ – an IEEE standard for qualifying PAM-4 transmitters. TDECQ is a computationally intensive algorithm which requires a considerable time investment. This work heavily accelerates this calculation while also identifying common transmitter impairments to enable manufacturers to rapidly pinpoint product defects. Eye-

diagram-based and signal-based approaches are both demonstrated to allow for flexibility in implementation depending on what is available: eye-diagrams are already required for the traditional TDECQ method while signal analysis allows for marginally increased accuracy.

Chapter 4 discusses optical performance monitoring techniques for long-haul coherent optical networks. Coherent optical networks serve as the backbone of the internet and thus span hundreds of kilometers while serving various locations; however, as data rates have increased, the system margins have decreased which are necessary to ensure consistent operation. Monitoring specific link parameters such as the optical signal-to-noise ratio allows network operators to gauge the health of the system – these metrics are becoming increasingly difficult to access. Here, ML-based approaches for monitoring such network parameters are shown. These techniques leverage information readily available from conventional DSP. Impairment identification for these links is also discussed with examples. Device-level impairment identification is demonstrated with limitations of such methods noted.

Finally, chapter 5 draws conclusions from the works in this dissertation while reviewing key findings and concepts presented in chapters 3 and 4. Potential avenues for continuing research are highlighted. The appendix details the IEEE standard for calculating the TDECQ of PAM-4 transceivers which is a crucial background component for chapter 3.

## **BACKGROUND INFORMATION**

### **2.1 Historical Overview of Fiber Optical Networks**

Whether it was by using fires or even reflections of sunlight from reflective materials, light has seen its uses as a method of communication throughout human history. Lighthouses are one famous example dating back as far as over 2,000 years ago with one of the Seven Wonders of the Ancient World, the Pharos of Alexandria. However, technological progress did not see many strides in long distance communication using light until the 1790s when the French engineer Claude Chappe invented the “optical telegraph” which used relay towers (i.e., repeaters) to visually identify coded symbols between these stations to transmit information [3]. By 1830, these stations, which were positioned across Europe, constructed what might be considered the first long-haul optical network.

The optical telegraph was a short-lived technology due to the advent of the electrical telegraph in the 1840s which saw use until the mid-20<sup>th</sup> century [4]. The electrical telegraph allowed for data transmission at a rate of multiple bits per second unlike the optical telegraph which had rates slower than 1 bit per second. Electrical communication dominated for 100 years due to the invention of key technologies such as the telephone and motivated progress into many different research fields such as microwave electronics to continually improve data rates.

By the 1950s, electrical communication methods were approaching technical limitations with balancing reach and data rate. This brought attention back towards optical communication as a potential means to alleviate these issues; however, this was hindered by limitations in available technologies until the 1970s. The invention of the laser in 1960 was one half of the puzzle as it served as a coherent source [5]. The

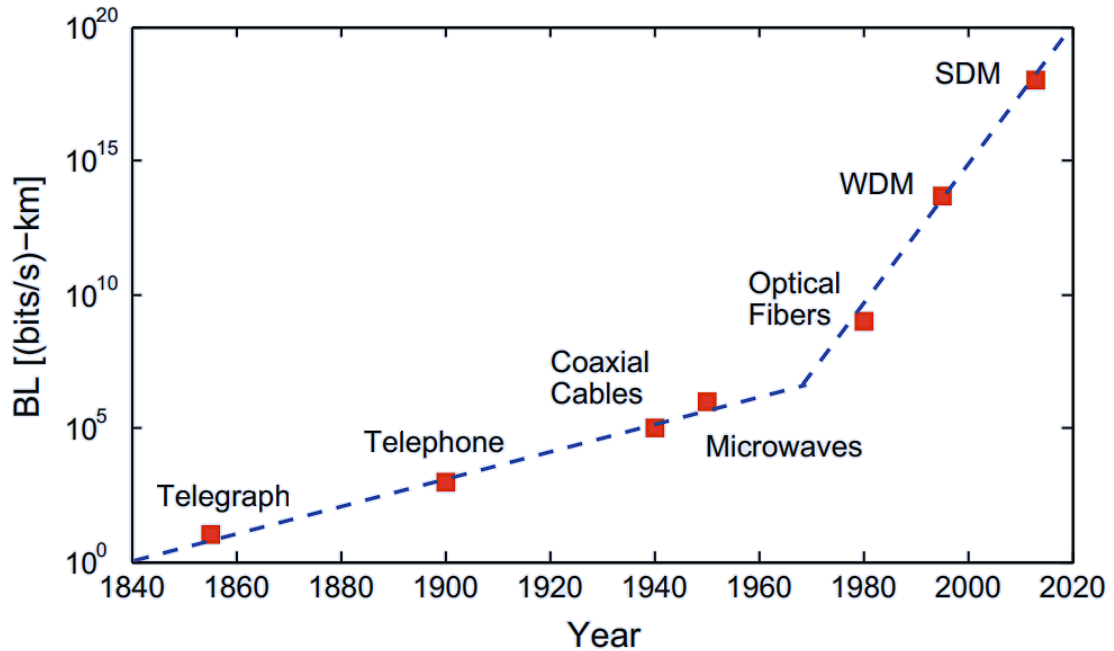


Figure 2.1: Bitrate-distance product evolution between 1840-2020 for communication systems. The evolution is plotted relative to key technological advancements. The invention of optical fibers and subsequent optical networking advancements facilitated a period of rapid growth [3].

invention of the optical fiber, also invented in the 1960s, was the other missing piece as it served as the transmission medium. However, optical fiber was too lossy for long distance transmission. This changed when Corning reduced fiber losses to below 20 dB/km in 1970 [6]. Improvements in fiber loss continued until 1979 when a group of Japanese scientists managed to reduce the loss to nearly 0.2 dB/km – a value which is still comparable to modern optical fiber [7].

The combination of these two advancements led to rapid development of optical communication systems and facilitated the first modern fiber optic networks which demonstrated much higher reach and data rates than the previous electrical communication systems. The bitrate-distance product of a variety of technologies including optical fibers is shown in Fig. 2.1. Supporting technologies such as WDM, space division multiplexing (SDM), advanced modulation formats as well as the

transition from direct detect to coherent detection with enabling DSP have allowed fiber optic networks to continually improve the data throughput over the last 50 years: modern optical networks have managed to reach data rates over 50 Tb/s in a single fiber [1] which is a large improvement from the less than 1 b/s supported by the original optical telegraph.

In the following sections, a more in-depth history of optical networking is discussed regarding the scaling capacity of these networks with an emphasis on certain technological breakthrough points which facilitated this growth. The breakthroughs which will be discussed in detail include inventions such as the optical amplifier, different fiber types, and receiver technologies as well as techniques such as wavelength division multiplexing and digital signal processing. A brief look at the future of optical networking is also discussed with an emphasis on the rising role of machine learning in today's optical networks.

### *2.1.1 The Deployment of First-Generation Optical Networks*

American Telephone and Telegraph (AT&T) deployed one of the earliest fiber optic network tests in 1977 [8]. In the “Atlanta System Experiment,” a fiber array composed of 144 fibers was deployed through 648 meters of fiber. The experiment was designed to simulate realistic field conditions by routing the fiber through underground ducts. The result of this study paved the way for optical networks to become practical telecommunication equipment as it evaluated the performance of realistic network conditions and modelled important system parameters such as fiber crosstalk, fiber dispersion, and timing jitter.

Within months of this preliminary experiment, companies around the world had already begun deploying live telephone traffic via multimode fiber (MMF). General Telephone and Electronics (GTE) deployed a network at 6 Mbps in Long Beach, California while the United Kingdom Post Office deployed a network near Martlesham Heath, UK operating at 8.4 Mbps [9-11]. AT&T deployed an optical link operating at 44.7 Mbps during what is known as “the Chicago Lightwave Communications Project.” This project was a follow up to the “Atlanta System Experiment” as a majority of the equipment from that test was shipped and used within this optical link. The network transmitted commercial traffic for the first time on April 1, 1977, and this traffic included voice, analog data, digital data as well as other services. The system operated at a wavelength of 820 nm as it used gallium aluminium arsenide (GaAlAs) lasers. The average fiber loss for the system at this wavelength was 5.1 dB/km. Overall, this project was a huge success as it demonstrated not only high transmission speeds, but also the reliability of fiber optic networks – 99.999% of all transmission time was error free. A variety of other field trials occurred around the world concurrently and details of these trials can be found in [2].

Optical networks of this time were known as “direct detect regenerated systems.” The main limitation of these networks was the transmission distance – lossy fiber alongside no in-line optical amplifiers required networks to “regenerate” the signal along the signal path. Regeneration entailed receiving the signal, decoding it, re-encoding it using another transmitter, and sending this new signal along the optical path. This process made deploying long distance optical networks relatively expensive. This era of regenerated optical networks lasted roughly 16 years from 1977 to 1993 [12] and saw

many technological breakthroughs to alleviate these challenges and shortcomings thereby pushing optical networks to the forefront of telecommunication.

The original optical network trials which operated at wavelengths near 850 nm through MMF were short-lived because these networks were heavily limited in capacity. Laser manufacturers worked to increase the operating wavelengths to reduce fiber attenuation. Lasers operating at 1300 nm were first implemented in an optical system in 1981 and single-mode fiber, which was originally theorized by Elias Snitzer in 1961, was finally deployed in an actual system by 1982. Similarly, lasers operating at 1550 nm were developed. These breakthroughs facilitated a great increase in data throughput from 45 Mbps all the way to 1.7 Gbps. The first system transporting two signals encoded on separate wavelengths on a single fiber was demonstrated in 1989 with an aggregate data rate of 3.4 Gbps – serving as a precursor to the WDM systems of today. However, the capacity of these systems was ultimately limited by the transceiver interface rates as the signals required regeneration every 10 km. Likewise, research efforts at the time also demonstrated vast improvements over available commercial results with 10 Gbps experiments occurring in 1988, 16 Gbps in 1989, and 20 Gbps in 1991.

### *2.1.2 Amplifiers and Dispersion Management for Optical Networks*

The invention of the EDFA in the late 1980s provided a cost-effective solution for long-haul optical networks as it removed the need to regenerate the signal during transit [12]. The EDFA provided a plethora of benefits including high gain and low noise figure which enabled longer distance transmissions while maintaining sufficient signal quality as well as a broad bandwidth which was an important feature for the development of

WDM optical networks as it enabled the simultaneous amplification of multiple wavelengths via one device. For reference, the EDFA operated (and therefore supported wavelengths) within the range of 1530-1565 nm. This range of wavelengths is known as the C-band.

However, the widespread deployment of EDFAs did not come without its own challenges. The combination of longer transmission distances and moving towards systems operating at 1550 nm resulted in chromatic dispersion becoming a limiting factor for signal quality. Chromatic dispersion is an optical phenomenon which is defined by different wavelengths of light arriving at their destination at slightly different times which limits the bandwidth. This effect largely occurs since there is a wavelength dependence with respect to the refractive index of optical fiber. Available fiber types at that time demonstrated large chromatic dispersion coefficients. For example, standard single mode fiber (SSMF) has a dispersion coefficient of 17 ps/nm/km at 1550 nm which resulted in rapid accumulation of the effect. Chromatic dispersion limited the reach of 10 Gbps signals to ~60 km.

Dispersion shifted fiber (DSF) was developed to get rid of the chromatic dispersion issues that were occurring in the C-band. DSF was specifically designed with a certain refractive index profile that shifted the zero-dispersion wavelength from 1300 nm region (such as in SSMF) to the 1550 nm region. It was demonstrated in the early 1990s that DSF was able to extend the reach of 10 Gbps signals to upwards of thousands of kilometers which resulted in widescale deployment primarily in Japan and some parts of North America. However, this was shown to be a mistake when the optical networks were extended to multiple wavelengths as low dispersion signals are extremely sensitive

to a nonlinear effect called four-wave mixing (FWM). FWM generates new interfering wavelengths by mixing nearby in-transit signals and is largely dependent on phase-matching between these neighboring channels – this condition occurs for low-dispersion signals.

A new fiber type called non-zero dispersion shifted fiber (or TrueWave fiber) was then developed in 1993 [13] to reduce the effects of FWM by being designed with a low amount of dispersion ( $\sim 2$  ps/nm/km) in the C-band. This eliminated the phase matching condition while maintaining most of the advantages of low dispersion. However, as data rates were pushed beyond 10 Gbps to upwards of 40 Gbps, TrueWave fiber still resulted in dispersion-limited systems. In the quest to remove this dispersion limitation, researchers discovered that another type of TrueWave fiber could be designed: fiber with a dispersion coefficient of  $-2$  ps/nm/km. This began the advent of dispersion-managed systems where systems were designed such that fibers of positive and negative dispersion coefficients were deployed with the intention of having non-zero dispersion locally to suppress FWM, but zero aggregate dispersion at the end of the link. One of the first demonstrations of a dispersion managed system occurred in 1993 where negative dispersion TrueWave fiber was used to correct for short SSMF spans [14].

Dispersion management became a crucial part of network design since it enabled high speed data transmissions across long distances. This led to the invention of dispersion compensating fiber [15-16] as this new fiber type supported a large negative dispersion which enabled more complex dispersion management as well as dispersion precompensation. Research in this period focused heavily on different types of dispersion mapping techniques as it enabled network operators to balance nonlinearities induced by

high launch powers which were crucial for maximizing the OSNR. In systems of this time, the most common dispersion map was such that equal amounts of dispersion compensation were applied periodically at a certain distance threshold – this type of dispersion map was called a “singly-periodic dispersion map” [17]. This type of mapping was preferred because it allowed for the development of simpler engineering rules compared to more complicated dispersion mapping techniques thereby simplifying the deployment process.

The era of dispersion managed systems which lasted roughly 16 years from 1993 to 2009 was supported by a variety of technologies: the EDFA enabled wideband amplification of over 80 wavelengths on a single fiber while DCFs enabled network operators to control the amount of dispersion during transmission. Optical networks had seen tremendous growth in throughput during this era: research demonstrated the first 1 Tbps transmissions in 1996 using a 50 channel WDM network. By the end of this era, commercial systems were able to support 80 wavelengths on a single fiber each operating at 40 Gbps.

### *2.1.3 Coherent Optical Networks and Digital Signal Processing*

As network operators maximized the available bandwidth of the EDFA, it was no longer possible to continue increasing data rates by adding more wavelengths. Therefore, research trended towards increasing the spectral efficiency of each wavelength as the next logical step. Note that spectral efficiency is defined as the number of bits transmitted per second per some allocated bandwidth (measured in bits/s/Hz). The implementation of advanced modulation formats was one driving technique to increase the spectral

efficiency [18]. Quadrature phase shift keying (QPSK) modulation was one such modulation format which was initially deployed for this purpose. QPSK allowed for the transmission of two bits per received symbol by encoding these bits on four different values of the signal phase with the distinct advantage of being readily compatible with the direct detect systems of that time.

Originally, coherent receivers were studied in the 1980s to increase transmission distance due to their increased receiver sensitivity [19]. However, this was negated by the invention of the EDFA since in-line optical amplification was then possible. Interest in coherent receivers returned in the early 2000s when coherent communication was proposed as a viable tactic to push data rates that were plateauing due to the limited fiber bandwidth by enabling progressively more advanced modulation formats. Coherent detection aimed to quadruple the data rate through fiber as it enabled both polarization diversity (encoding information independently on each polarization of the optical signal) and phase diversity (encoding information in the phase of the optical signal in terms of the in-phase and quadrature components) alongside the traditional amplitude modulation.

However, coherent communication truly began to gain traction due to advances in complementary metal oxide semiconductor processing alongside innovative ASIC designs during the early 2000s which led to the accessibility of faster analog to digital converters and digital to analog converters which increased the possible data rates for real-time systems while enabling the use of DSP to mitigate channel impairments such as chromatic dispersion (CD), polarization mode dispersion, and even nonlinear effects [20]. It also allowed for digital equalization.

In 2005, CD compensation using maximum likelihood estimation was demonstrated in a long-haul optical link for the first time [21] but suffered for commercial applications due to the high associated computational complexity. Therefore, researchers implemented digital linear filters to efficiently compensate for CD instead by using a combination of the coherent receiver and high-speed analog to digital converters. CD compensation removed the previous need for dispersion management in optical networks as digital compensation could be applied to any arbitrary amount of accumulated CD. Other similar simplifications by using DSP applied to a variety of other link impairments as well such as carrier phase differences and frequency offsets from the local oscillator at the coherent receiver. Since these impairments could be compensated digitally, link design became simplified and implementation barriers were removed as operators no longer needed to consider these parameters. Optical networks enjoyed a variety of benefits including increased transmission distance, performance, and data throughput.

Coherent networks also required less complex modelling methodologies to characterize the systems. The original detect-detect systems required computationally intensive split-step Fourier method (SSFM) simulations to accurately predict system performance with high accuracy. Meanwhile, coherent networks were able to use simple analytic and semi-analytic modelling methodologies such as the Gaussian Noise (GN) model which represents link distortions and impairments as an equivalent additive white Gaussian noise [22-25]. Likewise, modern optical networks have continued this analytical trend by researching other methods such as machine learning to further enhance both system modelling [26] and system performance predictions [27].

From 2004 until present day, coherent systems have continued to push the limits of system performance and data throughput via development of new techniques such as forward error correction (FEC) as well as the use of increasingly higher-order modulation formats: most modern coherent systems are developed with 4QAM, 16QAM, 32QAM, and 64QAM as the target formats, but research has also demonstrated modulation formats as high as 2048-QAM [28]. Likewise, the development of more efficient DSP algorithms alongside component-level performance improvements have enabled incredible advancements in interface rates between the coherent receiver and the electrical backend. Research data rates have scaled from 100 Gbps using 28 Gbaud DP-QPSK [29], 200 Gbps using 32 Gbaud DP-16QAM [30], and 400 Gbps using 56 GBaud DP-16QAM [31]. Coherent systems were even able to recently achieve 1 Tbps using 90 GBaud DP-64QAM in 2015 [32] resulting in modern optical experiments carrying traffic equivalent to an entire network in 1996 on one wavelength. Optical networks are now able to support 65 Tbps over 6000 km on a single fiber [33].

## **2.2 Fiber Optic Components and Hardware**

Fiber optical networks are supported by a variety of components, devices, and hardware which make not only the transmission of light across long distances possible, but also the encoding of high-speed information on this light feasible. The development and continual improvement of technologies such as lasers, optical fiber, modulators, amplifiers, filters, and photodiodes is significant for the deployment of all modern optical networks. Therefore, this section will develop the necessary framework to understand the role of these devices in an optical network, how these devices function, and common limitations which are related to these devices.

## 2.2.1 *Optical Transmitters*

Optical transmitters serve the role of converting an electrical input signal into an optical signal. To do this, individual components such as lasers, digital-to-analog converters (DACs), and modulators are used to generate a carrier signal and to encode information on the carrier. Here within, these components are discussed in detail.

### 2.2.1.1 Lasers

Lasers, devices which emit light, were first developed in 1960 by Theodore Maiman at Hughes Research Laboratories. They have become so ubiquitous that the acronym which originally stood for “light amplification by stimulated emission of radiation” is now known as its own word completely independent from its original meaning. Lasers are widely used in many different disciplines – they are implemented in many military and commercial products including laser printers, laser pointers, lidar, holograms, laser cutters, and countless others. Lasers have also been used to perform many medical procedures and surgeries such as laser eye surgery, scar removal surgeries, and cancer treatments. Most relevant to this work, lasers also serve as the major component of an optical transmitter by supplying an optical source which is used as the carrier for an information signal by encoding information onto it.

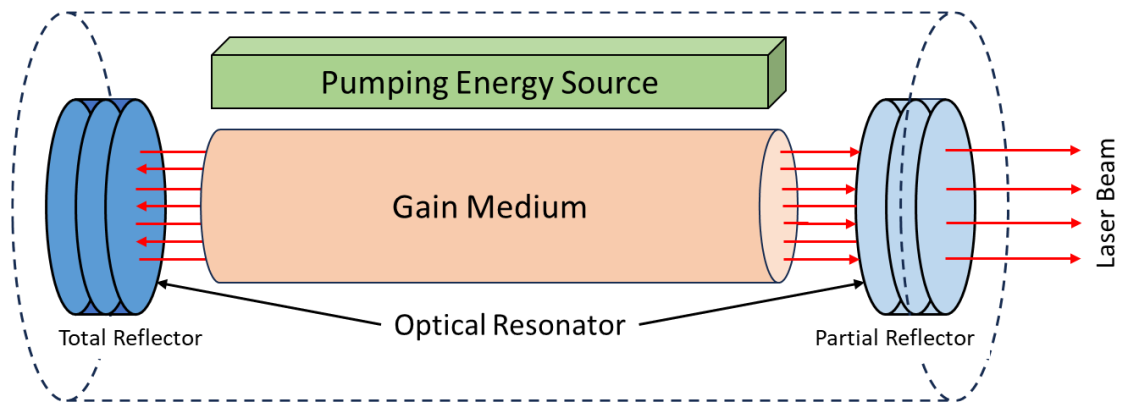


Figure 2.2: Diagram of a typical laser structure consisting of a pump source, gain medium, and optical resonator. Pump source adds energy to the system while the gain medium and optical resonator enhance the output optical beam.

The structure of a laser consists of a pump source, a gain medium, and two or more mirrors which form an optical resonator, Fig. 2.2. The pump source introduces energy into the gain medium from some external source. From this energy, excited energy states for atoms in the gain medium are produced which results in population inversion (defined as the state where the number of excited particles exceeds the number of low energy particles). When this condition is met, the rate of stimulated emission surpasses the rate of absorption in the material thereby allowing light emission to occur. The generated photons are then reflected in the optical resonator – the resonator stores photons within the medium to enhance the intensity of the output optical beam. Note that one end of the optical resonator is a fully reflecting mirror while the other is a partially reflecting mirror to allow for the optical resonator to direct the beam in a certain direction. The wavelength and output power of the laser can be designed by modifying the designs of these components.

### 2.2.1.2 Digital-to-Analog Converter

The information that needs to be transmitted is usually defined digitally and this is typically using a binary paradigm of 0s and 1s as the information bits. However, real world signals do not operate in a binary manner and are instead depicted as some physical phenomenon such as varying voltages. As such, a DAC is the device that is used to perform this conversion from a theoretical information signal to a physical signal. Unlike theoretical information signals, physical signals have limitations which define the performance of a DAC.

DAC performance is quantified by parameters such as the bit resolution, sampling rate, bandwidth, noise, and timing jitter. The bit resolution defines the number of output levels of the DAC – a 1-bit DAC has 2 possible output levels while a 4-bit DAC has 16 possible output levels. The bit resolution is directly related to the extremely relevant effective number of bits (ENoB) which measures the actual resolution of the DAC. According to the IEEE standard 1057, ENoB is defined as [34]

$$ENoB = \log_2 \left( \frac{FSR}{N_{rms} \sqrt{12}} \right) \quad (2.1)$$

where FSR is the full-scale range of the DAC voltage and  $N_{rms}$  is the rms noise voltage. The sampling rate of a DAC is limited to the speed that the internal electrical circuitry of the device can continue to produce correct outputs. This is largely defined by the Nyquist-Shannon sampling theorem and is thus dependent on the bandwidth. Noise and timing jitter are important impairments for DACs that limit the performance. Noise is

limited by thermal noise of the electrical components while timing jitter is how much a signal sampling deviates from a synchronized clock signal.

### 2.2.1.3 Modulators

Communication signals are often generated electrically and thus need to be converted to the optical domain for transport. Conventionally, modulators are used to perform this encoding from the electrical to optical domain by exploiting the Pockels effect [35] of electro-optical materials such as lithium niobate. Pockels effect is the phenomenon such that the refractive index of a material varies proportionally with an applied electrical field. By changing the refractive index, one can invoke differences in the phase of the optical signal – the components that enable this are called Mach-Zehnder interferometers (MZIs) and the transfer function of this component is

$$E_{out} = E_{in} \cos\left(\frac{\pi V_{in}}{V_{\pi}}\right) \quad (2.2)$$

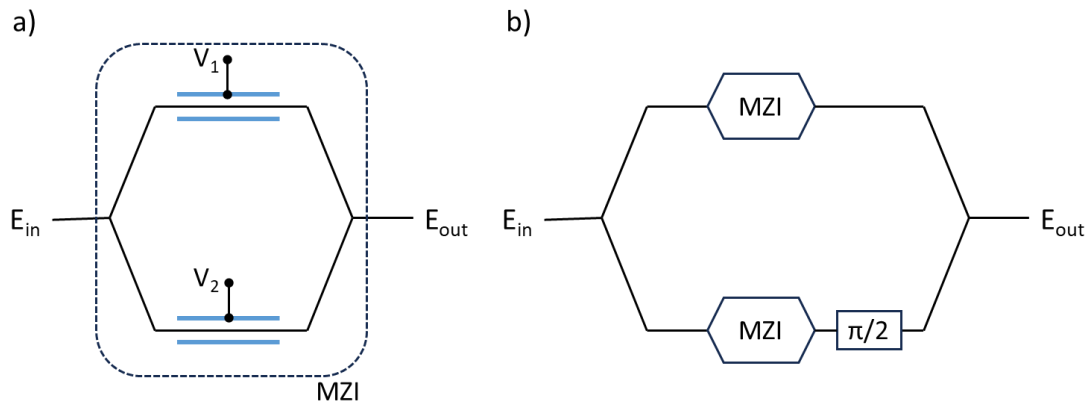


Figure 2.3: (a) Mach Zehnder Interferometer structure where intensity variations are generated via phase-induced constructive and destructive interference between the two different branches. (b) IQ modulator constructed using two MZIs and a phase shifter. IQ modulators are used to create advanced modulation formats.

where  $V_{in}$  is the input voltage of the electrical communication signal,  $V_{\pi}$  is the voltage necessary to induce a phase shift of  $\pi$ , and  $E_{in}$  and  $E_{out}$  are the input and output optical fields, respectively. Modern optical signals are complex and utilize both the in-phase and quadrature components of the signal to modulate across both amplitude and phase. MZIs can be combined in a structure such as Fig. 2.3 to also induce amplitude variations via interferometric interactions.

Since the transfer function of the MZI is sinusoidal, it can induce a nonlinear distortion onto the modulation signal. Therefore, the applied voltage  $V_{in}$  is usually limited to the linear regime as shown in Fig. 2.4 to limit these distortions. However, limiting the  $V_{in}$  can reduce modulation depth which reduces the effectiveness of modulation. It is an important design consideration to balance these effects to achieve optimal performance. Similarly, it is sometimes advisable to use an electrical amplifier, labelled as a driver

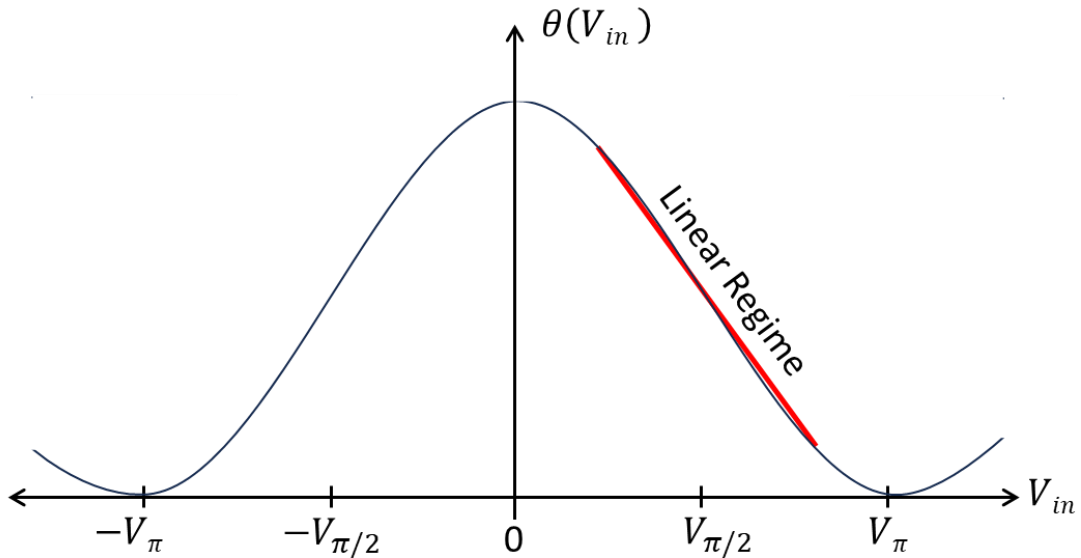


Figure 2.4: Transfer function for an MZI. Biasing the modulator to operate at the quadrature point enables both efficient and linear operation of the modulator. Quadrature biasing is such that it is biased at the voltage which corresponds to a phase shift of  $\pi/2$ .

amplifier, to increase the amplitude depth of  $V_{in}$  to thereby increase the modulation depth. The driver amplifier can induce nonlinearities and distortions to the signal which becomes another consideration when designing a proper modulator.

### 2.2.2 *Optical Fiber*

Optical signals generated by the transmitter are transported through hundreds of kilometers by optical fiber making it one of the most important components of an optical network. The following section thus focuses on the theory behind light propagation through optical fiber as well as common phenomenon and impairments associated with optical fiber. Special attention is given to standard SSMF as it is one of the most ubiquitous fiber types especially concerning long distance transmission.

#### 2.2.2.1 Light Propagation Principles for Optical Fibers

Light uses the principle of total internal reflection to propagate light through waveguides [36]. Total internal reflection is the phenomenon where light, when reaching the boundary between two materials, is completely reflected instead of propagating into the second material. This occurs when two conditions are met: the second material has a lower refractive index than the first material and the angle of incidence for light hitting the boundary is sufficiently oblique. Note that refractive index defines the speed of propagation in a material and is defined as  $\eta = c / v$  where  $c$  is the speed of light in a vacuum and  $v$  is the speed of light within the material of interest.

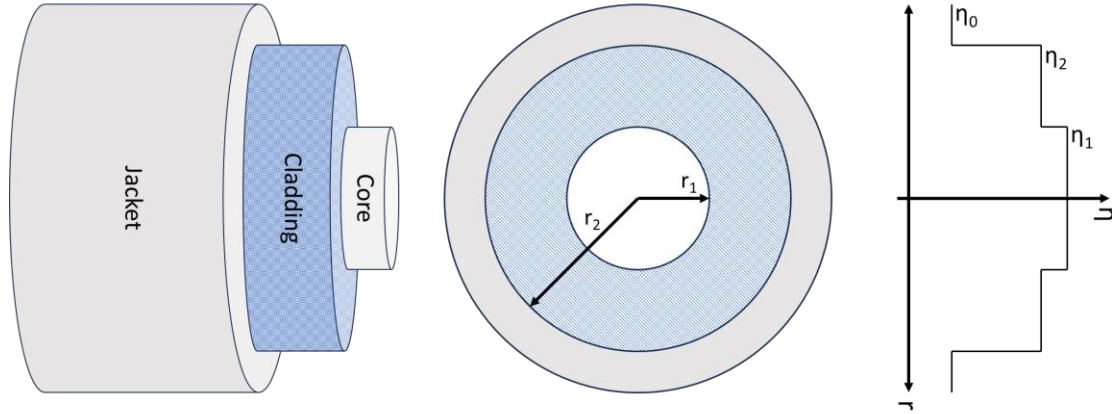


Figure 2.5: Cross-sectional diagram of a typical step-index optical fiber. The core is surrounded by cladding which has a slightly lower refractive index than the core (to abide by the principles of total internal reflection). Jacket layers are often included to protect the optical fiber from outside elements but do not affect its optical properties.

Optical fiber typically consists of a cylindrical core of silica surrounded by a cladding with a lower index than the core to abide by total internal reflection, Fig. 2.5. However, the geometric approach does not sufficiently describe light propagation through an optical fiber since the wavelength of light is comparable in size to the fiber core [37]. Approaching the problem using Maxwell's equations is, therefore, integral to a complete understanding. Maxwell's equations define the behavior of electromagnetic waves

$$\nabla \times \vec{E} = -\frac{\partial \vec{B}}{\partial t} \quad (2.3)$$

$$\nabla \times \vec{H} = \frac{\partial \vec{D}}{\partial t} \quad (2.4)$$

$$\nabla \times \vec{B} = 0 \quad (2.5)$$

$$\nabla \times \vec{D} = 0 \quad (2.6)$$

where  $\vec{E}$  is the electric field vector,  $\vec{D}$  is the electric flux density,  $\vec{H}$  is the magnetic field vector, and  $\vec{B}$  is the magnetic flux density. The field vectors and the flux densities are related such that

$$\vec{D} = \epsilon_0 \vec{E} + \vec{P} \quad (2.7)$$

$$\vec{B} = \mu_0 \vec{H} + \vec{M} \quad (2.8)$$

where  $\epsilon_0$  and  $\mu_0$  are the permittivity and permeability in free space and  $\vec{P}$  and  $\vec{M}$  are the electrical and magnetic polarization dependences. Note that  $\vec{M} = 0$  due to the non-magnetic properties of silica.

While evaluating  $\vec{P}$  traditionally requires a microscopic quantum-mechanical approach, this can be avoided by limiting the range of analysis to medium resonances covering wavelengths between  $0.5 - 2 \mu\text{m}$  which also corresponds to the extremely relevant low-loss region for optical fiber. Likewise, the analysis is further simplified by ignoring nonlinear effects. Using these conditions,  $\vec{P}$  and  $\vec{E}$  can then be related by

$$\mathbf{P}(\mathbf{r}, t) = \epsilon_0 \int_{-\infty}^{\infty} \chi(\mathbf{r}, t - t') \cdot \mathbf{E}(\mathbf{r}, t') dt' \quad (2.9)$$

where  $\chi$  is the linear susceptibility [36] which is a constant in an isotropic material such as silica glass. The wave equation for optical fiber can be developed by taking the curl of equation 2.3 and using equations 2.4 – 2.8

$$\nabla \times \nabla \times \mathbf{E} = -\frac{1}{c^2} \frac{\partial^2 \mathbf{E}}{\partial t^2} - \mu_0 \frac{\partial^2 \mathbf{P}}{\partial t^2} \quad (2.10)$$

where the speed of light is defined as  $c = (\epsilon_0\mu_0)^{-\frac{1}{2}}$ . By further expanding Equation 2.10 by taking the Fourier transform, the equation then becomes

$$\nabla \times \nabla \times \mathbf{E} = -\epsilon(\mathbf{r}, \omega) \cdot \left(\frac{\omega^2}{c^2}\right) \cdot \mathbf{E} \quad (2.11)$$

and the frequency-dependent dielectric constant is defined as  $\epsilon(\mathbf{r}, \omega) = 1 + \tilde{\chi}(\mathbf{r}, \omega)$  where  $\tilde{\chi}(\mathbf{r}, \omega)$  is the Fourier transform of  $\chi(\mathbf{r}, t)$ . Note that  $\epsilon$  is, in general, a complex number whose real and imaginary parts relate to the frequency-dependent refractive index ( $\eta$ ) and the absorption coefficient ( $\alpha$ ) by

$$\epsilon = \left(\eta + \frac{i\alpha c}{2\omega}\right)^2 \quad (2.12)$$

Note that the frequency dependence of  $\eta$  refers to the chromatic dispersion which is a major limiting performance parameter for optical networks. Equation 2.11 can be reformulated by leveraging the fact that  $\alpha$  should be sufficiently low for SSMF and SSMF should be isotropic to then become

$$\nabla^2 \mathbf{E} + \eta^2(\omega) \cdot k_0^2 \cdot \mathbf{E} = 0 \quad (2.13)$$

where  $k_0 = \omega/c = 2\pi/\lambda$  is the free-space wave number and  $\lambda$  is the free-space wavelength. The above analysis can then be further expanded to solve for the supported modes of the optical fiber. Note that optical modes refer to specific solutions of the wave equation which satisfy the dielectric boundary conditions. Three types of modes exist: guided modes (which are crucial for optical communication), leaky modes, and radiation

modes [38]. Equation 2.13 can be expressed in cylindrical coordinates to take advantage of the cylindrical symmetry of optical fiber

$$\frac{\partial^2 \mathbf{E}_z}{\partial \rho^2} + \frac{1}{\rho} \frac{\partial \mathbf{E}_z}{\partial \rho} + \frac{1}{\rho^2} \frac{\partial^2 \mathbf{E}_z}{\partial \phi^2} + \frac{\partial^2 \mathbf{E}_z}{\partial z^2} + \eta^2 k_0^2 \mathbf{E}_z = 0 \quad (2.14)$$

where the refractive index for core radius  $a$  is defined as

$$\eta = \begin{cases} \eta_1 & \text{if } \rho > a \\ \eta_2 & \text{if } \rho < a \end{cases} \quad (2.15)$$

Equation 2.14 is written in terms of  $\mathbf{E}_z$  since the other components can be defined relative to this component. Using separation of variables, Eqn. 2.15 is readily solved [36]

$$\mathbf{E}_z(\rho, \phi, z) = F(\rho)\Phi(\phi)Z(z) \quad (2.16)$$

$$Z(z) = e^{i\beta z} \quad (2.17)$$

$$\Phi(\phi) = e^{im\phi} \quad (2.18)$$

$$F(\rho) = \begin{cases} AJ_m(\gamma\rho) + BY_m(\gamma\rho) & \text{for } \rho < a \\ CK_m(\nu\rho) + DI_m(\nu\rho) & \text{for } \rho > a \end{cases} \quad (2.19)$$

where A, B, C, and D are constants, and  $J_m$ ,  $Y_m$ ,  $K_m$ , and  $I_m$  are Bessel functions [39],  $\beta$  is the propagation constant, and  $m$  is an integer to maintain the periodicity with respect to  $\phi$ . The parameters  $\gamma$  and  $\nu$  are defined such that

$$\gamma^2 = \eta_1^2 k_0^2 - \beta^2 \quad (2.20)$$

$$\nu^2 = \beta^2 - \eta_2^2 k_0^2 \quad (2.21)$$

Using the above methodology, the general solution for the wave equation, Eqn. 2.14, has the form

$$\mathbf{E}_z = \begin{cases} AJ_m(\gamma\rho)e^{im\phi}e^{i\beta z} & \text{for } \rho < a \\ CK_m(\nu\rho)e^{im\phi}e^{i\beta z} & \text{for } \rho > a \end{cases} \quad (2.22)$$

Similarly, the magnetic field can be solved using similar methods resulting in the equivalent equation differing only from the coefficients

$$\mathbf{H}_z = \begin{cases} BJ_m(\gamma\rho)e^{im\phi}e^{i\beta z} & \text{for } \rho < a \\ DK_m(\nu\rho)e^{im\phi}e^{i\beta z} & \text{for } \rho > a \end{cases} \quad (2.23)$$

Guided modes in optical fiber meet the criteria that  $\eta_1 > \bar{\eta} > \eta_2$  where  $\bar{\eta}$  is the effective refractive index. This is derived from Equations 2.20-21 as the parameters  $\gamma$  and  $\nu$  must be greater than zero to support a mode. Note that modes do not propagate when  $\bar{\eta} \geq \eta_1$  while they are no longer guided when  $\bar{\eta} \leq \eta_2$ . These conditions define an important metric: the normalized frequency (also known as the V number)

$$V = \frac{2\pi a}{\lambda} \sqrt{\eta_1^2 - \eta_2^2} \quad (2.24)$$

SSMF is specifically designed to support only one optical mode which corresponds to  $V < 2.405$ .

#### 2.2.2.2 Fiber Attenuation and Loss Mechanics

Fiber losses are a crucial consideration for optical networks as these effects limit the amount of power that can reach from transmitter to receiver during transmission. The fiber absorption coefficient ( $\alpha$ ), previously identified in Eqn. 2.12, is a parameter used to

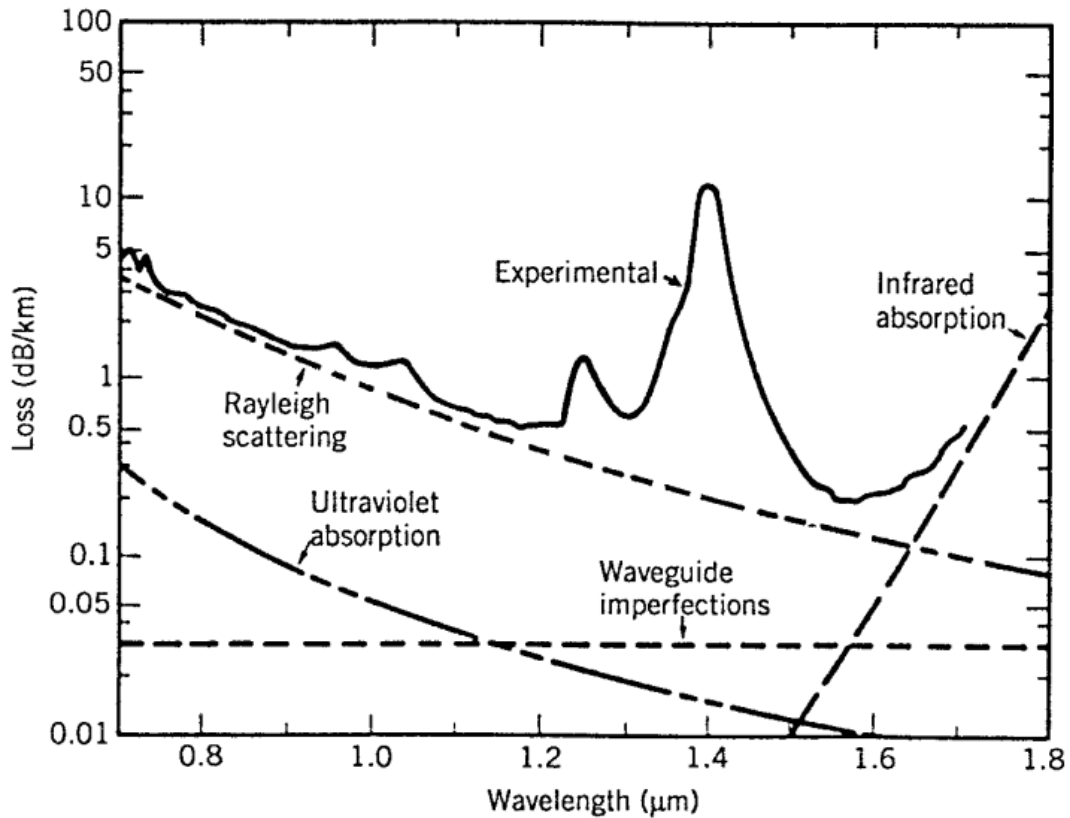


Figure 2.6: Spectral loss profile of single-mode fiber for fundamental loss mechanisms such as Rayleigh scattering, and intrinsic absorption characteristics associated with electronic and vibrational resonances [36].

define this power attenuation within an optical fiber. The power decays exponentially and is thereby given by

$$P_{out} = P_{in}e^{-\alpha L} \quad (2.25)$$

where  $L$  is the distance typically measured in kilometers. However, the fiber attenuation is usually reported in decibels per kilometer allowing for the convenient analysis

$$P_{out}(dBm) = P_{in}(dBm) - \alpha L \quad (2.26)$$

where  $P_{in}(dBm)$  and  $P_{out}(dBm)$  are measured in decibel-watt.

While the absorption coefficient gives a generalized measure of power decay, there are multiple sources which are major contributors to this: Material absorption and Rayleigh scattering. Material absorption occurs from either intrinsic or extrinsic material properties. Intrinsic material properties relate to electronic and vibrational resonances associated with that material [36]. Figure 2.6 shows the intrinsic material absorption for silica – electronic resonances which are occurring in the ultraviolet region where wavelengths are less than 0.4  $\mu\text{m}$  and vibrational resonances which are occurring in the infrared region where wavelengths are greater than 7.0  $\mu\text{m}$  both have a marginal impact within the typical operating region of optical fibers from 0.8  $\mu\text{m}$  to 1.6  $\mu\text{m}$ . These effects result in a minimum theoretical absorption coefficient for silica to be  $\leq 0.1$  dB/km within this range and even as low as 0.03 dB/km for wavelengths between 1.3  $\mu\text{m}$  and 1.6  $\mu\text{m}$  which are commonly used for long-haul optical networks. Extrinsic properties for fiber loss include impurities within the silica glass during fabrication – these effects will be largely ignored here as fiber manufacturers have created methods for sufficient purity to minimize these losses.

Rayleigh scattering is a fundamental loss mechanism that occurs due to microscopic random fluctuations of the refractive index of the fiber thereby resulting in light scattering during transmission. These refractive index fluctuations appear due to material density fluctuations stemming from cooling molten silica during manufacturing. The Rayleigh scattering scales with wavelength on the scale  $\lambda^4$  and thus varies as

$$\alpha_R = \frac{C}{\lambda^4} \quad (2.27)$$

where  $C$  is a constant typically between  $0.7 - 0.9 \text{ (dB/km)}\cdot\mu\text{m}^4$  depending on the fiber core [40]. Under these assumptions, Rayleigh scattering introduces a minimum fiber loss range of  $\sim 0.12 - 0.16 \text{ dB/km}$  at the nominal wavelength of  $1550 \text{ nm}$ .

Aside from material absorption and Rayleigh scattering, other loss mechanisms include fiber imperfections during fabrication such as random variations in core size. However, manufacturers have minimized these losses to as low as  $\leq 0.03 \text{ dB/km}$  and thus are largely ignored in this analysis. Similarly, mechanical bends in fiber may introduce excess loss during transmission but limiting these bends to a radius of at least  $5 \text{ mm}$  results in minimal losses of  $\leq 0.01 \text{ dB/km}$ . Total loss in modern commercial optical fiber is limited to  $\sim 0.2 \text{ dB/km}$  with record with experimentally recorded losses as low as  $0.142 \text{ dB/km}$  for silica-based fiber [41].

### 2.2.2.3 Chromatic Dispersion

Chromatic dispersion, the primary type of dispersion found within single mode fibers, is an optical phenomenon where pulses are temporally broadened resulting in intersymbol interference between subsequent symbols. This phenomenon occurs because different spectral components of an optical signal will travel at different velocities within the fiber and thus reach the end of the fiber at different times. Consider a single-mode fiber of length  $L$ , a specific spectral component would clearly travel the distance in the time  $t = L / v_g$ . Note that  $v_g$  is the group velocity which is related to the optical frequency by  $v_g = d\omega / d\beta$  where  $\beta$  is the propagation constant. Considering a pulse with a spectral width of  $\Delta\omega$ , the temporal broadening can then be calculated as

$$\Delta t = \frac{dt}{d\omega} \Delta\omega = \frac{d}{d\omega} \left( \frac{L}{v_g} \right) \Delta\omega \quad (2.28)$$

where  $t = L / v_g$  is used to further expand the relationship. Further extending this analysis can be done by substituting with  $v_g = d\omega / d\beta$  resulting in

$$\Delta t = L \frac{d^2\beta}{d\omega^2} \Delta\omega = L\beta_2 \Delta\omega \quad (2.29)$$

$\beta_2$  is often referred to as the group velocity dispersion, or the second-order dispersion. Converting to wavelength analysis for optical systems is preferred resulting in [36]

$$\Delta t = -\frac{2\pi c}{\lambda^2} \beta_2 L \Delta\lambda = DL\Delta\lambda$$

where  $D$  is a conventional fiber parameter known as the dispersion parameter and is often reported in units of ps/nm-km. The typical dispersion value for SSMF is ~17 ps/nm-km.

#### 2.2.2.4 Nonlinearities

The analysis of light propagation through an optical fiber was previously performed under the assumption that nonlinear effects were to be ignored. In reality, silica glass exhibits a nonlinear change in refractive index that scales with the intensity of the light

$$\eta = \eta_0 + \eta'_2 |E_0(z, t)|^2 \quad (2.30)$$

where  $\eta_0$  is the linear refractive index,  $\eta'_2$  is the nonlinear refractive index, and  $E_0(z, t)$  is the pulse envelope [42]. This is called the optical Kerr effect. Note that  $\eta'_2$  is typically on

the scale of  $\sim 2.0 \times 10^{-20} \text{ m}^2/W$  for SSMF which results in a modest change in refractive index from typical power levels. However, this small change still presents an impact on modern optical network performance due to the long transmission distances – specifically in the form of self-phase modulation and cross-phase modulation.

Self-phase modulation (SPM) is a phenomenon where a specific frequency exhibits a nonlinear response onto itself via changing the electric field power. Consider a linearly polarized electric field defined as

$$E = \frac{1}{2} E_0(z, t) \exp(-j\eta k_0 z) \exp(j\omega_0 t) \quad (2.31)$$

By applying the nonlinear refractive index from Eqn. 2.30 to the electric field, it results in the power-dependent nonlinear relationship for the electric field

$$E = \frac{1}{2} E_0(z, t) \exp(-j\eta_0 k_0 z) \exp(j\omega_0 t) \exp(-j\eta'_2 |E_0(z, t)|^2) \quad (2.32)$$

Note that this additional phase term, which arises from the nonlinearity of the refractive index, introduces new frequency components to the signal often resulting in spectral broadening. Spectral broadening results in increased optical bandwidth which can become a limiting performance factor for optical networks.

Cross-phase modulation (XPM) is a phenomenon which occurs for WDM optical networks which carry multiple signals on the same fiber. Unlike the case for SPM, the phase shift which occurs due to the nonlinearities depends instead on the power of all other channels that are transmitted. While XPM may be considered a potential source of significant degradation for WDM optical networks which can carry upwards of 80 or

more wavelengths at a time, characterizing the impact on the system performance can prove to be quite difficult as it depends on a multitude of factors. The impact is dependent on not only the power and channel spacing between adjacent channels, but it is also dependent on the amount of CD present. In fact, networks designed with sufficient channel spacing and with enough CD exhibit minimal impact from XPM [43].

FWM is another major source of nonlinear degradation for optical fiber and results in signals on three different wavelengths interacting to generate a fourth electrical field with potential frequencies defined as

$$\omega_4 = \omega_1 \pm \omega_2 \pm \omega_3 \quad (2.33)$$

which demonstrates quite a few possibilities; however, only a few of these frequencies may satisfy the important phase-matching requirement [44]. FWM has two main mechanisms which limit system performance: the main channels transfer power to the newly generated channel and the newly generated channel causes interchannel crosstalk. Modern networks can somewhat limit the effects of FWM via accumulated CD as it limits the potential for phase matching. Likewise, phase matching could be further reduced by increasing channel spacing or even using unequal spacings between channels. However, this is not ideal as systems may be designed with a certain channel spacing to maximize capacity.

#### 2.2.2.5 Miscellaneous

A variety of secondary fiber effects exist but will not be discussed in detail here due to their limited impact when compared to the previously discussed properties. Polarization

effects such as polarization mode dispersion [45], polarization dependent loss [46], and cross-polarization modulation [47] are such examples.

### *2.2.3 In-Transit Optical Devices*

The optical networks of today facilitate expansive data transmission around the world as they transmit signals across vast distances and to various locations. These features require the use of specific devices: the optical amplifier and the optical filter. Optical amplifiers enable networks to compensate fiber losses while keeping signals within the optical domain. Optical filters such as the reconfigurable optical add-drop multiplexer (ROADM) allow network operators to choose the signal path of any arbitrary signal. In this section, we will discuss both optical amplifiers and optical filters in detail.

#### 2.2.3.1 Optical Amplifiers

There are two main types of amplifiers found within current long-haul optical communication systems: EDFAs and Raman amplifiers. While these devices both amplify the incoming optical signal and thus allow for the compensation of fiber losses, the mechanics by which this occurs differ slightly. Simply speaking, EDFAs use an optical fiber doped with erbium as the gain medium where a pump laser is multiplexed into the erbium-doped fiber. This excites the erbium ions which then results in an energy transfer from the excited erbium ions to the optical signal. Raman amplifiers use a different principle which is denoted as Raman amplification – energy transfer occurs based upon nonlinear interactions between the signal and pump lasers directly within the transmission optical fiber.

Despite the advantages of increasing transmission distance, amplifiers do degrade signal quality via noise addition. This results in a degraded OSNR [48]. This degradation is quantified using an important amplifier metric called the noise figure which is conventionally expressed as [48]

$$F = 2n_{sp}\chi \quad (2.34)$$

where  $n_{sp}$  is the spontaneous emission coefficient and  $\chi$  is the excess noise coefficient. Note that it is more common to represent this metric in units of decibels

$$F_n = 10 \log_{10}(F) \quad (2.35)$$

Ideal amplifiers would result in  $n_{sp} = \chi = 1$  which would result in a best-case noise figure of 3 dB. In practice, EDFAs exhibit a relatively large noise figure compared to this theoretical limit typically ranging between 5 dB to 8 dB. This is due to a large spontaneous emission coefficient ( $n_{sp} > 1$ ). Raman amplifiers, on the other hand, exhibit noise figures close to the theoretical limit since they exhibit a much lower spontaneous emission coefficient ( $n_{sp} \sim 1$ ). Despite this clear advantage, EDFAs are still a popular choice for optical networks where low noise figures are not necessary as they have lower manufacturing costs and higher power efficiencies such as metro links. Raman amplifiers are often chosen for long-haul optical networks where OSNR margins are limited.

Since the noise figure of an optical amplifier directly affects the OSNR of the optical network, it is advantageous to directly relate these parameters both in linear units and decibels

$$F = \frac{(SNR)_{in}}{(SNR)_{out}} \quad (2.36)$$

$$F_n = 10 \log_{10}(F) = 10 \log_{10} \left( \frac{(SNR)_{in}}{(SNR)_{out}} \right) = SNR_{in,dB} - SNR_{out,dB} \quad (2.37)$$

Note that these equations are defined in terms of SNR instead of OSNR. The relationship between SNR and OSNR is defined as [49]

$$OSNR = \frac{pR_s}{2B_{ref}} SNR \quad (2.38)$$

where  $p$  is the number of polarizations,  $R_s$  is the symbol rate, and  $B_{ref}$  is the reference resolution bandwidth which is commonly chosen to be 12.5 GHz or 0.1 nm. The OSNR is usually measured via an optical spectrum analyzer (OSA).

Long-haul optical networks often utilize more than just one amplifier during transit to further extend reach. For an optical link employing  $N$  uniformly spaced EDFAs, the output OSNR is given by [50]

$$OSNR_{dB} = 58 + P_0 - \Gamma - 10 \log_{10}(N) - F_n \quad (2.39)$$

where  $P_0$  is the total optical power launched into the fiber and  $\Gamma$  is the amplifier gain. Cascading amplifiers reduces the OSNR of the system. Calculations such as these are often performed as a preliminary link budget for optical networks to determine the viable reach of an amplified system alongside any excess margins that may be available.

### 2.2.3.2 Optical Filters

Optical filters selectively transmit light in a particular frequency band while absorbing the remainder. One important type of optical filter in long-haul optical networks is the ROADMs. ROADMs allow network operators to remotely add or drop network traffic on a per-wavelength basis enabling an all-optical routing solution. Likewise, it enables power equalization between the different WDM channels to improve system OSNR and maximize reach. The main component of a ROADM which enables this is the wavelength-selective switch (WSS) which can be manufactured using various techniques such as micro-mirror arrays, planar lightwave circuits, and liquid crystal on silicon [51].

It is necessary to carefully manage certain design constraints when planning networks using ROADMs as they can introduce impairments which may heavily degrade the signal quality. Limited pass-band insulation can introduce crosstalk between adjacent channels. In the case of cascaded ROADMs, this effect can accumulate resulting in severe performance degradations [52]. Other pass-band related penalties also exist such as frequency drifts between the signals of interest and the ROADM passband as well as filter tightening especially in the case of cascaded ROADMs.

Originally, ROADMs functioned on a fixed wavelength channel plan – typically 50 GHz or 100 GHz channel grid. Each signal added to the network needed to fit within these bands and placed relative to specific center wavelengths to be compatible with the ROADMs. Modern ROADMS now accommodate flexible grids where different channels can use both different channel widths and spacings.

## 2.2.4 Optical Receivers

Optical receivers serve the role of converting an optical signal into an electrical signal. The main component responsible for this conversion is the photodiode. In the case of coherent detection, the coherent receiver implements a photodiode-based architecture which enables polarization- and phase-diverse signal reception. These components are ubiquitous in long-haul optical networks and thus will be discussed here.

### 2.2.4.1 Photodiodes

Photodiodes convert optical signals back into the electrical domain as this is a necessary step for digitally processing the signal. Photodiodes operate by generating an electrical photocurrent which scales based on the incoming optical power

$$I_{PC} = RP_{in} \quad (2.40)$$

where  $I_{PC}$  is the resulting photocurrent,  $P_{in}$  is the incoming optical power, and  $R$  is the responsivity of the photodiode. As is obvious from the previous equation, the responsivity is an important photodiode parameter which determines the ratio of generated photocurrent to input optical power and is given by [53]

$$R = \eta \frac{e}{h\nu} = \eta \frac{e\lambda}{hc} = \eta \frac{\lambda}{1.24} \quad (2.41)$$

where  $\eta$  is the quantum efficiency,  $e$  is the electron charge,  $h$  is Planck's constant,  $c$  is the speed of light, and  $\lambda$  is the wavelength of the light incident on the photodiode. Note that  $hc/e \approx 1.24 \times 10^{-6} \text{ eVm}$  and thus the above equation assumes wavelength is reported in microns.

There are two main noise sources that result from a basic photodiode: thermal noise and shot noise [54]. Thermal noise is random voltage fluctuations that occur due to the random motion of the electrons in the device. The variance of the thermal noise can be characterized as

$$\sigma_{thermal}^2 = \frac{4k_B T B_e F_n}{R_L} \quad (2.42)$$

where  $k_B$  is Boltzmann's constant,  $T$  is the temperature,  $B_e$  is the effective bandwidth of the receiver,  $R_L$  is the circuit load resistance, and  $F_n$  is the noise figure of any amplifier within the circuit. Shot noise is the phenomenon associated with the statistical distribution of the discretely generated electric charges during photodetection. The variance of the shot noise can also be calculated as

$$\sigma_{shot}^2 = 2qI_{PC}B_e \quad (2.43)$$

where  $q$  is the electron charge. The effects of these noise sources are modeled for a basic PIN photodiode with respect to the input optical power in Fig. 2.7 using the general parameter assumptions in Table 2.1. The modeling shows that different noise sources may dominate in different link configurations. Note that another type of noise known as the relative intensity noise (RIN) exists and is apparent at the receiver, but this largely results from the instability of the transmitter laser and thus it will be disregarded.

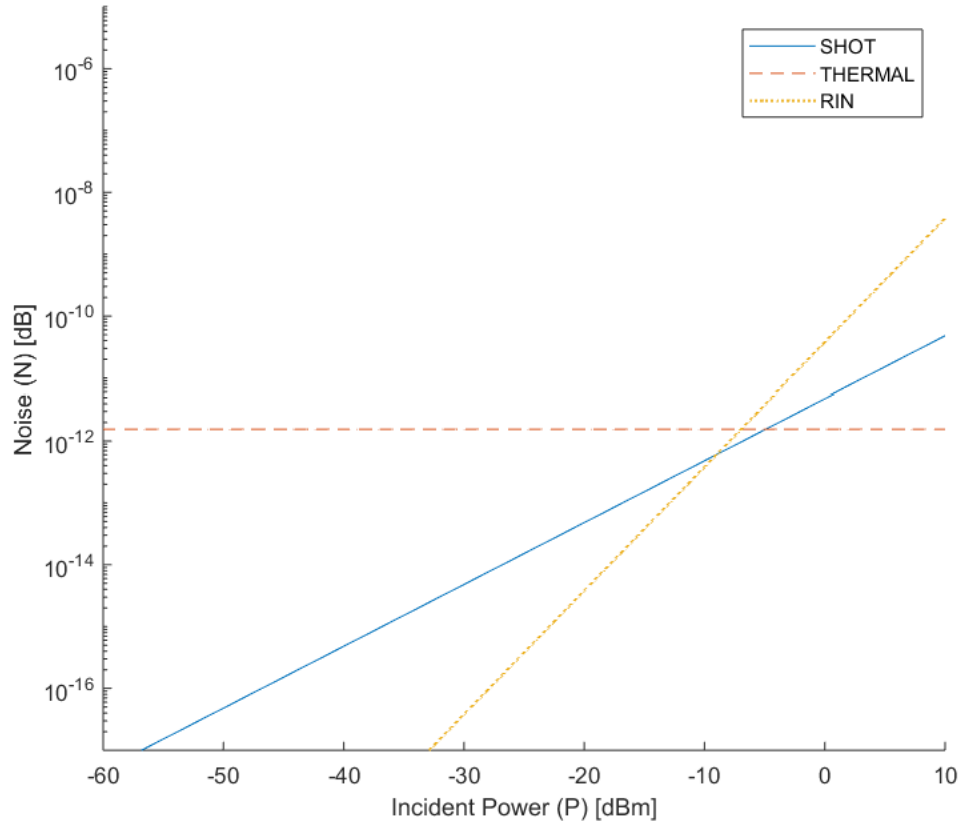


Figure 2.7: Noise as a function of incident optical power for a PIN photodiode. For low incident optical power, thermal noise dominates while for higher powers, shot noise dominates at the receiver. However, note that RIN noise dominates shot noise for high power systems under these constraints.

Table 2.1  
General assumptions for photodiode noise model

Symbol	Description	Numerical Value
$T$	Temperature	300 [K]
$\lambda_0$	Wavelength	1550e-9 [m]
$B_e$	Electrical Bandwidth	25e9 [Hz]
$B_o$	Optical Bandwidth	100e9 [Hz]
$RIN$	Rel. Intensity Noise	-145 [dB/Hz]
$R$	Responsivity	0.8 [A/W]
$F_n$	Noise Figure (for TIA)	5 [dB]
$M$	APD Gain	100
$F$	Excess Noise Factor	5

### 2.2.4.2 Coherent Receivers

Coherent receivers are largely responsible for the record data rates of modern optical networks. They have enabled the use of today's advanced modulation formats which can encode information on both the amplitude and phase as well as on both polarizations of an optical signal. There are a multitude of coherent receiver architectures, each with increasing complexity, such as the single-branch coherent receiver, balanced coherent receiver, and balanced IQ coherent receiver [54]. Here, we will focus on the balanced IQ coherent receiver and its essential building blocks due to its widespread usage in long-haul networks.

The coherent receiver operates via mixing an incoming information signal with a

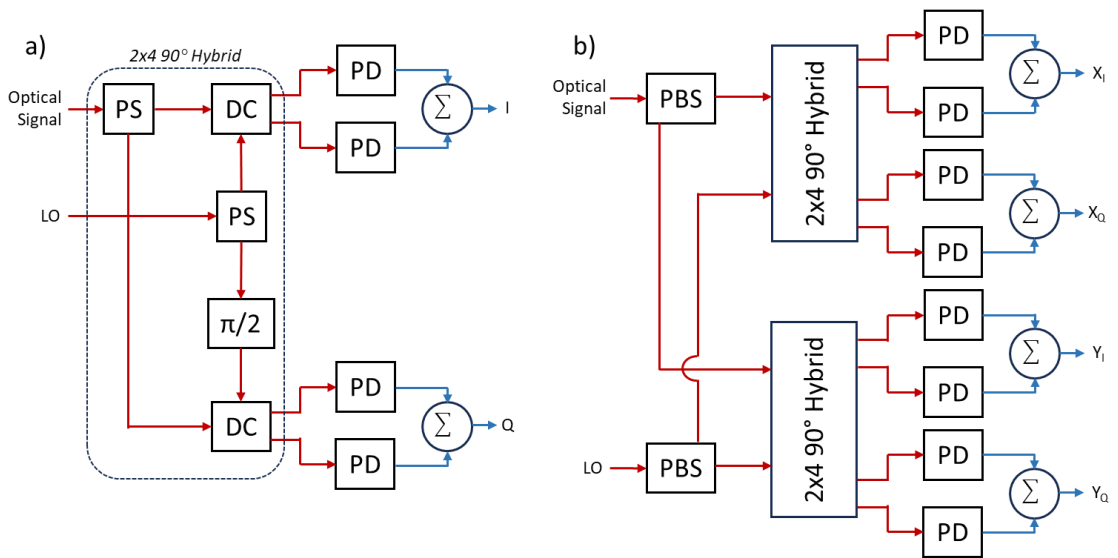


Figure 2.8: (a) Balanced IQ coherent receiver constructed from power splitters (PS), directional couplers (DC), phase shifters ( $\pi/2$ ), and photodiodes (PD). 2x4 90° Hybrid architecture is shown. (b) Dual polarization IQ coherent receiver architecture which uses a combination of 2x4 90° hybrids and polarization beam splitters (PBS) to jointly receive the X and Y polarizations.

high-power local oscillator (LO) which serves as a phase reference [55]. A balanced IQ coherent receiver consists of power splitters, phase shifters, directional couplers, and balanced photodiodes, Fig. 2.8(a). The incoming signal and the LO are split via a power splitter, and one is delayed by a factor of  $\pi/2$  to enable detection of both in-phase (I) and quadrature (Q) components of the signal. The signal and LO are then coherently mixed using a directional coupler and sent to a pair of balanced photodiodes. If we allow the complex electric fields of the signal and LO to be defined as [20]

$$E_s(t) = A_s(t) \exp(i\omega_s t) \quad (2.44)$$

$$E_{LO}(t) = A_{LO}(t) \exp(i\omega_{LO} t) \quad (2.45)$$

where  $A_s(t)$  is the complex amplitude and  $\omega_s$  is the angular frequency, then the electric fields and power incident on the balanced photodiodes can be defined as

$$E_1 = \frac{1}{\sqrt{2}}(E_s + E_{LO}) \quad (2.46)$$

$$P_s = k \frac{|A_s|^2}{2} \quad (2.47)$$

$$E_2 = \frac{1}{\sqrt{2}}(E_s - E_{LO}) \quad (2.48)$$

$$P_{LO} = k \frac{|A_{LO}|^2}{2} \quad (2.49)$$

Note that, ideally, the balanced photodiodes are identical; however, in practice, they are simply manufactured to be as close as possible. Using a pair of balanced photodiodes, it

is possible to suppress the DC component and thus maximize the beat between the signal and the LO. The output photocurrents from the balanced photodiodes are

$$I_1(t) = \frac{R}{2} \left[ P_s(t) + P_{LO} + 2\sqrt{P_s(t)P_{LO}} \cos(\omega_{IF}t + \theta_s(t) - \theta_{LO}(t)) \right] \quad (2.50)$$

$$I_2(t) = \frac{R}{2} \left[ P_s(t) + P_{LO} - 2\sqrt{P_s(t)P_{LO}} \cos(\omega_{IF}t + \theta_s(t) - \theta_{LO}(t)) \right] \quad (2.51)$$

where  $R$  is the responsivity of the photodiode,  $\omega_{IF} = |\omega_s - \omega_{LO}|$  is the intermediate frequency,  $\theta_s(t)$  is the phase of the signal, and  $\theta_{LO}(t)$  is the phase of the LO. Therefore, the output of the balanced photodiode pair is

$$I(t) = I_1(t) - I_2(t) = 2R\sqrt{P_s(t)P_{LO}} \cos(\omega_{IF}t + \theta_s(t) - \theta_{LO}(t)) \quad (2.52)$$

Note that since the photocurrent is proportional to  $\sqrt{P_{LO}}$ , the LO, which maintains a constant power, acts as a consistent gain source for the received signal. The LO phase term includes only phase noise which randomly varies with time. It is straightforward to extend this to the case of the dual-polarization coherent receiver by adding a polarization beam splitter at the input to the system, Fig. 2.8(b).

To accurately decode the incoming signal, it is important to minimize the frequency offset between the signal and the LO [56]. When the two lasers beat at the photodiode, it results in a growing relative phase offset between symbols as seen in Eqn. 2.52. This impairment can be mitigated in a few ways. One simple way is to use the same laser at the transmitter and receiver, but this is unpractical since transmission distances can reach 1000s of kilometers. Other traditional solutions include the use of a phase-locked loop circuit to synchronize the phase of the output signal with a reference signal.

However, this adds system complexity and can be quite costly. It is now popular in modern optical networks to solve this issue using DSP processing on the received waveform which will be discussed in the following section.

## **2.3 Digital Signal Processing for Optical Networks**

While DSP is used in a variety of optical applications (e.g., equalization in direct detect optical links), this section will focus on modern coherent links as these systems are largely defined by their associated DSP and thus offer a larger assortment of DSP to discuss. These DSP algorithms are designed to optimize the signal for transmission through a specific channel or to compensate for impairments that occurred during transmission – these functions can be implemented at either the transmitter or the receiver and are often balanced as such to provide optimal performance. It is noted that the following section is not an exhaustive list of all possible DSP, but instead an exploration of commonly used algorithms for commercial applications with an emphasis on the types of algorithms used within this work.

### *2.3.1 Transmitter-Side DSP for Coherent Optical Networks*

#### 2.3.1.1 Advanced Modulation Formats

Modulation is the process of using a lower-frequency *information signal* to vary characteristics of a higher-frequency *carrier signal*. The characteristics of the carrier signal that are usually varied are the amplitude, phase, and/or the frequency. DSP at the transmitter-side is typically used to modulate the optical signal in such a way that it is optimized for the specific channel which it is being propagated through. This is usually

with respect to the channel capacity and optical signal-to-noise ratio (OSNR) – higher-order modulation formats increase spectral efficiency but require higher signal power which in turn leads to higher nonlinearities. The types of modulation applied by the transmitter include many different types of advanced modulation formats which can be divided into two main categories: single-carrier and multi-carrier formats.

Single carrier formats are such that the waveform is modulated directly onto the carrier. Formats in this category include pulse amplitude modulation (PAM-N) where the digital waveform is encoded across N amplitude levels, phase-shift keying (N-PSK) where the digital waveform is encoded as N different phases, and quadrature amplitude modulation (N-QAM) which combines  $\sqrt{N}$  amplitude and phase encodings to represent the digital waveform (with some exceptions for specific QAM formats such as 8-QAM or 32-QAM). Frequency-shift keying is another type of modulation format where digital information is encoded with respect to frequency changes of the carrier. A special subset of single-carrier modulation formats are time-domain hybrid modulation formats (TD-HMF) where different modulation formats are interleaved in time allowing for non-integer spectral efficiencies (on average) and thus more flexibility for channel optimization [57]. However, it is worth noting that granularity of the spectral efficiency using TD-HMF is limited by the interleaving schedule and requires increased DSP complexity to handle which can make this method impractical for some systems.

Multi-carrier formats divide a digital waveform into multiple subcarriers to match the channel of interest more optimally. This is called digital subcarrier multiplexing (DSCM) and it is analogous to WDM where channels are generated via independent carriers and multiplexed onto the same transmission medium. The

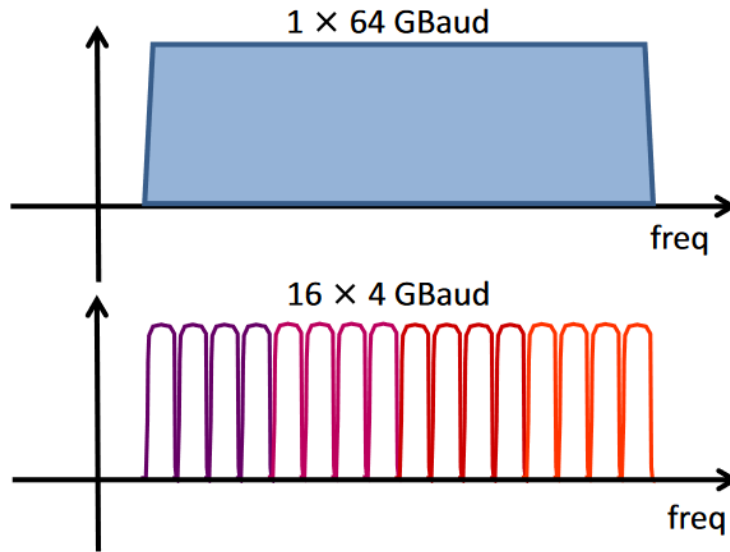


Figure 2.9: Spectral depiction of single-carrier and multi-carrier formats [58]. Single-carrier formats utilize a single high baudrate signal while multi-carrier formats use multiple lower baudrate signals to carry the data.

waveforms are generated by means of using the fast Fourier transform (FFT). The total capacity of multi-carrier formats approaches the capacity of the sum of the subcarriers with an associated penalty for any implemented guard bands or non-ideal channel spacing, Fig. 2.9. Examples of multi-carrier formats include discrete multi-tone (DMT) and orthogonal frequency-division multiplexing (OFDM). DMT is traditionally used to signify baseband wired multicarrier communication while OFDM is traditionally for wireless multicarrier communication. Advantages of multi-carrier modulation formats include the ability to modify the system on a subcarrier basis allowing for greater flexibility and channel optimization. It may also reduce nonlinear penalties which can be attributed to the lower baud rates of the individual subcarriers. Likewise, DSCM can be used to implement “point-to-multipoint” links which allow for digitally provisioning

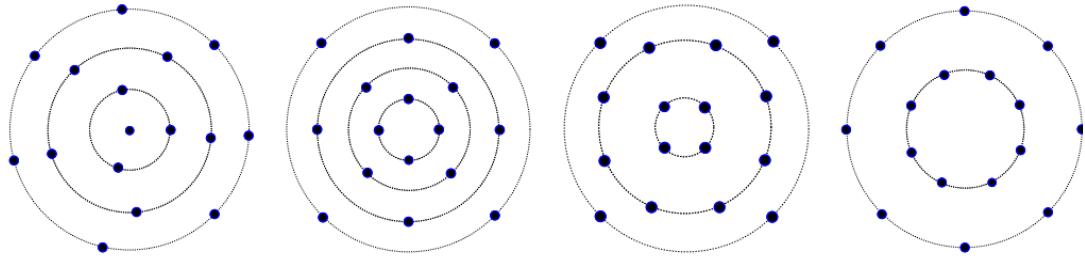


Figure 2.10: Examples of geometrically shaped 16QAM constellations [60].

channels for independent transmission thereby alleviating equipment costs during deployment [58].

### 2.3.1.2 Geometric and Probabilistic Shaping

Geometric shaping (GS) is defined by establishing the constellation structure of a transmitted signal. For example, traditional QAM signals are transmitted in a square lattice shape. Research has shown that alternative constellation shapes may provide benefits with respect to traditional link penalties such as nonlinearities. In [59], it is shown that 16-QAM constellations can be shaped to be more tolerant to linear/nonlinear phase distortions – performance was improved by 1.1 dB over traditional square QAM. Likewise, in [60], it was shown that performance gains of  $\geq 2$  dB were possible by optimizing the radius distributions of various constellation geometries, Fig. 2.10. However, GS waveforms require specialized DSP to manage and locating the optimum operating configuration is difficult.

Probabilistic shaping (PS) is an alternative approach to achieve the non-integer spectral efficiencies provided by TD-HMF [61]. PS-based methodologies map the waveform to a non-uniform distribution where lower-energy constellation points are

more frequently utilized allowing for a flexible entropy and thus spectral efficiency. This technique also has other advantages such as improved tolerance to nonlinearities. Likewise, PS is relatively easy to implement in practical systems – low complexity encoder/decoder pairs can create these mappings to a distribution of choice [62].

### 2.3.1.3 Miscellaneous Transmitter-Side DSP

Other transmitter-side DSP include functions such as pulse shaping or linear and nonlinear precompensation as well as FEC encoding [63, 64]. Pulse shaping can reduce intersymbol interference from neighbouring channels while precompensation can be used to digitally reduce both linear and nonlinear impairments. In [64], Roberts et al. demonstrates the reduction of SPM effects using digital precompensation. It is noted that pulse shaping is often used in combination with a matched filter at the receiver to maximize the SNR. A common example of one such pulse shape is the root raised cosine (RRC) filter. Likewise, FEC encoding is used to aid in correcting erroneous bits in the received waveform by appending parity bits to the waveform.

## 2.3.2 *Receiver-Side DSP for Coherent Optical Networks*

### 2.3.2.1 Chromatic Dispersion Compensation

Chromatic dispersion compensation is an important operation in the DSP chain for modern optical networks as it counteracts the accumulated dispersion that occurred during transmission instead of requiring links to be dispersion managed using specific hardware. CD can be compensated via filters in either the time or frequency domain. Low

amounts of CD can be removed in the time domain via an FIR filter with tap weights and number of taps defined by [65]

$$a_k = \sqrt{\frac{j c T^2}{D \lambda^2 z}} \exp\left(-j \frac{\pi c T^2}{D \lambda^2 z} k^2\right) \quad (2.53)$$

$$N = 2 \times \left\lfloor \frac{|D| \lambda^2 z}{2 c T^2} \right\rfloor + 1 \quad (2.54)$$

where  $D$  is the fiber dispersion coefficient,  $\lambda$  is the central wavelength of the transmitted signal,  $z$  is the fiber length,  $T$  is the symbol period, and  $\lfloor \cdot \rfloor$  is the floor operator.

For longer links with large amounts of accumulated CD, it is more efficient to perform corrections in the frequency domain due to the large number of taps required for the time domain filter. An all-pass filter is used to correct for the CD and this filter has a transfer function defined as [66]

$$G(z, \omega) = \exp\left(-j \frac{D \lambda^2 z}{4 \pi c} \omega^2\right) \quad (2.55)$$

The overlap-and-save method is conventionally used to implement this filter as it is efficient at evaluating the Fourier transform of long sequences of data. This is accomplished by dividing the signal into equal length segments (with overlap between the segments) and taking the DFT of these segments [67].

### 2.3.2.2 Timing Recovery

Timing recovery (TR) resamples the waveform at the optimum sampling points where the eye opening is maximized. Traditionally, a phase locked loop was used to synchronize

the clock to the correct sampling timing. This was implemented in hardware via a reference clock and oscillator. However, modern receivers operate in the digital domain which has necessitated the development of software-based digital techniques to accomplish this. There have been three major avenues for TR: time domain, frequency domain, and hybrid time-frequency domain approaches.

Time domain techniques process directly on the received waveform and shift the sampling time based on a calculated timing error offset. Examples of time domain techniques include the Gardner method [68], the Alexander phase detector [69], and the Mueller and Müller algorithm [70]. Frequency domain techniques use Fourier transform coefficients to extract the correct clock. In [71], Godard demonstrated an example of a frequency domain algorithm.

In [72], a hybrid time-frequency domain algorithm called the digital filter and square timing recovery was demonstrated. Whether the signal is PAM, QAM, or PSK modulated, the signal can be represented as

$$r(t) = \sum_{n=-\infty}^{\infty} a_n g_T(t - nT - \epsilon(t)T) + n(t) \quad (2.56)$$

where  $a_n$  are the transmitted symbols,  $g_T(t)$  is the transmitted signal pulse,  $T$  is the symbol period, and  $n(t)$  is the channel noise. The offset from the optimal sampling point is determined by  $\epsilon(t)$ . To extract this timing error, the signal is first filtered and sampled at an integer multiple  $N$  of the symbol rate. The optimal receiver filter is a matched filter  $g_R(t) = g_T(t)$ . The signal is then squared to obtain

$$x_k = \left| \sum_{n=-\infty}^{\infty} a_n g\left(\frac{kT}{N} - nT - \epsilon(t)T\right) + \tilde{n}\left(\frac{kT}{N}\right) \right|^2 \quad (2.57)$$

where  $g(t)$  is the filtered transmitter pulse from  $g_T(t)$ ,  $N$  is the integer oversampling factor, and  $\tilde{n}(t)$  is the received noise. The received signal contains a spectral component at  $1/T$ . The spectral component and its normalized phase can be computed as

$$X_m = \sum_{k=mLN}^{(m+1)LN-1} x_k e^{-\frac{j2\pi k}{N}} \quad (2.58)$$

$$\hat{\epsilon}_m = \frac{-1}{2\pi} \arg(X_m) \quad (2.59)$$

The normalized phase yields an unbiased estimate for the timing delay  $\epsilon(t)$  for a block of symbols with length  $L$  as we assume that the timing delay is a slow-varying effect and thus constant over a short duration. The chosen number of samples  $L$  is crucial to balance for optimal algorithm operation as too few samples result in high jitter in the estimation while too many samples result in poor estimation as the estimation duration may exceed the rate which the timing delay varies. The oversampling rate for the algorithm must also be  $\geq 2$  as the phase needs to be extracted at symbol rate.

### 2.3.2.3 Polarization Demultiplexing

Modern optical networks encode information on both polarizations of the light signal which has enabled an instantaneous doubling of the symbol rate. However, the polarization state of the signal is not preserved as it propagates through fiber – the polarizations are arbitrarily rotated by the time the signal reaches the coherent receiver (at

the polarization beam splitter) which results in the received symbols consisting of a linear combination of the X and Y polarizations

$$\begin{bmatrix} X_{out} \\ Y_{out} \end{bmatrix} = \begin{bmatrix} h_{xx} & h_{xy} \\ h_{yx} & h_{yy} \end{bmatrix} \begin{bmatrix} X_{in} \\ Y_{in} \end{bmatrix} = \begin{bmatrix} h_{xx}^T X_{in} + h_{xy}^T Y_{in} \\ h_{yx}^T X_{in} + h_{yy}^T Y_{in} \end{bmatrix} \quad (2.60)$$

It is imperative to rotate the data back to its original orientation to accurately identify the original signals on the X and Y polarization. This is analogous to the famous “cocktail party problem” which is defined by the automatic processing the human brain does to differentiate individual conversations inside a loud, noisy room (i.e., determine an individual source from a mixture of multiple sources) [73, 74]. Typically, such as in the case of polarization demultiplexing, the problem is under-constrained since we do not know the original polarized data nor the mixing coefficients ( $h_{xx}$ ,  $h_{xy}$ ,  $h_{yx}$ ,  $h_{yy}$ ).

The constant/multi-modulus algorithms (CMA/MMA) [75, 76] are one commonly used method for determining these coefficients. The coefficients are iteratively solved on a symbol-by-symbol basis as

$$h_{xx}(n) \rightarrow h_{xx}(n) + \mu(r^2 - |X_{out}(n)|^2)X_{out}(n)X_{in}^*(n) \quad (2.61)$$

$$h_{xy}(n) \rightarrow h_{xy}(n) + \mu(r^2 - |X_{out}(n)|^2)X_{out}(n)Y_{in}^*(n) \quad (2.62)$$

$$h_{yx}(n) \rightarrow h_{yx}(n) + \mu(r^2 - |Y_{out}(n)|^2)Y_{out}(n)X_{in}^*(n) \quad (2.63)$$

$$h_{yy}(n) \rightarrow h_{yy}(n) + \mu(r^2 - |Y_{out}(n)|^2)Y_{out}(n)Y_{in}^*(n) \quad (2.64)$$

where  $\mu$  is the step size and  $r^2 = \mathcal{E}(a^4)/\mathcal{E}(a^2)$  is the radius of convergence. Note that  $a$  represents the theoretical symbols of that modulation format and  $\mathcal{E}$  represents the

expectation. The CMA algorithm utilizes the case where  $r^2 = 1$  which occurs for the 4-QAM modulation format while the MMA algorithm is a modification which allows for multiple amplitude levels and  $r^2 > 1$ .

One major limitation of the CMA/MMA algorithms results from the fact that the mixing coefficients ( $h_{xx}$ ,  $h_{xy}$ ,  $h_{yx}$ ,  $h_{yy}$ ) are updated independently and thus often converge to a singular state of polarization. One rudimentary method for rectifying this issue is to establish conditions that guarantee these mixing coefficients will always be orthogonal to one another:

$$h_{xy} = -h_{yx}^* \quad (2.65)$$

$$h_{yy} = h_{xx}^* \quad (2.66)$$

However, fiber effects such as polarization-dependent loss (PDL) exist which may invalidate this condition (which relies on the assumption that the mixing matrix is unitary) resulting in poor convergence performance for CMA/MMA algorithms with respect to polarization demultiplexing for these systems [77].

Some approaches exist which alleviate the issue of orthogonality: blind source separation (BSS) algorithms [78]. BSS algorithms are designed to separate out a set of signals from a mixed set with little or no information about the signals or how they are mixed. Besides alleviating the orthogonality issue, another advantage of the BSS approach is avoiding the singularity issue that may occur when updating the mixing coefficients. Popular BSS algorithms including principal component analysis (PCA) and

independent component analysis (ICA) have seen use within optical systems and have demonstrated similar or better performance to the other presented methodologies [79].

In the case of ICA, it has an analogous structure to the CMA/MMA algorithms where the mixing coefficients are instead updated in a multiplicative manner and update coefficients defined as [80]

$$B_{k+1} = N_k B_k \quad (2.67)$$

$$N_{1,1} = 1 + \mu(1 - |X_{out}|^2) \quad (2.68)$$

$$N_{1,2} = \frac{\mu|a|}{2\sigma^2} (e^{j\phi_1} Y_{out}^* - e^{-\phi_2} X_{out}) - \mu X_{out} Y_{out}^* \quad (2.69)$$

$$N_{2,1} = \frac{\mu|a|}{2\sigma^2} (e^{j\phi_2} X_{out}^* - e^{-\phi_1} Y_{out}) - \mu Y_{out} X_{out}^* \quad (2.70)$$

$$N_{2,2} = 1 + \mu(1 - |Y_{out}|^2) \quad (2.71)$$

where  $B_k$  is the 2x2 inverse mixing matrix,  $N_k$  is the 2x2 coefficient update matrix with coefficients  $N_{1,1}$ ,  $N_{1,2}$ ,  $N_{2,1}$ ,  $N_{2,2}$ , and  $a$  and  $\sigma$  are parameters defining the corresponding normal distribution.

#### 2.3.2.4 Frequency Offset Correction

Optical receivers in modern networks operate with a free-running LO which may result in a frequency difference between the received signal and the LO. To accurately receive the signal, this frequency offset (which results in a phase difference) is estimated and removed via DSP. One example of such an algorithm is a phase increment estimation

algorithm [81] which estimates the phase difference between consecutive samples  $a_k$  and  $a_{k-1}$

$$\Delta\varphi = 2\pi\Delta\nu T_S \quad (2.72)$$

where  $\Delta\nu$  is the frequency difference and  $T_S$  is the sampling time.

To estimate the frequency difference, a symbol is multiplied by the complex conjugate of the previous symbol which is then, in the case of  $n$ -PSK modulation, raised to the  $n$ th power. Multiplying by the complex conjugate results in a value whose phase is the difference of the two symbols while raising the value to the  $n$ th power unwinds the symbols to remove the phase modulated information. This is then summed over many samples to calculate an average phase. The phase is then divided by  $n$  as a correction factor for the  $n$ -power operation. The block diagram of this algorithm is shown, Fig. 2.11. Finally, an accumulated phase is subtracted from the original signal on a symbol-by-symbol basis

$$\varphi_k = k\Delta\varphi T_S \quad (2.73)$$

$$a_k = M e^{j(\theta - \varphi_k)} \quad (2.74)$$

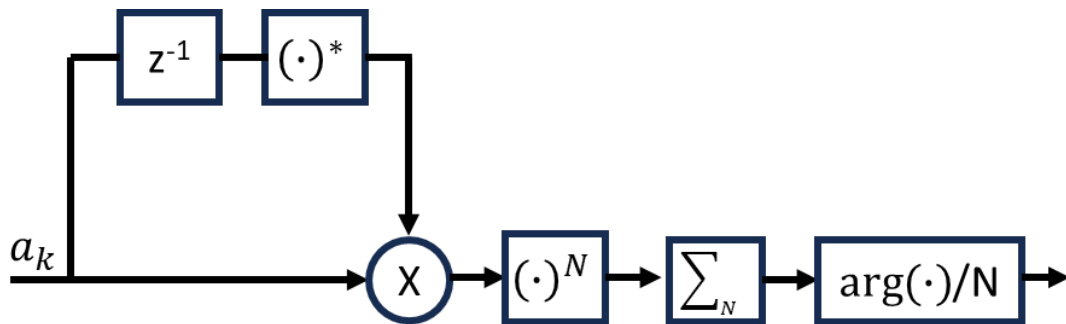


Figure 2.11: Block diagram for frequency estimation algorithm for PSK modulation formats where  $N$  is the number of constellation points (e.g., for QPSK,  $N = 4$ ).

### 2.3.2.5 Carrier Phase Recovery

The phase between the signal and the LO will randomly fluctuate relative to one another which results in the presence of phase noise in the received symbols. A constrained version of a decision-directed least mean squares algorithm is often used to compensate for the phase distortions whose filter is updated such that [82]

$$w_i = w_{i-1} + \mu(d_i - w_{i-1}x_i) \quad (2.75)$$

where  $\mu$  is the step size and  $d_i$  is the nearest constellation point to  $w_{i-1}x_i$ .

However, the filter is constrained such that if the filter update results in a different symbol decision, then the filter is instead updated as

$$w_i = w_{i-1} + \alpha\mu(d_i - w_{i-1}x_i) \quad (2.76)$$

where  $\alpha$  is a small factor usually defined between 0 and 0.1. This is to prevent phase ambiguity that would occur as the receiver is agnostic to what is the correct decision and thus this relationship needs to be maintained to accurately decode the signal.

### 2.3.2.6 Channel Equalization

Typically, an adaptive equalizer is implemented as the final stage of demodulation to compensate for any residual impairments that have not been fully compensated by the previous algorithms. The most used adaptive equalizer in optical networks is the decision-directed complex least mean square (LMS) algorithm [83]. Similar to the previous CPR algorithm, the LMS filter weights are iteratively updated as

$$\omega_{i+1} = \omega_i + 2\mu(d_i - y_i)x_i^* \quad (2.77)$$

where  $d_i$  is the decision symbol,  $\mu$  is the step size,  $x_i$  are the uncompensated symbols, and the compensated symbols are defined as

$$y_i = \omega_i^T x_i \quad (2.78)$$

### 2.3.2.7 Miscellaneous Receiver-Side DSP

Other receiver-side DSP include functions such as nonlinearity compensation as well as matched filtering and FEC decoding. Nonlinear compensation modules help reduce the effects of fiber nonlinearities which result from phenomenon such as self-phase modulation, cross-phase modulation, four-wave mixing, and nonlinear phase noise. The most common approach that is used for nonlinear compensation is digital backpropagation (DBP) [84]. Usually, nonlinear compensation can only be warranted in long-haul links due to the computational demands of the algorithms which has motivated research into innovative ML techniques to compensate for these nonlinear effects more efficiently [85-88].

As mentioned previously, matched filtering is often combined with pulse shaping at the transmitter. Typically, the matched filter is defined as the complex conjugate of the expected signal. It is often employed in the frequency domain. Matched filtering emphasizes the underlying signal in the presence of noise to maximize the signal-to-noise ratio (SNR) [74]. Finally, FEC decoding is the counterpart to the FEC encoding at the transmitter [89]. The FEC decoding uses the parity bits encoded in the message to detect errors. There are a variety of FEC codes that exist which fall under two major categories:

hard decision and, more recently, soft decision codes. The main disadvantage of using FEC is the need to sacrifice signal overhead which reduces the net data rate transmitted.

## **2.4 Machine Learning**

Machine learning has recently been explored and demonstrated as a potential solution to a variety of technical issues in optical networks. A large variety of research has been performed since approximately 2016 and is likely to continue into the future. In this section, a brief history of ML with an emphasis on how it has related to optics is discussed followed by ML basic operation principles and the associated innerworkings of common ML algorithms such as feedforward neural networks, convolutional neural networks, and long short-term memory networks.

### *2.4.1 History of Machine Learning*

Machine learning, in the modern sense, dates back as early as the 1940s when simple linear models were developed to make decisions based on an input and a target output. One of the most important building blocks of ML was developed by Warren McCulloch and Walter Pitts in 1943: the McCulloch-Pitts neuron was an early model of today's ML neurons that could decide between two target categories based on some input by determining whether some mapping function  $f(x, w) = \sum_{i=1}^n w_i x_i$  was positive or negative [90]. However, this required human input to set the weights unlike the automated weight optimization of today's approaches.

In the 1950s, the perceptron model was created by research psychologist Frank Rosenblatt who described the model as the “first machine which is capable of having an

original idea” due to its ability to learn associated model weights automatically – similar to and as an important precursor to the powerful ML techniques of today. The perceptron, which was based on certain ideas of the human nervous system and human learning patterns, showed extreme promise, and helped spark explosive growth regarding research for artificial intelligence as Rosenblatt and his colleagues demonstrated the learning capabilities of the perceptron via the perceptron-convergence theorem. This theorem stated that any linearly separable problem can be fully learned by a perceptron after a finite number of iterations thereby perfectly classifying all example inputs.

However, a book published by Marvin Minsky and Seymour Papert in 1969 that, while defining the strengths, clearly stated the weaknesses and limitations of the perceptron. One of the major limitations stated by the authors was the inability to model nonlinear logical functions such as the XOR or NXOR functions using neurons with implications that larger structures such as perceptrons suffered from the same limitations [91]. These supposed limitations drove research away from artificial intelligence and ML resulting in what is known as the “first winter of AI” [92]. Eventually, researchers proved that modelling these functions was possible: three-layer perceptrons were shown to be able to model an XOR logic function.

Machine learning gained traction again in the 1980s when researchers began to study the learning abilities of multi-layer neural networks. One specific major breakthrough was the development of the backpropagation learning algorithm [93]. Backpropagation resulted in efficient algorithmic learning by enabling gradient descent approaches via derivative calculations. However, the actual benefits of backpropagation and other related computational advances did not meet the advertised promises of

performance and reduced computational costs which resulted in another decrease in interest and funding for ML in the early 1990s resulting in what is known as the “second winter of AI.”

However, interest peaked for a third time in the early 2000s due to a variety of factors including the explosive growth of available data and the implementation and affordability of parallel processing. The sheer amount of available data not only enabled ML-based approaches but was also necessary to automatically process the sheer amount of available data. Meanwhile, multiple avenues explored parallel processing including Google’s MapReduce technology in 2004 [94] which also further facilitated the computational speeds required to handle the large amounts of data available. This parallel processing trend was also enabled by the increasing affordability of RAM at that time as well as the development of the GPU. Likewise, the development of “deep learning” algorithms which expanded upon the capabilities and performance of the original neuron- and perceptron-based approaches were demonstrated resulting in what is now known as deep neural networks (DNNs) – a key technology of the ML of today. By the mid to late 2000s, a plethora of research existed regarding DNNs which has propelled ML into the limelight since with famous researchers Geoffrey Hinton, Yann LeCun, and Yoshua Bengio (often referred to as the Godfathers of Artificial Intelligence) leading the way.

Since the mid to late 2000s, ML has become an important tool within many disciplines to solve the problems of today. Some disciplines include finance, healthcare, retail, and education due to its ability to efficiently create robust models from data. In more recent years, it has spread into a variety of other technical fields such as the communication industry. Optical communication, specifically, has shown that ML is

promising for multiple important applications including optical performance monitoring [95-97], impairment detection and identification [98-100], device design and system modelling [101, 102], network resource allocation [103, 104], and other functions such as nonlinear compensation. Note that this is only an extremely small subset of the available research in optical communication and this field is still considered in its infancy.

#### 2.4.2 *Machine Learning Basics*

ML is formally defined as “the study of computer algorithms that allow computer programs to automatically improve through experience [105]. ML methods are often divided into two major categories: supervised learning and unsupervised learning. Supervised learning entails supplying an algorithm with input-output pairs and the algorithm learns the corresponding mapping function between the input and output. The typical labels for data can be either categorical labels for classification applications or real-valued scalar labels for regression applications. Supervised learning is typically what is considered when discussing machine learning and includes common algorithms such as support vector machines (SVMs), feedforward neural networks (FFNNs), convolutional neural networks (CNNs), and long short-term memory (LSTM) networks.

Unsupervised learning involves algorithms that attempt to learn some mapping to sort data that have no target labels into clusters (or groups). Unlike supervised learning which requires an “expert” to define the input-output pairs, unsupervised learning is based around automated pattern recognition. One example of unsupervised algorithms includes the famous ICA algorithm which is often used to transform (or decompose) the latent space of some data set into its maximally independent components such as in the

case of blind source separation problems where the algorithm must separate a set of source signals from a mixed signal with little information about the source signals or mixing process. Another example of an unsupervised algorithm are autoencoders which can be considered a generalized nonlinear case of PCA [106] – these algorithms attempt to encode data by defining it as a lower-dimensional representation. Finally, there exist other specialized algorithms which are analogous to supervised learning techniques such as the one-class SVM.

In the following sections, important ML principles are discussed including desirable features of ML training paradigms such as the generalizability and the bias-variance trade-off. Likewise, techniques which are commonly used to enhance ML model performance and avoid phenomenon such as overfitting including hyperparameter selection and cross validation are discussed.

#### 2.4.2.1 Generalizability

The most important metric of an ML algorithm is the ability to demonstrate an equally high performance on both observed data and unobserved data – generalizability describes how well ML algorithms can perform on this unobserved data. ML algorithms are trained using observed data (referred to as the training set). The ML algorithm performs an optimization problem by attempting to minimize the training error (i.e., the difference between estimated and expected values of that training set).

The goal is to minimize the error of the unobserved data (referred to as the test set). This error is referred to as the test error or the generalized error. There are certain required assumptions regarding how the training and test sets are collected to accomplish this: ideally, the data sets are independent and identically distributed. However, in practice, ML algorithms usually exhibit a gap in performance between the training and test error since the ML algorithm is minimized respective to the training set exclusively. Therefore, ML algorithm performance is predicated on the ability to both minimize the training error and minimize the difference between the training and test errors, Fig. 2.12. These performance metrics correspond to two fundamental challenges of ML: underfitting and overfitting. Underfitting occurs when the model does not learn the underlying relationship between the input and the output resulting in a large training error. Overfitting occurs when the model learns specific features of the training data

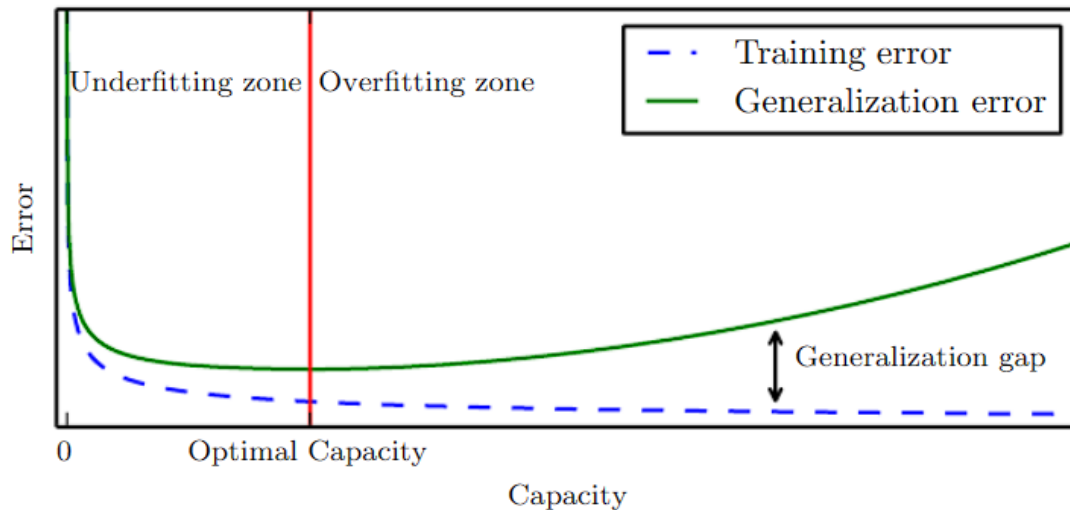


Figure 2.12: Training and validation example for ML algorithms. Underfitted models exhibit higher training error but relatively low validation accuracy while overfitted models exhibit low training accuracy but relatively high validation accuracy. Optimal fitting results in moderately low training error while maximizing validation accuracy [108].

which are not indicative of the actual distribution resulting in a large gap between training and test error.

The concept that is crucial to understand how underfitting and overfitting connect with the learning process of an ML algorithm is the capacity of said algorithm. Capacity is defined as the level of complexity that can be modeled by an algorithm. Models with a low level of capacity relative to the complexity of the task would fail to appropriately fit the training data resulting in an underfitted model while a model with a high level of capacity relative to the complexity of the task would learn features of the training data that are specific to that specific data resulting in an overfitted model. Therefore, it is imperative to design an ML algorithm with capacity that matches the complexity of the problem in mind.

Balancing the capacity of an ML algorithm with the complexity of some task is not trivial as the capacity is a loosely defined term. There have been efforts to quantify the capacity such as the Vapnik-Chervonenkis (VC) dimensions which have been proposed to quantify binary classifiers [107]. Today, this balance is usually developed heuristically by an expert who can guide the design process. The complexity is defined as the number of dimensions required to map between input and output.

#### 2.4.2.2 Bias-Variance Tradeoff

ML algorithms perform as an estimator which are defined by statistical properties that are innate to the trained model. Certain fundamental concepts such as bias and variance are important when characterizing the generalizability of the ML algorithms specifically

when mean squared error (MSE) is the metric for performance. Bias measures the expected deviation of some distribution from its actual distribution:

$$bias(\hat{\theta}_n) = \mathcal{E}(\hat{\theta}_n) - \mu \quad (2.79)$$

where  $\hat{\theta}_n$  is a vector containing the estimator outputs,  $\mathcal{E}(\hat{\theta}_n)$  is the expectation of the estimator outputs, and  $\mu$  is the mean of the actual distribution. An estimator is unbiased if  $bias(\hat{\theta}_n) = 0$  and is asymptotically unbiased if  $\lim_{n \rightarrow \infty} bias(\hat{\theta}_n) = 0$ . Variance measures the statistical deviation from the expected estimator value that is likely to occur for any specific sample:

$$var(\hat{\theta}_n) = \mathcal{E} \left[ \left( \hat{\theta}_n - \mathcal{E}(\hat{\theta}_n) \right)^2 \right] \quad (2.80)$$

Note that the standard deviation which is defined as  $SD(\hat{\theta}_n) = \sqrt{var(\hat{\theta}_n)}$  is also a useful metric for evaluating statistical characteristics.

To evaluate the best ML algorithm, it is important to evaluate how statistically the estimators compare. One of the most common metrics is the MSE which is a measure of the overall expected deviation between the estimator and the actual values:

$$MSE = \mathcal{E} \left[ \left( \hat{\theta}_n - \theta \right)^2 \right] \quad (2.81)$$

$$MSE = bias(\hat{\theta}_n)^2 + var(\hat{\theta}_n) \quad (2.82)$$

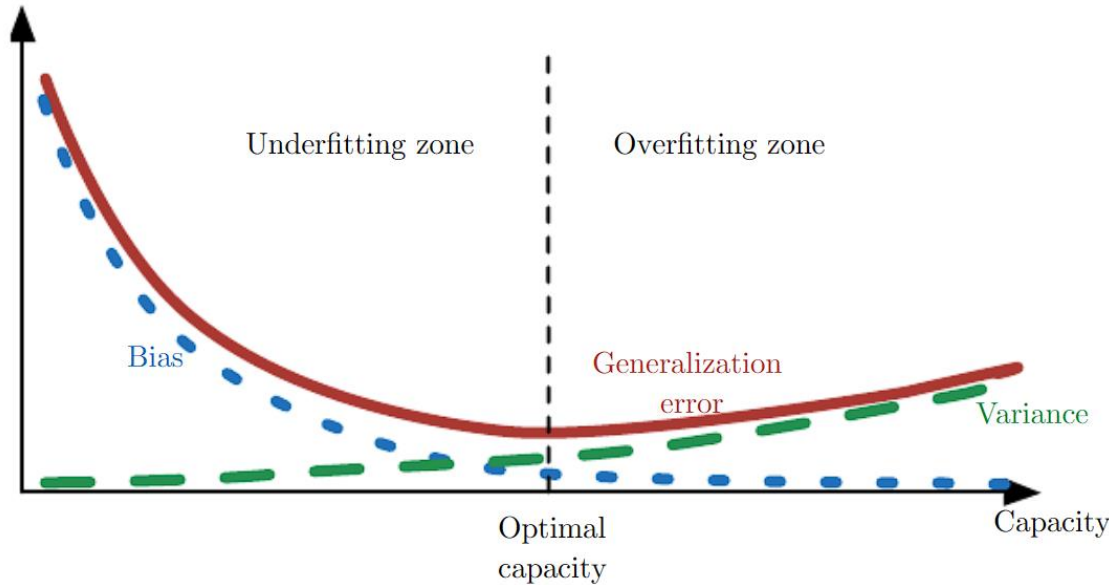


Figure 2.13: Relationship between model capacity and generalization error for ML models. Generalization error is composed of bias and variance errors. Optimal capacity is the point in which these metrics are jointly minimized [108].

Since the best estimators will minimize the MSE, it is apparent that one should choose an optimal estimator that jointly minimizes these two metrics – this is known as the bias-variance tradeoff for ML. Typically, increasing the capacity of an ML model results in increased variance and decreased bias, and vice versa for decreased capacity. An example of scaling capacity and how this affects the bias-variance tradeoff is shown, Fig. 2.13.

#### 2.4.2.3 Regularization

The complexity of the data is oftentimes unknown as ML algorithms are frequently applied to tasks where there is not readily available or readily understood analytical models. Therefore, choosing the correct capacity for these tasks is not transparent resulting in the use of higher capacity models than actually needed to ensure that the ML algorithm is capable of learning the underlying relationships. However, this puts the

model at risk of overfitting. Regularization is one method to manage the risk of overfitting without compromising the capacity of the model. Formally, regularization is defined as “any modification we make to a learning algorithm that is intended to reduce its generalization error but not its training error” [108].

One common method of implementing regularization is by adding a penalty to the cost function. For example, when performing a linear regression while using an L2 norm regularization, the cost function may be formed such that [108]:

$$J(\omega) = MSE_{train} + \lambda \omega^T \omega \quad (2.83)$$

where  $\lambda$  is the regularizing coefficient and  $\omega$  is a vector containing the model weights. Since the training process attempts to minimize the cost function, the regularizing term creates a tradeoff between fitting the data and reducing the magnitude of the weights resulting in either smaller slopes in the gradient descent or fewer overall features used

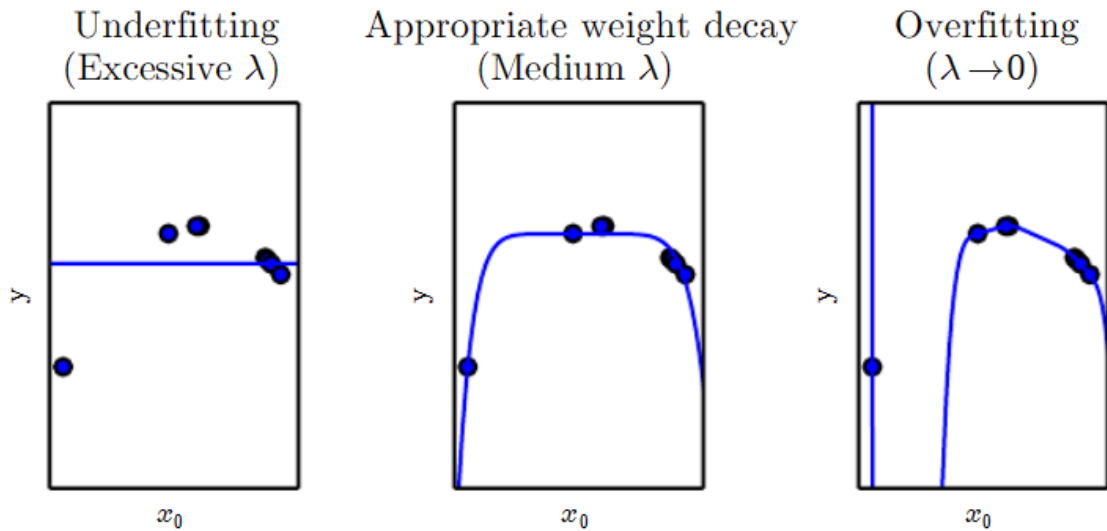


Figure 2.14: Polynomial regression fitting example using quadratic data and an ML model with degree 9. The regularization hyperparameter enables the over-capacity model to sufficiently fit the data as it controls the degree of learning possible [108].

within the mapping. An example of a polynomial fitting using varying levels of regularization to control overfitting is demonstrated in Fig. 2.14.

#### 2.4.2.4 Hyperparameters and Validation Sets

When designing an ML algorithm, there are a variety of settings that can be tuned to control how the algorithm operates – these are called hyperparameters. These parameters are either preset due to the difficulty of learning such a parameter or are separate from the learning process as they are not adapted during training and in fact are often used to guide the training process. Common hyperparameters may include the optimization algorithm used, the learning rate of the algorithm, how many optimization iterations that training occurs over, etc. Regularization is one such hyperparameter as well. Note that it is possible, in certain circumstances, to design a learning algorithm that can optimize the hyperparameters of another algorithm during training; however, this is not feasible for capacity-defining hyperparameters as the learning process would always choose to overfit since it would result in the “best fit” for that training data set. Similarly, other hyperparameter cannot often be optimized using the training set as the training accuracy does not correlate to the model’s ability to generalize – this is the job of the test set.

Validation sets are utilized to remove this limitation. The validation set is a third batch of data analogous to the training and test sets. Validation sets allow for the generalizability of the model and its hyperparameter selections to be evaluated during training while ensuring that the completed model can still be independently evaluated using the test set. The validation set is obtained by splitting the training set. The typical split is 80%-20% with 80% for training and 20% for validation.

#### 2.4.2.5 Cross-Validation

ML algorithms are oftentimes limited by the amount of data that can be collected for real world applications – data collection can be a slow, arduous process or the data may be difficult to collect. Therefore, splitting a data set into fixed training, validation, and test sets may result in data sets that are small thereby limiting the statistical certainty of the trained model. Cross-validation is a method to alleviate this issue. In a  $k$ -fold cross validation, the data is divided into  $k$  non-overlapping sets. The training is repeated  $k$  times with each cross-validation set used to compute the validation accuracy while the rest of the data is used for training the model. An aggregate validation error is computed by averaging the test errors across all trials.

#### 2.4.3 *Types of Machine Learning Algorithms*

This section will highlight common ML algorithms that are often used in today's literature. Since many ML applications involve regression or classification, this section will focus on these supervised learning algorithms including feedforward neural networks, convolutional neural networks, and long short-term memory networks. Support vector machines will be discussed relative to both supervised and unsupervised learning applications.

##### 2.4.3.1 Support Vector Machines

Support vector machines are one of the most well-known and influential algorithms in machine learning. SVMs are traditionally used to separate one type of data from another [109]; however, they have been modified and applied to other applications such as multi-

class classification and regression. The traditional SVM which performs a two-class classification operates by the linear function:

$$\omega^T x + b, \quad \text{if } \begin{cases} \omega^T x + b < 0, & \text{then Class 1} \\ \omega^T x + b > 0, & \text{then Class 2} \end{cases} \quad (2.84)$$

where  $\omega$  is the transformation that is being estimated and  $x$  is the input.

However, since this function is linear with respect to both  $\omega$  and  $x$ , it is insufficient to model complex, nonlinear relationships. By using a technique called the “kernel trick,” this limitation can be bypassed. The kernel trick first implies that the linear function of the SVM can be rewritten as a sum of functions [108]:

$$\omega^T x + b = b + \sum_{i=1}^m \alpha_i x_i^T x_i \quad (2.85)$$

where  $x$  is the training example, and  $\alpha$  is a vector of weight coefficients. This can be further extended by replacing  $x$  with  $\phi(x)$ :

$$\omega^T x + b = b + \sum_{i=1}^m \alpha_i \phi_i(x)^T \phi_i(x) \quad (2.86)$$

where  $\phi(x)$  is a basis function which may allow for transformation of the input into a higher dimensional state where linear regression is possible [110]. Note that this new function is nonlinear with respect to  $x$ , but still linear with respect to  $\omega$  and  $\phi(x)$ . Computationally, however, this is still prohibitively expensive as it requires one to calculate the basis functions with respect to the number of dimensions of the transformation.

Finally, the kernel trick observes that the dot product of the basis functions can be rewritten as a kernel evaluation to drastically reduce the number of computations required as this circumvents the need to transform individual inputs separately. The most common kernel evaluation is the Gaussian kernel which is defined as:

$$k(x_1, x_2) = \exp\left(\frac{(x_1 - x_2)^2}{2\sigma^2}\right) \quad (2.87)$$

where  $x_1$  and  $x_2$  are the input samples, and  $\sigma$  is a scaling parameter. The Gaussian kernel, which corresponds to a dot product in an infinite dimensional space, is also known as the radial basis function kernel [108]. Note that SVMs are not the only technique that can be enhanced using the kernel trick. In fact, an entire class of algorithms exist which are categorized as “kernel machines” or “kernel methods” [111, 112].

One of the major drawbacks of kernel machines is that the computational complexity of evaluating the decisions scales linearly with the size of the training set. SVMs have mitigated this effect by selecting a small subset of training samples to be used to calculate the decision threshold – these are called the support vectors and they are the points which define and are located closest to the separating hyperplane. Likewise, the hyperplane is defined such that the separation between it and the support vectors is maximized.

While the typical application of SVMs is that of a supervised, two-class classification, i.e., separating one known type of data from another known type of data, there have been a variety of techniques employing SVM which expand this role into different applications such as regression-based SVMs and multi-class classification

SVMs. One other type of unique SVM which is of interest to the ML community is the one-class SVM. The job of this algorithm is to separate a known distribution of data from all other types (including unknown types) of data. Functionally, this is performed by generating a decision hyperplane that fully encompasses the data set – anything inside the hyperplane is classified as the expected class and any data which falls outside of the hyperplane is classified as the unknown class.

#### 2.4.3.2 Feedforward Neural Networks

Neural networks have their origins rooted in attempts to find mathematical representations of biological information processing systems [110]. A variety of models fall under the umbrella of neural networks including one of the most simple and common implementations – the FFNN. Note that this also includes other deep-learning variations. The FFNN is commonly referred to as the DNN. It is also sometimes referred to as a multi-layer perceptron – this is a misnomer due to differing activation functions.

FFNNs are regularly used for classification and regression as they function incredibly well at approximating functions. FFNNs, depicted in the form of a directed graph, process information in one direction – from the input layer to the output layer with hidden layers in between for intermediate computations, Fig. 2.15. Each layer is composed of a set of nodes which perform a nonlinear transformation on the input – these are called the activation functions. Common activation functions include the sigmoid, hyperbolic tangent, rectified linear unit (ReLU) as well as many others, Fig. 2.16. The nonlinear nature of the activation function is crucial for the FFNN to learn nonlinear models. Note that deep learning refers to neural networks with multiple hidden layers as

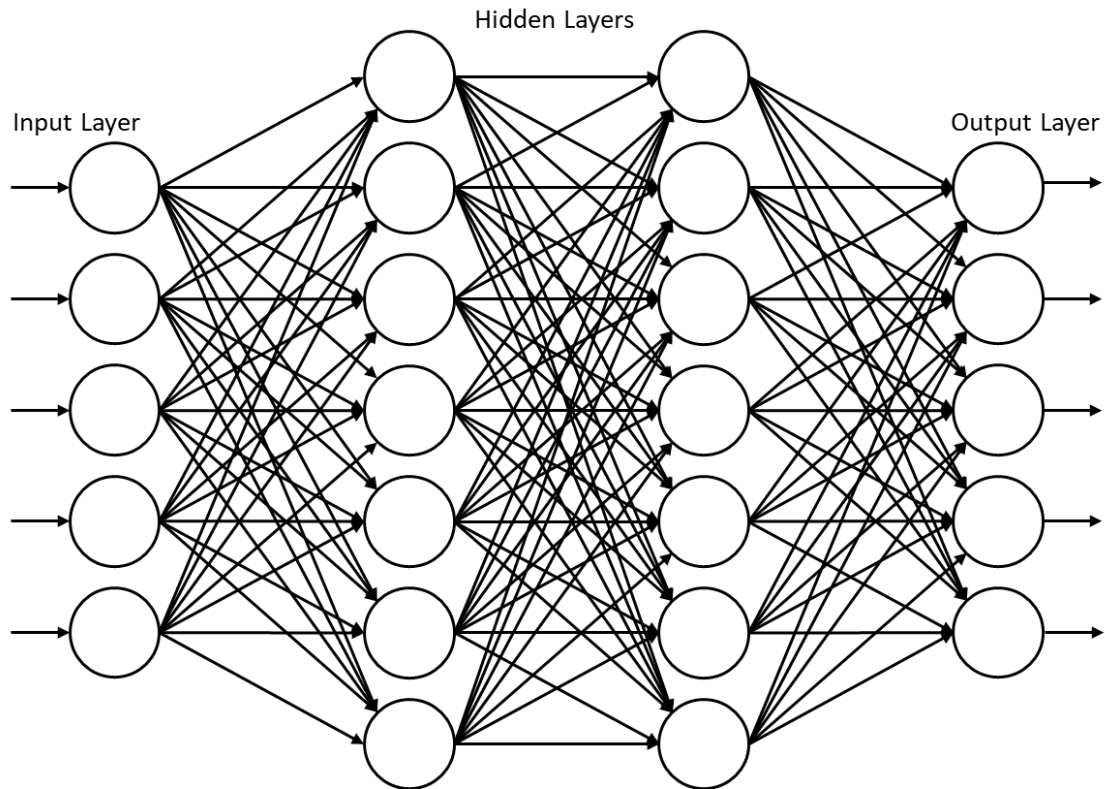


Figure 2.15: FFNN with two hidden layers. Each node in the hidden and output layers acts as an activation function, or nonlinear transformation. Inputs of each hidden and output layer are a weighted multiplication of all outputs from the previous layer.

increasing the number of hidden layers increases the complexity of the model allowing for more complex relationships to be learned.

FFNNs are trained using gradient descent which is a common approach for many optimization problems. However, while FFNNs offer the advantage of nonlinearities, this results in most effective loss functions becoming non-convex thereby requiring to be optimized using iterative methods to find local minimums instead of, for example, the global minimum convergence of linear optimizers. Note that common loss functions for neural networks include cross-entropy for classification-based problems and MSE for regression-based problems. Common output layer methodologies for performing

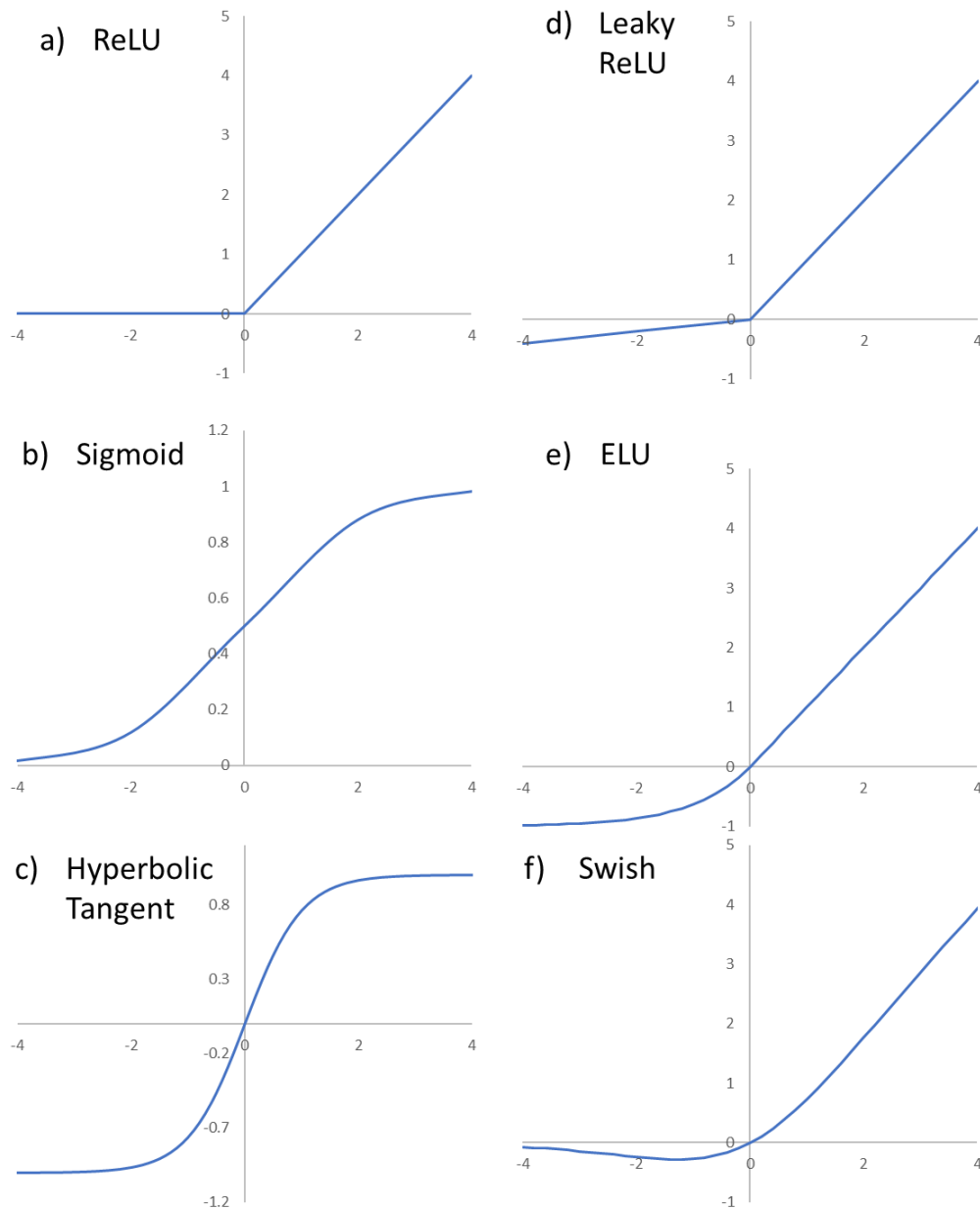


Figure 2.16: Activation functions used in ML. Selecting the correct activation function depends on the application. ReLU generally demonstrates sufficient performance and is most often used today. Swish is a lesser-known activation function discovered by researchers at Google with advantages over ReLU in deeper networks.

classification and regression are discussed in the following section. Likewise, regularization functions such as the L2 regularization discussed previously are commonly implemented to limit overtraining of these networks.

### 2.4.3.3 Convolutional Neural Networks

Convolutional neural networks are a subset of deep learning algorithm commonly used for classification and regression that extends on the FFNN by performing a feature extraction process via automated, optimized filters. CNNs are most popularly known for their ability to analyze images, a 2-dimensional grid-like topology [113]. However, there are variants of CNNs which can be applied to multi-dimensional inputs such as the 1-dimensional CNN which processes array topologies, the 3-dimensional CNN which is applied in applications such as video processing (i.e., 2-dimensional images as it spans across the third “time” dimension). It can also be extrapolated to higher, N-dimensional cases; however, the applications are more abstract when compared to the traditional uses.

A CNN consists of an input layer, feature extraction layer (FELs), fully connected layer (FCL), and an output layer, Fig. 2.17. The FEL consists of a convolutional layer, nonlinear transformation layer, and pooling layer. Note that FELs may be cascaded to further enhance the input data. Convolutional layers perform a convolution with the input and a filter that is iteratively optimized during training to extract some specific

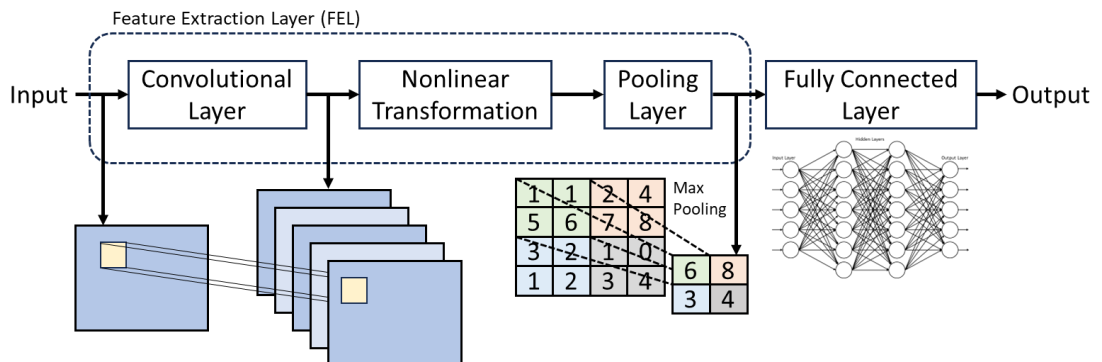


Figure 2.17: Typical CNN structure which maps from an N-dimensional input to a feature map via convolutions, nonlinear transformations, and pooling. Feature maps are then used as the input to a FFNN to generate a relationship between these feature maps and the parameter of interest.

feature from the data. The convolution operation results in a feature map which precisely records not only the feature of interest, but also the location within that input. Examples of simple features in the case of an image may include edges, shapes, contours, colors, etc. In more advanced implementations, the features can become incredibly complex and arbitrary with a deep learning model. The output of the convolutional layer is then passed through a nonlinear transformation as this enables each FEL to function independently of the subsequent and future layers – without a nonlinear element, any cascaded linear layers are equivalent to some single layer thereby severely reducing the possible modeling complexity. Finally, pooling layers then reduce the size of the feature map by downsampling the input. There are two common approaches to pooling: max pooling and average pooling. Max pooling calculates a series of maximum values of the input over a small, sliding window while average pooling instead calculates the average. Pooling layers result in multiple benefits such as reducing the required model complexity by reducing the size of the data as well as offering some level of location invariance to the input. Location invariance suggests that small shifts in the location of a feature will have minimal impact on prediction error.

The FEL is then flattened to a 1-dimensional array and used as the input to the FCL. Since the FCL is analogous to the FFNN, it also serves as an effective function approximator by performing an abstract mapping between FEL-extracted features and the expected training target values. The output layer which finalizes the FCL usually consists of a Softmax activation function to generate a probability distribution for the decision nodes in classification applications [108]:

$$\sigma(\vec{z})_i = \frac{e^{z_i}}{\sum_{j=1}^N e^{z_j}} \quad (2.88)$$

where  $z_i$  are individual input vector elements and can assume any real value. For regression applications, a neuron is used to combine the output of the FCL:

$$\tilde{y} = \sum_{i=1}^N W_i x_i + b \quad (2.89)$$

where  $y$  is the resulting estimation from the output layer,  $W_i$  and  $x_i$  are the associated weights and inputs passed from the hidden layer (where  $i$  corresponds to each  $N$  number of hidden neurons). Note that the output layer is traditionally an unbounded, linear function as nonlinear activation functions such as the sigmoid, hyperbolic tangent, and ReLU limit the range of the output which is an often-undesirable feature.

#### 2.4.3.4 Recurrent Neural Networks

Recurrent neural networks (RNNs) are a specialized type of neural network which have feedback connections to supply an element of memory to the machine learning model [114]. This memory element gives an advantage over conventional FFNN approaches in applications involving systems with correlated features across multiple samples. Examples include time series prediction, speech recognition and language processing. Despite demonstrating better performance than FFNNs for these applications, RNNs are notoriously difficult to train due to the vanishing/exploding gradient problem which occurs as the combination of feedback loops and training backpropagation will cause smaller weights to shrink exponentially and larger weights to explode exponentially. This

phenomenon is further exacerbated by lengthening the sequence of the input and it is difficult to mitigate.

The LSTM, a type of RNN which was designed to model both short- and long-term dependencies in an input, is the most implemented type of RNN. This is accomplished using LSTM cells, Fig. 2.18. LSTM cells have what is known as the “cell state” which is the main element of the LSTM which determines the relevance of previous information thereby adding memory to the architecture. The cell state is controlled by three gates which perform operations on the input to the LSTM cell. The first gate is the “forget gate” which is used to decide to pass information to the cell state from the previous time step or forget it:

$$f_t = \sigma(W_f \cdot [h_{t-1}, x_t] + b_f) \quad (2.90)$$

The sigmoid function results in a number between 0 and 1: if  $f_t = 0$  then forget

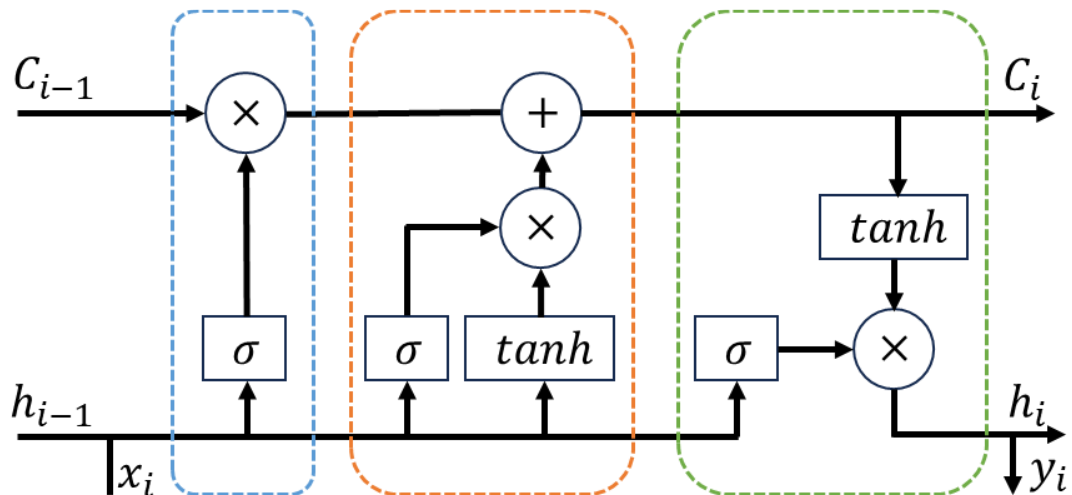


Figure 2.18: Structure of an LSTM cell. There are three main logic gates. The forget gate, depicted in blue, decides if information is passed to the cell state,  $C_i$ . The input gate, labeled orange, quantifies the importance of new information. The output gate, shown in green, determines the output of the LSTM cell based on the cell state.

everything, and if  $f_t = 1$  then forget nothing. Next, the “input gate” is used to quantify the relevance of the new information:

$$i_t = \sigma(W_i \cdot [h_{t-1}, x_t] + b_i) \quad (2.91)$$

$$\tilde{C}_t = \tanh(W_C \cdot [h_{t-1}, x_t] + b_C) \quad (2.92)$$

where  $i_t$  measures the importance of new information carried by the input and  $\tilde{C}_t$  generates a candidate vector of new, potential values – these two steps are combined and added to the current state resulting in the following change in the cell state after the first two gates:

$$C_t = f_t * C_{t-1} + i_t * \tilde{C}_t \quad (2.93)$$

Finally, the “output gate” determines the output of the LSTM cell. The output, which is based on the cell state, is filtered by running it through another sigmoid function to decide what part of the cell state will be included in the output as well as altering the cell state via another hyperbolic tangent function:

$$\sigma_t = \sigma(W_o \cdot [h_{t-1}, x_t] + b_o) \quad (2.94)$$

$$h_t = \sigma_t * \tanh(C_t) \quad (2.95)$$

Note, that the hyperbolic tangent ensures that the cell state is limited to a reasonable range of -1 to 1. Without this function, the cell state can become very large or small over time thereby limiting the learning potential of the network as mentioned previously with vanishing and exploding gradients.

# **MACHINE LEARNING FOR TDECQ: ACCELERATING PAM-4 TRANSCEIVER CHARACTERIZATION**

Recent transitions to the PAM-4 modulation format have increased the throughput over that of traditional PAM-2 direct detect optical links without doubling bandwidth requirements – this has been a necessary transition to meet the ever-increasing data rate requirements [115, 116]. However, increased transmitter complexity has necessitated more robust test and measurement techniques to ensure that optical networks are able to meet performance metrics such as reaching sufficiently low bit error rate (BER) thresholds. To meet these metrics, transceivers are tested to assure these components can perform at expected levels. Still used today, a legacy PAM-2 interoperability metric, the transmitter and dispersion penalty (TDP), requires comparing a measured BER with that of an ideal transmitter. Such measurement unfortunately is both costly and time consuming. Simple PAM-2 eye masks were for a long time a popular alternative to gauge interoperability. However, alongside the presence of multiple eyes, equalizing links with PAM-4 signaling render these traditional metrics less effective.

The IEEE has moved away from these traditional metrics to the more link-performance predictive TDECQ metric which was implemented in the IEEE 802.3 standard. As outlined in Appendix A, TDECQ calculates the additional noise required to reach a target symbol error rate (SER) using an iterative statistical process [117-119]. However, since the TDECQ process is complex and iterative, it requires significant computational effort. Thus, the process leaves room for improvement regarding efficiency.

Machine learning has recently seen significant popularity in optical communication with respect to applications such as optical performance monitoring, failure and fault management, impairment identification, etc. due to its ability to efficiently model systems using abstract inputs (such as constellation diagrams or eye diagrams) or with no defined model. It has previously been shown the feasibility of machine learning for TDECQ estimation [120, 121] specifically for real-time oscilloscopes. TDECQ measurements can be significantly accelerated using machine learning by establishing an equivalent model that circumvents the iterative nature of the conventional approach.

In this section, we expand upon these works by demonstrating an extension of capability for estimating the TDECQ via ML - using both eye diagram and raw waveform analysis. Likewise, the method will be shown to be capable of determining the limiting transceiver penalty which degrades the TDECQ – this will be referred to as impairment identification. Finally, the difference in results when the acquisition engine is changed from real-time to equivalent time oscilloscopes will be documented.

### **3.1 Methodology**

To implement a robust machine learning solution, one must collect sufficient training data. Therefore, the methodology is divided into two distinct sections: the experimental setup which details the testbed used for collecting the training and test data, and the machine learning overview which details the ML architectures used within.

### 3.1.1 Experimental Setup

The experimental setup, shown in Fig. 3.1(a), consisted of a PAM-4 transmitter which includes a 1310 nm DFB laser that was externally modulated using an EOSpace Lithium Niobate modulator. The modulator was driven by a Tektronix 70001A arbitrary waveform generator (AWG) and biased using a Thorlabs MBX bias controller. The output of the AWG was amplified using an SHF 807 linear amplifier to obtain high modulation depth. The transmitter employed a PAM-4 pattern known as the short stress pattern random quaternary (SSPRQ) per the IEEE 802.3 standard for TDECQ.

The optical signal was split by a 50/50 fiber optic splitter and the optical signal was captured using both a Tektronix DPO70E1 optical to electrical converter connected directly to the Tektronix DPO73304D real-time oscilloscope as well as an 80C20 optical

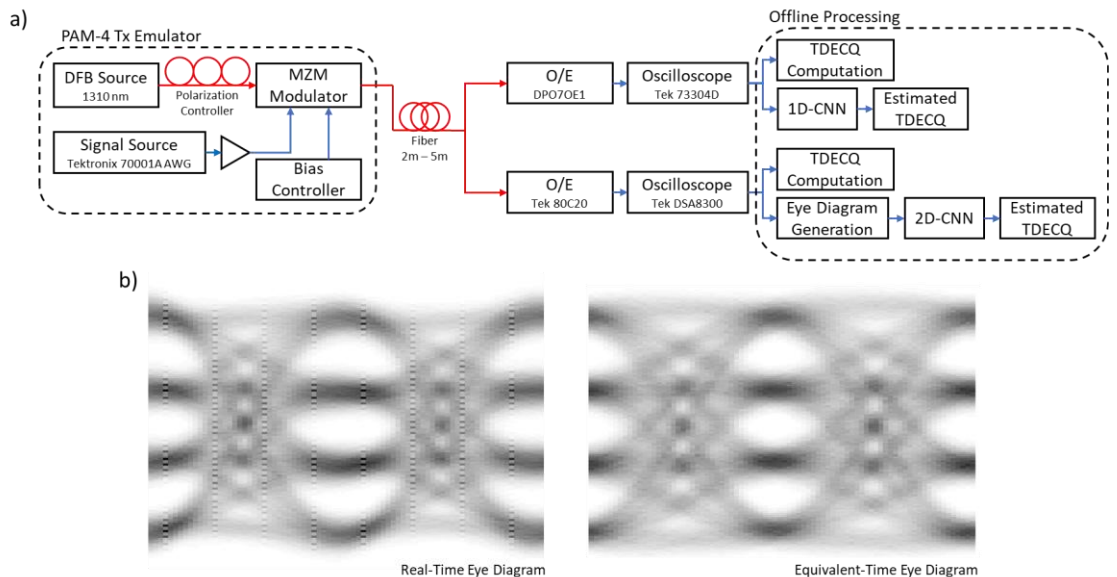


Figure 3.1: (a) The experimental setup consists of transmitter configured to emulate a variety of impairments, (b) example eye-diagrams from a real-time and equivalent-time oscilloscope from similar setup configurations. Quantization effects are visible in the real-time eye-diagram. Note that intermediate values are interpolated for eye-diagram plots.

sampling module connected to a DSA8300 equivalent-time oscilloscope. This dual-oscilloscope setup is to ensure consistency between measurements and comparisons between the waveforms captured for each oscilloscope. Example eye diagrams from each oscilloscope type are shown in Fig. 3.1(b). Quantization effects can be seen in the real-time eye diagram which can be attributed to the lower bit resolution – the real-time oscilloscope has 8-bit resolution unlike the higher bit resolution of the equivalent-time oscilloscope. The waveforms received by each oscilloscope are processed offline to generate a TDECQ using the conventional IEEE mandated procedure. These TDECQ values are used as a training target for the ML algorithms as well as a comparison value for testing.

The experimental setup was used to generate three distinct impairments that exist within PAM-4 transmitters, Fig. 3.2. Bandwidth limitations were emulated using a Gaussian filter at the AWG whose bandwidth varied between 9 GHz and 20 GHz. SNR was varied from 15 dB to 30 dB by digitally adding additive white Gaussian noise (AWGN) to the signal. Nonlinear signal compression effects were implemented by varying the MZM bias (non-null point) creating unequal PAM-4 eyes. Impairments were generated such that the investigated TDECQ values uniformly spanned 2 to 5 dB which covers the common range of values per the IEEE 802.3 standard. The complete data set included ~750 waveforms. Comparable data sets were taken using each oscilloscope type.

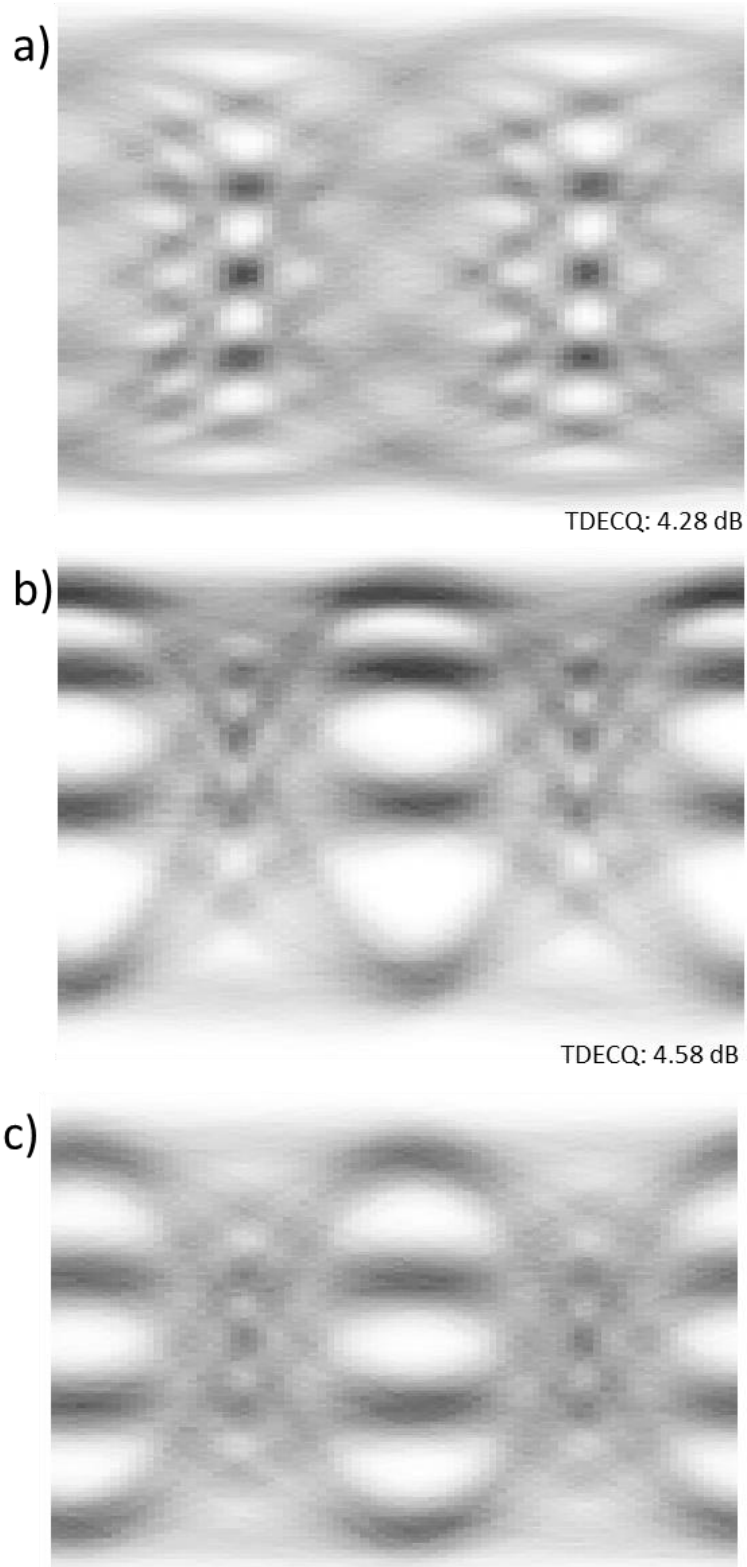


Figure 3.2: Examples eye-diagrams impacted by impairments with varying severity: (a) bandwidth limitations which was generated using a filter at the transmitter, (b) signal compression which resulted from improper MZM biasing, (c) SNR degradations by digitally loading AWGN.

### 3.1.2 *Machine Learning Architecture*

To bypass the computationally intensive TDECQ process, two ML algorithms were developed which use either the eye diagram or the raw waveform. The eye diagram is a conventional measurement used to qualify the performance as the transmission quality is readily identified by a variety of eye measurements such as the rise and fall times, 1 and 0 levels, optical modulation amplitude, extinction ratio, etc. In fact, some of these measurements are crucial for the TDECQ measurement. Thus, eye diagrams are often readily available due to their usefulness. Raw waveforms were also explored as an input for estimating the TDECQ as this avoids the additional preprocessing required to generate the eye diagram with a trade-off of increased ML complexity. The raw waveform should also allow for more robust measurement by reducing visual artifact that occur in the eye diagram resulting from quantization.

Separate machine learning algorithms were developed for the eye diagram and waveform methodologies. This was so that the developed algorithm was tailored to the form of the input: eye diagrams consisted of 80x160 histogram matrices and waveforms consisted of a vector with 262,140 samples. Note that these algorithms were deployed and tested on both real- and equivalent-time oscilloscopes which use distinct sampling methodologies and thus have vastly different inherent noise characteristics.

The CNN, a subset of deep learning algorithms, was the chosen machine learning approach due to its popularity and success in image processing applications. CNNs automatically optimize filters to extract features from the input image [122]. CNNs typically consist of an FEL and a FCL. The FEL consists of convolutional layers and

pooling layers. Convolutional layers perform a convolution with the input and a filter that is designed to extract some specific feature. These filters are iteratively optimized during training for use during operation. The convolution operation results in a feature map which precisely records features and their locations within the input for that specific convolution layer. Pooling layers then reduce the size of each feature map by down sampling (typically by calculating an average or max for a local set of pixels). Pooling layers have multiple benefits which include reducing the required network complexity via spatial reduction as well as introducing a degree of feature location invariance. Note that there is a nonlinear activation function between convolutional and pooling layers that enables nonlinear modeling. Multiple FELs can be connected in series to accentuate feature extraction.

The FCL, which is connected to the output of the FEL, is a structure where the neurons of one layer are connected to everyone neuron of the subsequent layer. Thus, a major distinction between convolutional layers and FCLs are that the convolutional layers are instead locally connected. The FCL has the role of mapping the feature map (i.e., output of the FEL) to the expected training targets. This relationship is usually incredibly complex and often nonlinear. Note that the input to the FCL is a vector formulated by flattening the output of the FEL. The FCL connects to a Softmax layer and subsequent output layer which, for the purpose of TDECQ estimation, is a singular regression node. Note that for impairment identification, the output layer would be replaced with N classification nodes where N is the number of classification categories.

The CNN architecture depicted in Fig. 3.3(a) was used to estimate TDECQ and identify the most likely impairment degrading the performance directly from an eye

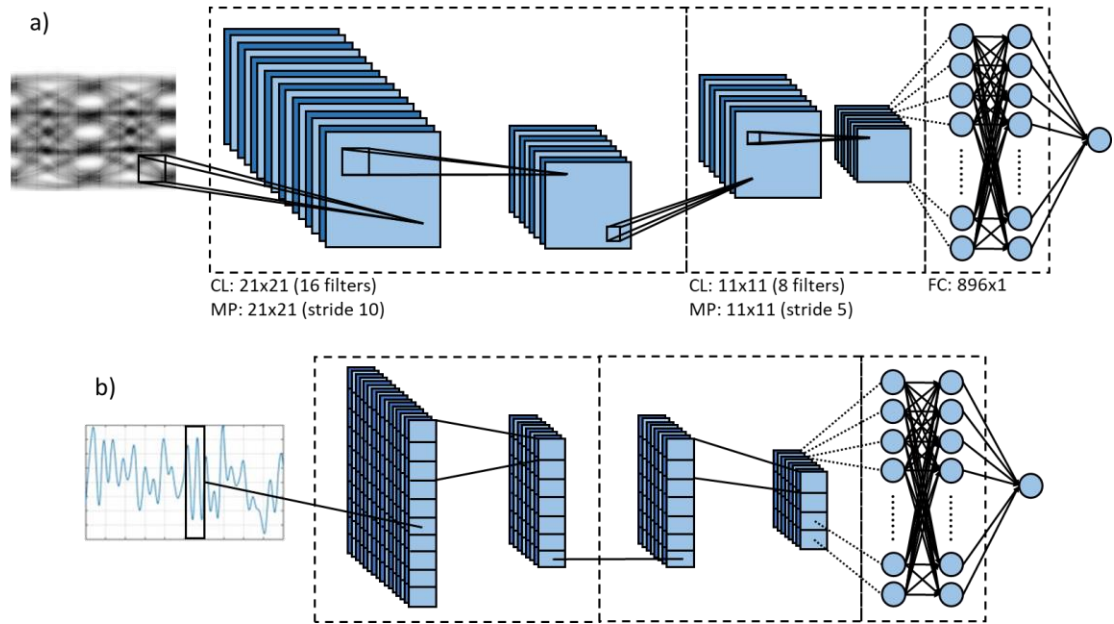


Figure 3.3: (a) Two-dimensional CNN architecture which uses eye-diagrams as input. The input image is an  $80 \times 160$  matrix representing a histogram of the captured eye diagram. (b) One-dimensional CNN architecture which uses the digitally acquired waveform as the input. The raw waveforms consisted of consisted of 262,140 samples which correspond to an oversampling rate of 8.

diagram. As the input is 2-dimensional, this method will henceforth be referred to as 2D-CNN to distinguish from future discussed methodologies. The same 2D-CNN architecture was used for both TDECQ estimation and impairment identification because the feature extraction was well-tuned to the respective input. This specific architecture consists of two FELs with hyperparameters of filter sizes, number of filters, and strides as shown. Max pooling was used. The input to the 2D-CNN is an  $80 \times 160$  matrix representing a histogram of the captured eye diagram. The 2D-CNN was trained using  $\sim 2300$  waveforms with TDECQs ranging from 2 dB to 5 dB and spanning 3 distinct impairments which were emulated on the experimental testbed.

For the waveform-based approach, a specialized one-dimensional CNN (1D-CNN) was implemented where filters are applied along one dimension of the waveform.

The 1D-CNN has seen considerable merit when used for time-series data [122]. The architecture consists of three FELs, Fig. 3.3(b). Max pooling was used. The input to this 1D-CNN was an array with 262,140 values representing the captured, sampled digital waveform. The same data set was used to train the 1D-CNN as was used for the 2D-CNN to allow for fair comparison between the two methodologies. Likewise, both methods were tested using both real- and equivalent-time oscilloscope data.

## 3.2 Results

This section highlights key performance comparisons between real- and equivalent-time oscilloscopes for eye-diagram-based and signal-based methods. Performance comparisons are performed relative to the ML methodology and type of scope. Signal-based methods are emphasized to determine whether the statistics of the sampled signal are representative for TDECQ. Impairment identification is demonstrated using the eye-diagram based approach. Training nuances such as ML management of oscilloscope noise characteristics are demonstrated as well.

### 3.2.1 TDECQ Estimation via 2D-CNN

Figure 3.4 shows the correlation between conventionally measured TDECQ and ML estimated TDECQ for both real- and equivalent-time oscilloscopes when using eye diagrams as the input feature. Similar performance between real- and equivalent-time oscilloscopes is demonstrated with an average TDECQ discrepancy of  $\leq 0.12$  dB. The tested equivalent-time oscilloscope outperforms the real-time oscilloscope within the high TDECQ range ( $\geq 3$  dB). This is likely due to the quantization effects that occur due to the limited bit resolution of the real-time oscilloscope as discussed previously.

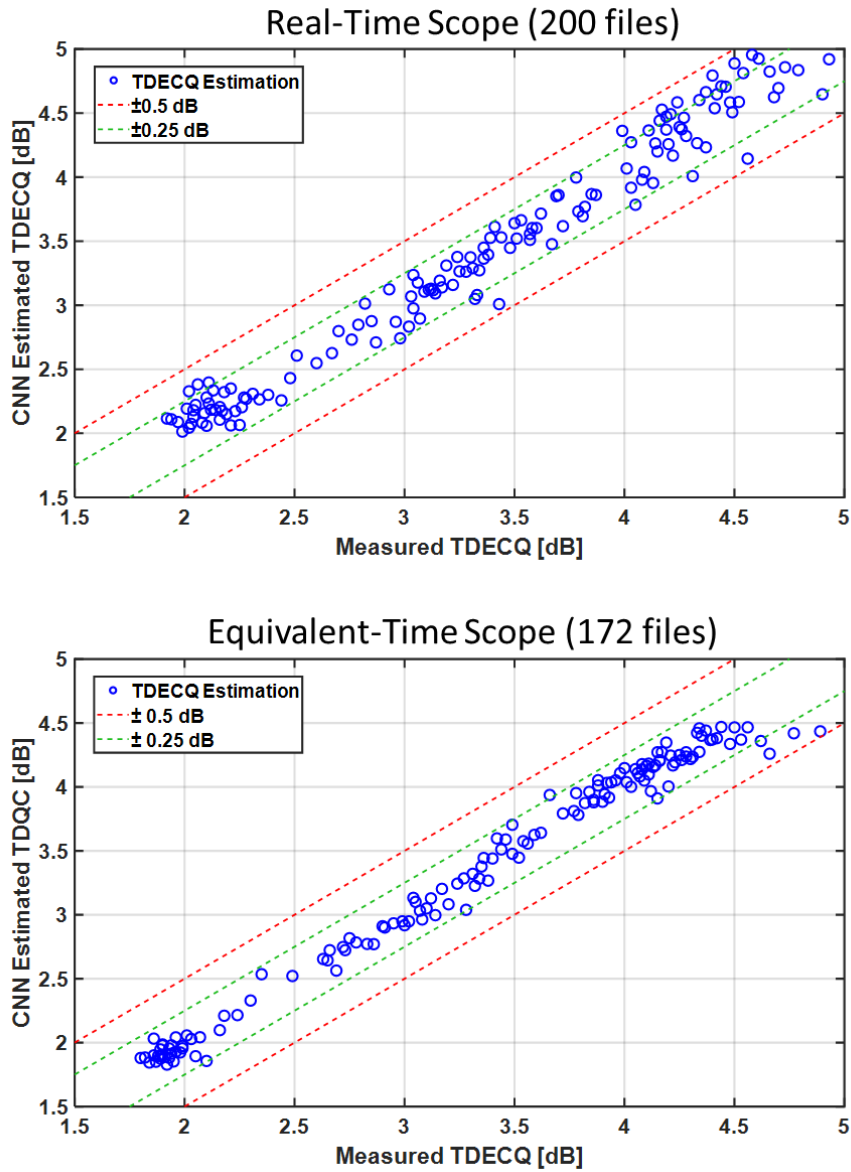


Figure 3.4: Performance comparison between real- and equivalent-time oscilloscopes for eye-diagram-based TDECQ estimation. Equivalent-time oscilloscope demonstrates a better average performance for entire tested TDECQ range.

Quantization artifacts within the eye diagram act as a type of noise and thus may obscure features that the ML would otherwise detect to create a more robust model. The signal quality for the lower TDECQ range ( $\leq 3$  dB) is high; therefore, there are few or no

features to obscure proper TDECQ estimation resulting in more equal performance within this range.

### 3.2.2 TDECQ Estimation via 1D-CNN

Figure 3.5 shows the correlation between conventionally measured TDECQ and ML estimated TDECQ for both real- and equivalent-time oscilloscopes when using the raw waveform as the input. The waveform-based method demonstrates similar performance for both oscilloscopes across the 2 dB to 5 dB TDECQ range. Both oscilloscopes performed best at low TDECQ values with  $\leq 0.07$  dB average discrepancy for  $\text{TDECQ} \leq 3$  dB. A marginal increase in average discrepancy to  $\leq 0.11$  dB occurred for  $\text{TDECQ} \geq 3$  dB. It is clear to see that, unlike the eye-diagram-based method, there is no difference in maximum error between the two oscilloscopes. Thus, the image artifacts that may have resulted in higher error for the eye-diagram-based method has no discernible effect on the waveform-based approach demonstrating an advantage with respect to the different ML methodologies.

### 3.2.3 Impairment Identification via 2D-CNN

The confusion matrix of Fig. 3.6 shows 100% accuracy for all tested impairment cases when the TDECQ is  $\geq 3$  dB. Note that a TDECQ of  $\leq 3$  dB is the criteria for compliance per the IEEE 802.3 standard. This proves that ML can provide accurate impairment identification when the waveform is clearly impaired. The ML architecture required little adjustment between TDECQ estimation and impairment identification demonstrating that the CNN is well tuned to analyze the system input. It is important to note that while these impairments are not exhaustive, they do capture a good spread of possible effects on the

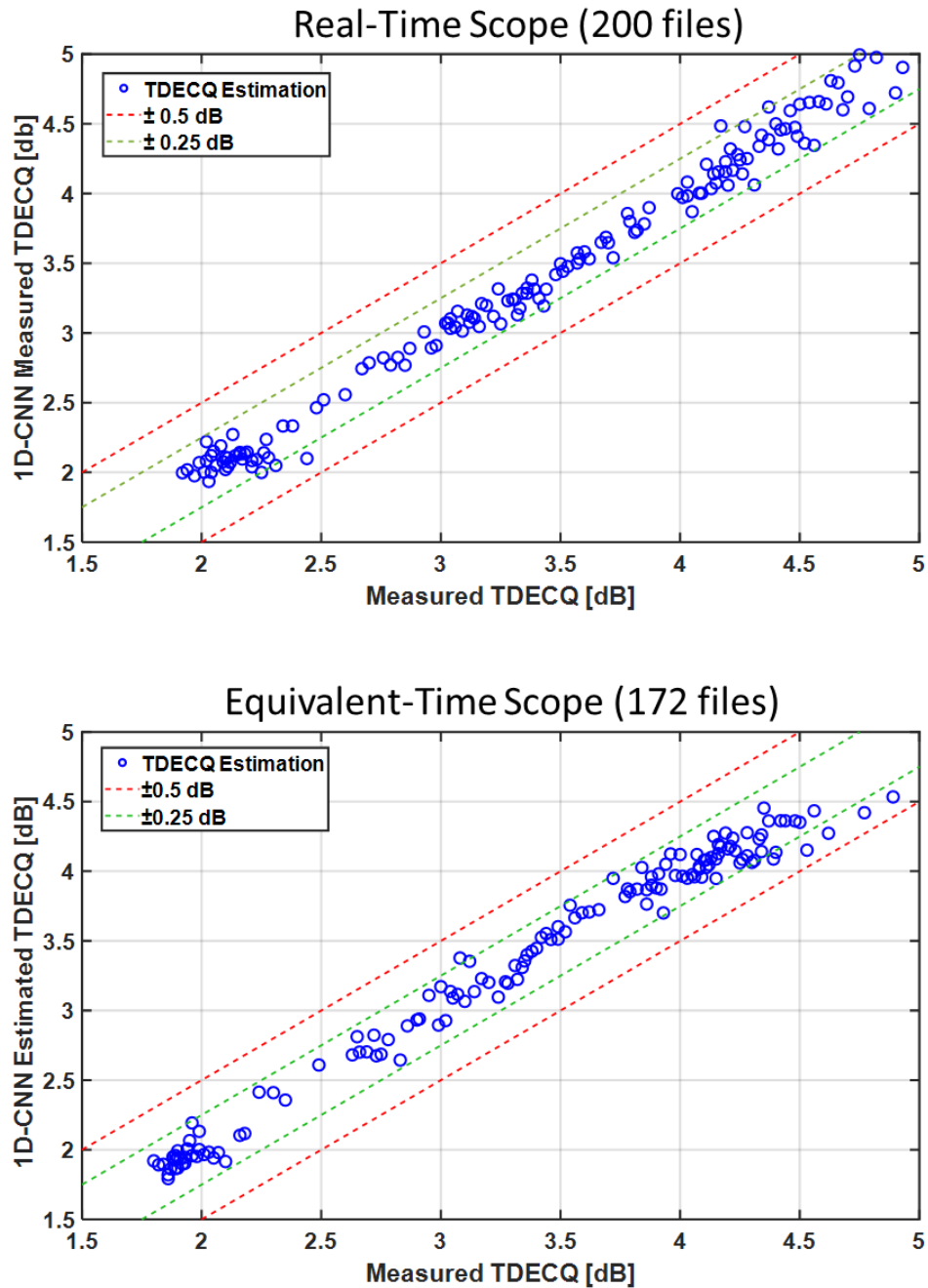


Figure 3.5: Performance comparison between real- and equivalent-time oscilloscopes for the signal-based TDECQ estimation demonstrating equivalent performance between the two oscilloscopes.

eye diagram. We note that there may be some impairments which result in similar effects on the eye diagram, and it may be difficult to separately identify these effects.

**Confusion Matrix**

<b>Output Class</b>	Bias Limited	Bias Limited	BW Limited	SNR Limited	Bias Limited
	Bias Limited	32 40.5%	0 0.0%	0 0.0%	100% 0.0%
	BW Limited	0 0.0%	18 22.8%	0 0.0%	100% 0.0%
	SNR Limited	0 0.0%	0 0.0%	29 36.7%	100% 0.0%
		100% 0.0%	100% 0.0%	100% 0.0%	100% 0.0%
		Bias Limited	BW Limited	SNR Limited	
		<b>Target Class</b>			

Figure 3.6: Confusion matrix depicting 100% impairment identification accuracy for the eye-diagram-based approach when TDECQ is greater than 3 dB. Bandwidth limitations, signal compression, and SNR limitations were all accurately identified. Note that 3 dB is the TDECQ threshold for compliance.

Nonetheless, identifying a single or few likely causes of poor transceiver performance will provide great benefits for validating components.

Next, we examine the impairment identification accuracy as the minimum TDECQ threshold is reduced to determine limits on impairment detection. Fig. 3.7 shows impairment identification accuracy versus the minimum TDECQ data used for training for the real-time oscilloscope and equivalent-time oscilloscopes, respectively. Impairment identification accuracy remained at 100% until the minimum TDECQ threshold was 2.6 dB. We note that a TDECQ of 2.6 dB reveals a well performing component. The reduced

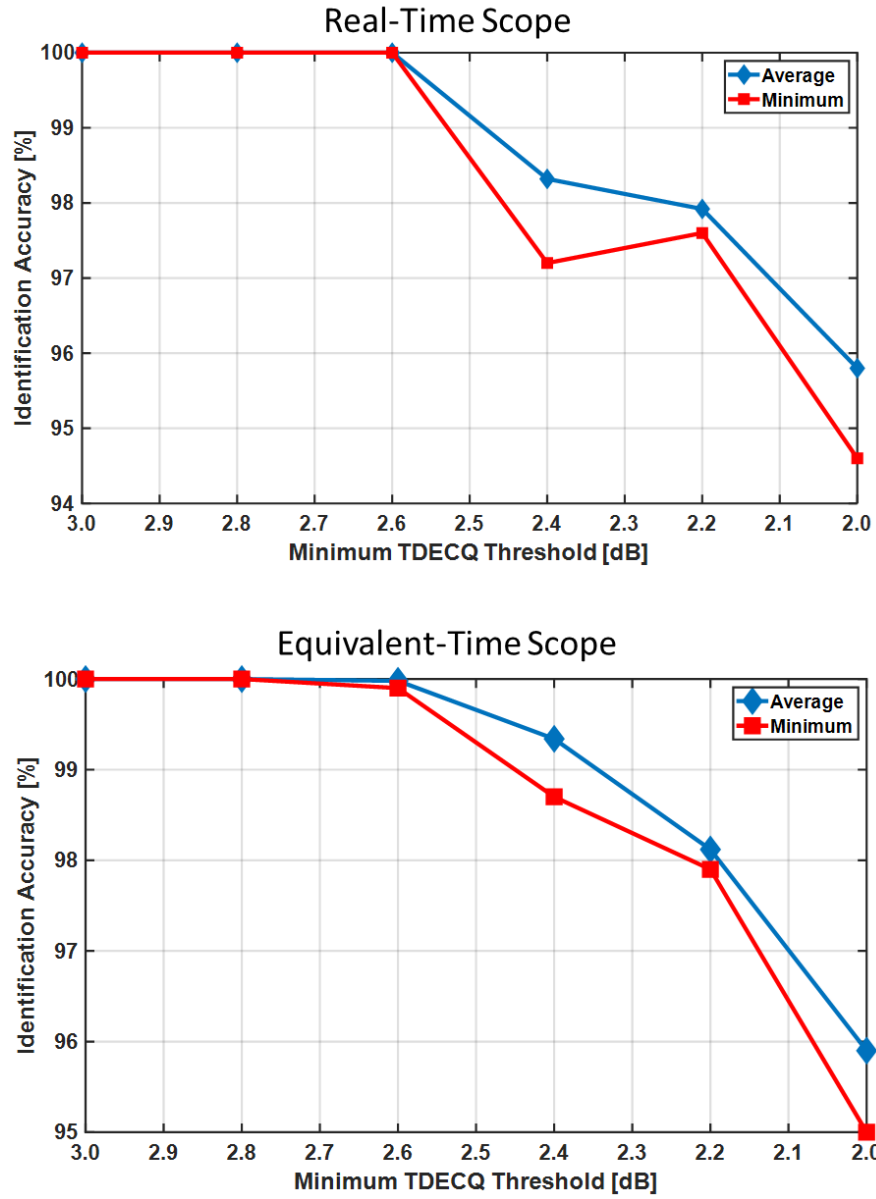


Figure 3.7: Impairment identification accuracy for real- and equivalent-time oscilloscopes when using the eye-diagram-based approach. All three emulated impairment types were jointly tested as a function of minimum TDECQ. The eye-diagram and waveform approaches demonstrated negligible performance differences, thus only one is shown.

accuracy clearly results from the near negligible impact of the impairment on the eye.

Hence, from a practical standpoint, properly trained ML algorithms can accurately identify impairments not only for all situations where the impairment was a significant

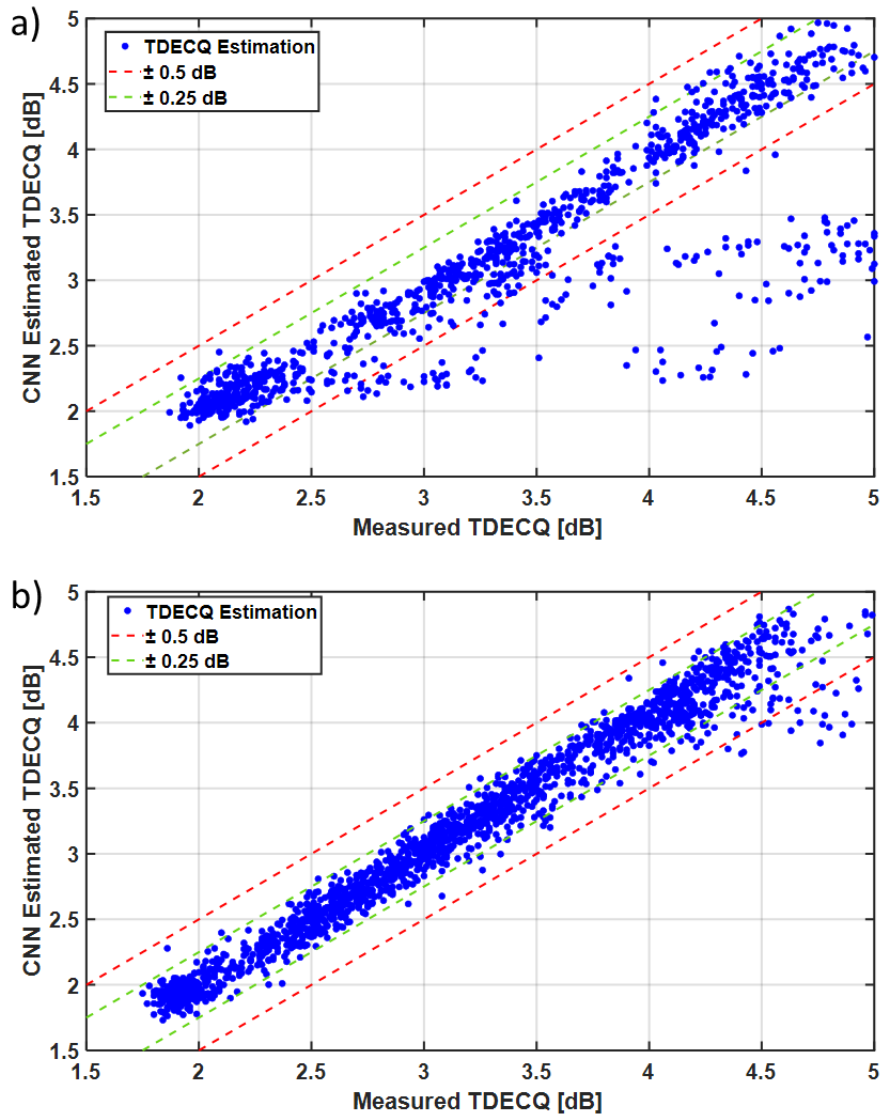


Figure 3.8: (a) TDECQ estimation results for CNN trained on one impairment and tested on multiple impairments. Demonstrates good accuracy for trained impairments while untrained impairments show little correlation between measured and estimated TDECQ. (b) TDECQ estimation results for CNN trained and tested on all impairments. Demonstrates good accuracy for all tested cases.

limiting factor, but also for cases where the effect is minimal – well within the IEEE compliance range of  $\leq 3$  dB TDECQ. It is noted that the analysis here consists solely of the 2D-CNN methodology for brevity; however, the 1D-CNN methodology demonstrates similar performance as it did during TDECQ estimation.

### **3.3 Impairment Dependence for ML Performance**

Here, we show the ramifications of different impairments on the TDECQ estimation accuracy. In one instance, we trained the CNN on a full range of TDECQ penalties only resulting from bandwidth limitations. The testing results over the same range of TDECQ but including other impairments is shown in Fig. 3.8(a). The ML algorithm accurately estimates the TDECQ for the impairment it is trained for; however, it fails to estimate the TDECQ for other impairments resulting in poor overall accuracy. Hence, CNN is impairment specific and not generalized for all types of impairments. This result is obvious as the eye diagram has varying effects depending on the impairment present which must be learned by the ML to be effectively managed. Therefore, it confirms that all anticipated impairments should be part of the ML training protocol – this is an important consideration when designing an effective ML solution to any problem. We verify this by training and testing with all generated impairments, Fig. 3.8(b). The TDECQ estimation accuracy was drastically improved in this scenario.

### **3.4 Oscilloscope Dependence for ML Performance**

The ML techniques are learning features from either the eye diagram or the waveform. These inputs, which are transmitted via a conventional PAM-4 transmitter, also incur some penalties or noise characteristics from the receiving technology. In fact, the different oscilloscope technologies have been shown to have different noise characteristics which may affect the signal quality in unique ways. As these oscilloscope-specific noise characteristics will be underlying all waveforms captured using that

oscilloscope, the ML will learn these noise characteristics directly so that they may be abstracted from the TDECQ estimation.

Figure 3.9 shows an example of cross testing the ML across real- and equivalent-time oscilloscopes using both the eye diagram and waveform methods – the ML was

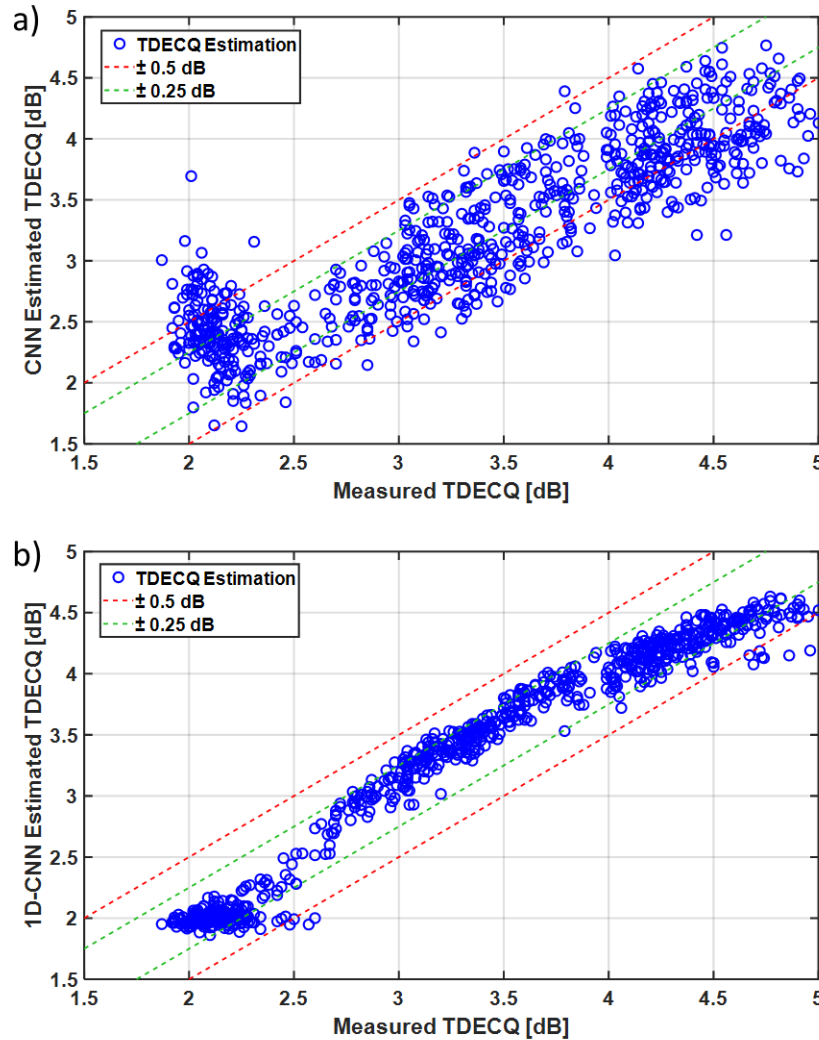


Figure 3.9: Demonstration of scope-specific noise characteristics for equivalent-time trained, real-time tested cases for the (a) eye-diagram method where quantization effects have a discernible effect on accuracy, (b) waveform method where quantization effects have minimal impact. Note that both cases have an inherent offset which corresponds to the inherent noise characteristics of the oscilloscope which the ML algorithm learns during training.

trained using equivalent-time oscilloscope waveforms and tested using real-time oscilloscope waveforms. The performance is greatly degraded for the eye diagram method. This is due to visible quantization effects which have a greater effect on the real-time oscilloscope eye diagrams which occur due to the lower bit resolution of the oscilloscope. Since the ML was trained on equivalent-time data, the ML has not learned these quantization effects thus it is likely interpreted as an impairment degrading the estimated performance.

However, for the waveform method, this is not true – estimation variance is relatively low demonstrating reasonable performance. Therefore, the quantization effects have had minimal impact in this case. Note that there is an inherent offset or bias which is clearly visible in this case due to the low estimation variance. This bias is the result of the underlying oscilloscope-specific noise characteristics. Thus, training should be performed on the specific scope for best performance. Training data requirements, however, can be reduced using certain ML approaches such as transfer learning.

#### *3.4.1 Transfer Learning for Oscilloscope-Specific TDECQ Estimation*

Sufficient performance of these ML methods is unique to training models for the specific devices due to learning the underlying characteristics such as the inherent noise profiles. This limits the possibility of developing a universal model as inherent biases based on these characteristics occur within the estimation. Therefore, one needs to train specific ML models for each device thereby limiting the deployment of this method as large amounts of data is required to train a well-performing model. However, by using an ML technique called transfer learning, we can leverage a previously trained network to

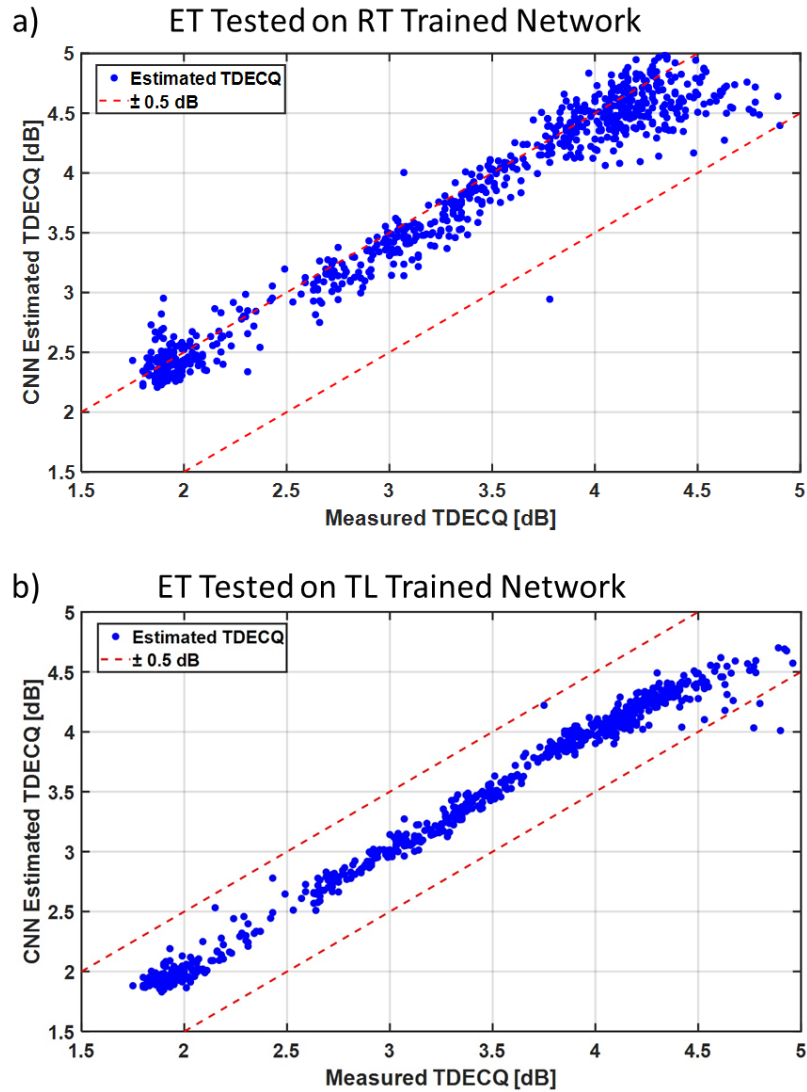


Figure 3.10: (a) Equivalent-time oscilloscope TDECQ estimation using real-time oscilloscope trained ML. Increased error based on the inherent noise characteristics of the real-time oscilloscope. (b) Equivalent-time oscilloscope TDECQ estimation using transfer-learning-based ML. Original CNN was initialized to a real-time oscilloscope dataset but retrained with a small subset of equivalent-time data.

initialize a newer, similar network – this enables the ML to generalize “knowledge” from the previously trained network to the new device, reduce the number of waveforms required for training, and can even accelerate the training process by having more efficient weight initializations.

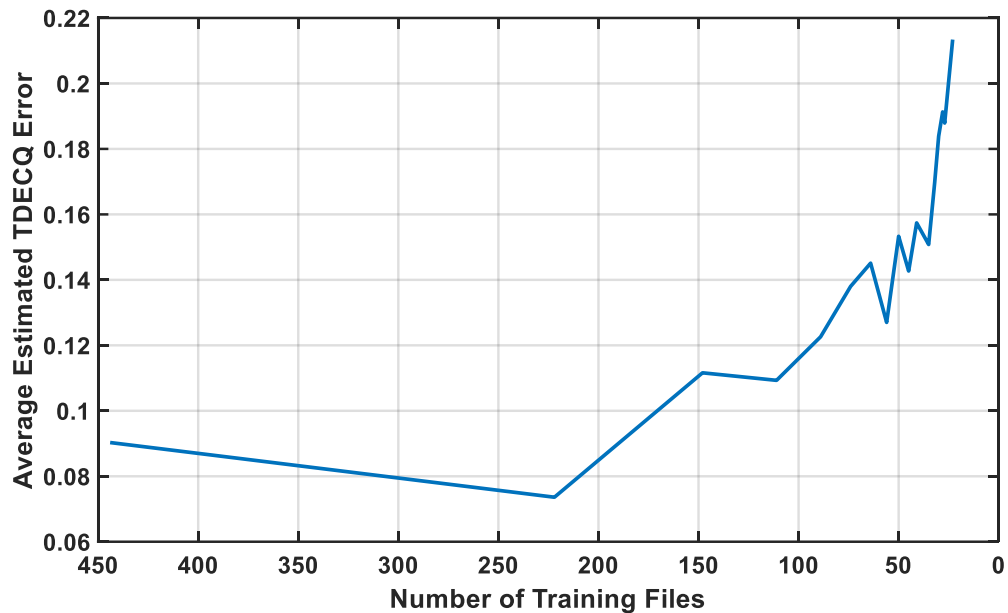


Figure 3.11: Transfer learning model accuracy scaled by number of files used to train the CNN. Model accuracy within 0.25 dB after using only 25 training waveforms. Model approaches expected accuracy metrics after only 100 waveforms and thus requires a dataset that is ~10% of the original network.

As shown previously, if you test equivalent-time data on an equivalent-time model, the estimation accuracy is high. However, if you test the same equivalent-time data on a real-time model, the estimation accuracy is poor and has an inherent bias to the estimation, Fig. 3.10(a). By implementing transfer learning, this real-time model can be rapidly adapted to manage equivalent-time data instead. Transfer learning is readily implemented by resetting specific layers (e.g., the fully connected layer) from a pretrained network, setting a low learning rate for the pretrained layers, and retrain this network using new, application specific data. Therefore, if we retrain the real-time model using a batch of equivalent-time data, the estimation performance of equivalent-time data on the retrained model is greatly improved, Fig. 3.10(b).

The number of waveforms required to retrain the model is now explored, Fig. 3.11. Transfer learning shows a stable estimation accuracy on the new model when  $\geq 200$  waveforms from the new device are used to retrain. After this, a penalty becomes apparent as the model has a harder time generalizing to the new data set due to the lack of statistical information about the new device. Nevertheless, 50% performance gain was observed compared to starting with an untrained network for the same number of training iterations. It is noted that this is an extreme case of transfer learning for this application – less waveforms may be required, and performance should improve if transfer learning is applied to different equivalent-time models as these models will have more similar noise characteristics.

### **3.5 Computational Complexity for TDECQ Estimation**

It is imperative to qualify PAM-4 transmitters during the manufacturing process by measuring the TDECQ per the IEEE 802.3 standard to ensure that these devices can provide sufficient performance. While it has been shown that ML can achieve sufficient accuracy when estimating the TDECQ for PAM-4 transmitters, the true advantage for using ML for this application is to increase the computational efficiency and therefore reduce calculation time. This enables greater manufacturing throughput by removing the bottleneck of the TDECQ qualification process.

Table 3.1 highlights the number of operations (multiplications, additions, and comparisons) required for the conventional, waveform (1D-CNN), and eye-diagram (2D-CNN) approaches as well as the runtime for each TDECQ calculation method. Some simplifying assumptions are done in this analysis which give benefit to the conventional

Table 3.1  
TDECQ Computational Complexity

Method	Multiplications	Additions	Comparisons	CPU Runtime
IEEE Algorithm	$1 \times 10^{10}$	$1.0 \times 10^{10}$	$1.0 \times 10^8$	55.0 sec
1D-CNN	$1.1 \times 10^9$	$1.1 \times 10^9$	$4.1 \times 10^7$	3.0 sec
2D-CNN	$2.5 \times 10^7$	$2.5 \times 10^7$	$3.1 \times 10^6$	0.1 sec

method. The computational complexity of associated DSP such as TR and upsampling is ignored. Likewise, the computational burden of Bessel filtering is ignored. ML methods for estimating TDECQ demonstrate up to 1000 times reduction on the number of computations compared to the conventional method which results in a decrease in computation time from 55 seconds to 0.11 seconds.

# **OPTICAL NETWORK MONITORING AND MANAGEMENT**

## **USING THE DIGITAL COHERENT RECEIVER**

Optical networks must demonstrate constant growth of their aggregate data rates to attempt to meet projected data demands. Coherent long-haul optical networks have exploited technologies such as WDM, time division multiplexing (TDM), PS, higher-order (or hybrid) modulation formats, etc. as methods to increase data throughput. When implementing these techniques, often in combination with one another, important link metrics such as the generalized optical signal-to-noise ratio (GOSNR) are often obscured or costly to monitor using traditional means. For example, the amplified spontaneous emission (ASE) level of a tightly spaced WDM system is difficult to assess by conventional spectrum analysis due to lack of a visible noise floor due to the adjacent side channels. Likewise, measuring the nonlinear noise by classical methods is difficult due to high computational burden as well as required system knowledge. A non-exhaustive list of literature for measuring the linear and nonlinear noise of optical systems are detailed in [123-129].

Optical links are composed of a multitude of optical components whose deterioration can result in catastrophic network failures if left unmanaged. While some network faults may be classified as hard failures and thus have specific and obvious causes, other faults may be classified as soft failures and slowly deteriorate the link performance (often within the allotted performance margin) which may eventually result in network disruption if left unchecked. Prior research has demonstrated attempts into detecting and identifying link failures [130-134].

Often, the components that make up these links are also not unique—that is, the network often includes multiple identical components such as EDFAs and ROADMs. Knowing that a failure is occurring as well as the type of failure is useful for troubleshooting; however, localizing that failure is even more valuable due to reduced troubleshooting efforts required to locate the appropriate repair in the optical links thereby drastically reducing downtime. However, interconnectivity between these optical links due to the use of ROADMs has created complicated mesh networks where failures within one link may also affect other links within that network. Thus, localization becomes a two-fold dilemma of network localization and link (point-to-point) localization. In [135-138], the network localization methods for various applications are detailed, and algorithmic approaches are presented.

The digital coherent receiver is the backbone of modern long-haul optical links. It allows for the reception and processing of coherent signals. Digital demodulation algorithms are commonly applied to signals acquired by the digital coherent receiver and are used to correct distortions and impairments that occur on signals during transmission. Thus, the algorithms often contain information about the link health which may then be correlated back to the total network health. Networking monitoring and management techniques may be employed by exploiting the digital coherent receiver to obtain information that is currently being ignored by network operators. By using the corresponding demodulation algorithms, the digital coherent receiver can be repurposed as a “test and measurement” equipment alongside its traditional purpose of signal acquisition thereby enabling the use of less monitoring equipment as well.

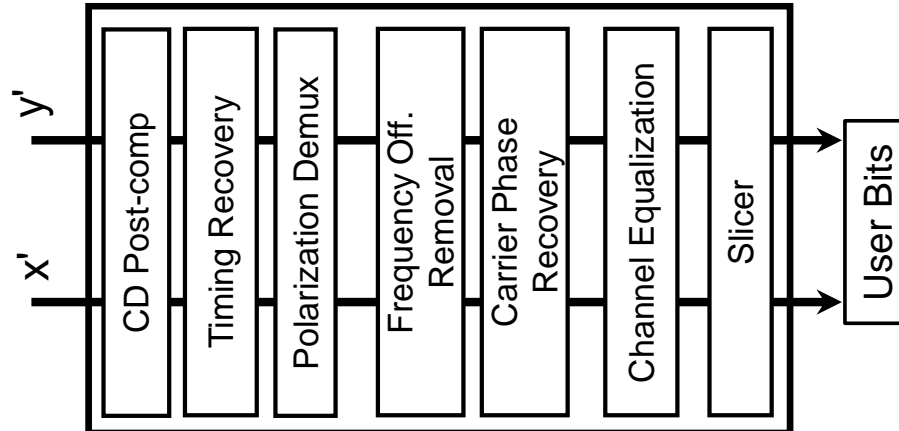


Figure 4.1: Conventional demodulation flowchart for a long-haul coherent optical link

In this section, we develop the framework for leveraging conventional, commercially implemented DSP such as the carrier phase recovery algorithm as well as common transmitter outputs such as the constellation diagrams to assist and enhance performance monitoring. Fault detection, identification, and localization are discussed. Machine learning is highlighted as a potential avenue to enhance next generation optical networks with examples of possible monitoring and modeling techniques.

#### 4.1 DSP Architectures with ML-Based Monitoring

Modern digital coherent receivers are often driven by DSP algorithms that assist with demodulation by correcting for distortions and impairments within the transmitted signal. For example, chromatic dispersion compensation is used to correct for temporal broadening that occurs due to the wavelength dependence of the group velocity. Equalization, as another example, is used to correct signal distortions such as intersymbol interference by spectrally flattening the signal. A conventional DSP chain is commonly structured as chromatic dispersion compensation, timing recovery, polarization

demultiplexing, frequency offset removal, carrier phase recovery, and channel equalization, Fig. 4.1.

Since the algorithms attempt to correct for impairments and distortions that occur from transmitting through fiber, the algorithm's corrections hold information that can identify not only the degree of impairment, but also the cause of the impairment. Thus, the digital coherent receiver can be used as a "test and measurement" equipment. However, interpreting the information from these algorithms is not necessarily obvious or straightforward.

Typical impairments and distortions in these links are usually statistically significant. However, since the signatures are often unique to the specific conditions of that link and the combination of compensation and degree of impairment is frequently nonlinear, traditional analytical methods are complicated to implement and are oftentimes computationally intensive. ML has been demonstrated as an innovative and extremely effective technique for developing these statistical models.

The design and development of ML techniques for DSP-based monitoring using extracted features from the digital coherent receiver is not straightforward. Multiple locations during demodulation may be chosen to monitor the same impairments. Thus, an information-theoretic tradeoff between feature pre-processing, data availability, and prediction performance exists. As the signal is processed during demodulation, information within the signal that corresponds to specific compensated impairments or distortions is reduced but impairment detection for effects that are not compensated may be enhanced. It may also be difficult to extract relevant features before certain processing

has occurred. For example, intersymbol interference (ISI) caused by chromatic dispersion distorts the signal such that before compensation, meaningful feature extraction is difficult due to the noise-like representation of the signal. Likewise, an important consideration is the availability of certain information during commercial deployment as data rate taps from certain DSP are very costly to design, develop, and manufacture.

## 4.2 Conventional Monitoring Parameters for Fiber Optic Networks

By utilizing the appropriate OPM equipment or techniques, one can monitor network parameters such as OSNR, nonlinearities, power, wavelength, etc. on a per-channel basis which can enable network planning and optimization. In this section, we focus on monitoring the linear and nonlinear noise with respect to the GOSNR which accounts for the joint linear and nonlinear contributions. The limitations of traditional measurement techniques within modern optical networks are discussed.

### 4.2.1 Linear Noise in Optical Networks

Optical systems consist of different types of noise and distortions – linear noise is one of the most important types as it directly relates to the OSNR of the network which largely defines the performance of the network. Linear noise in optical networks largely results from ASE which is generated during amplification. The largest source of ASE is usually from the EDFAs typically used in long-haul optical networks.

Traditionally, OSNR is defined as

$$OSNR_{dB} = 10 \cdot \log_{10}(P_{signal}/P_{linear}) \quad (4.1)$$

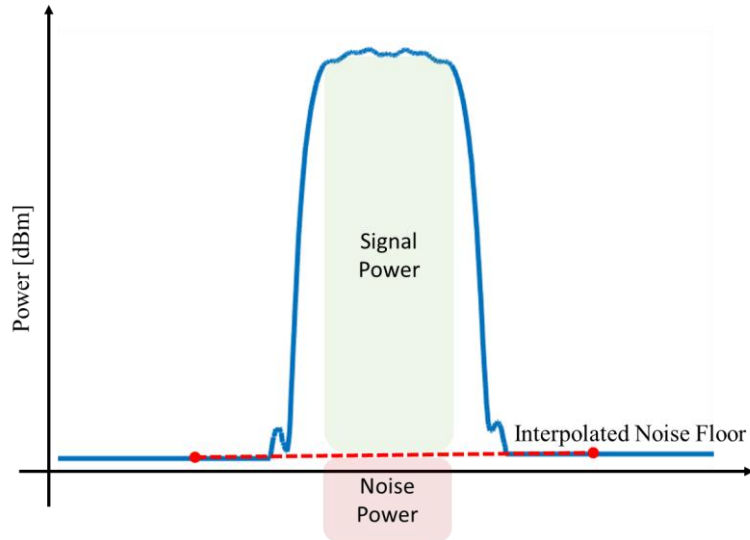


Figure 4.2: OSNR measurement using an OSA. Noise floor is estimated via the out-of-band noise. Conventionally, signal and noise power are integrated within a 0.1 nm band. Other integration

where  $P_{\text{signal}}$  is the optical power of the signal and  $P_{\text{noise}}$  is the optical power of the linear noise. Conventionally, the OSNR may have been measured using an optical spectrum analyzer by extrapolating the noise floor from the out-of-band optical noise spectrum, integrating the amount of noise power, integrating the signal power, and calculating the ratio of signal power to noise power, Fig. 4.2.

However, when utilizing WDM, the noise floor may become obscured by adjacent channels. Thus, it becomes impossible to calculate the noise floor. Likewise, filtering effects from ROADMs also affect the noise floor estimation resulting in inaccurate OSNR measurements at the receiver.

#### 4.2.2 Nonlinear Noise in Optical Networks

When monitoring optical networks using WDM, the capacity is oftentimes limited by the optical Kerr effect which results in nonlinear effects such as self-phase modulation, cross-

phase modulation, four wave mixing, and cross polarization modulation. The quality of transmission (QoT) is decreased due to intra- and inter-channel signal-signal interactions as well as signal-noise interactions [139]. The complete compensation of these nonlinear effects is difficult because it would require complete knowledge of the propagation of all channels as well as ASE noise additions.

Classical theoretical methods for modelling the nonlinear effects within optical fibers are largely based around the nonlinear Schrodinger's equation (NLSE)

$$\frac{dA}{dz} = -\frac{\alpha}{2}A - i\frac{\beta_2}{2}\frac{d^2A}{dt^2} + i\gamma|A|^2A \quad (4.2)$$

where  $A(z,t)$  is the light pulse envelope,  $\alpha$  is the fiber attenuation,  $\beta_2$  is the second-order chromatic dispersion, and  $\gamma$  is the nonlinear coefficient. Since the NLSE is a nonlinear partial differential equation, finding analytical solutions can prove challenging and computationally expensive. Numerical methods such as the popular SSFM are often used to find approximate solutions to the equation. In fact, digital backpropagation is the most common method for nonlinear compensation in optical networks – this technique uses the SSFM to reverse fiber propagation and estimate the transmitted signal from the received signal [140].

#### 4.2.3 Generalized OSNR in Optical Networks

The GOSNR is a link metric that measures the aggregate performance of an optical link based on both the linear and nonlinear noise contributions and is defined as

$$GOSNR_{dB} = 10 \cdot \log_{10}\left(\frac{P_{signal}}{P_{noise,lin} + P_{noise,NL}}\right) \quad (4.3)$$

The GOSNR is essentially the true, in-band OSNR since it additionally accounts for the nonlinear noise which is an in-band source of interference. In practice, measuring the GOSNR requires the assumption that the dominating signal degradations result strictly from these linear and nonlinear effects. Therefore, any other signal distortions such as those that may arise from nonoptimal DSP are ignored. Note that this is an important distinction for ML-based approaches.

### 4.3 Optical Performance Monitoring via Carrier Phase Recovery

In this section, we develop and experimentally verify an ML framework for leveraging a commercially implemented carrier phase recovery algorithm to assist in automated performance monitoring of an optical link.

#### 4.3.1 Methodology

The CPR algorithm compensates for phase differences between the transmitted carrier and the receiver's local oscillator which results in accumulated phase noise within the signal, Fig. 4.3(a). Phase errors that result from the difference between the transmitter and LO are modelled as a Wiener process [141, 142]. A Wiener process is defined as a sum of independent and identically distributed Gaussian random variables. Thus, the source and LO generate a random phase walk

$$\varphi(t+1) = \sum_{k=0}^{t+1} \theta(k) \quad (4.4)$$

$$\varphi(t+1) = \varphi(t) + \theta(t+1) \quad (4.5)$$

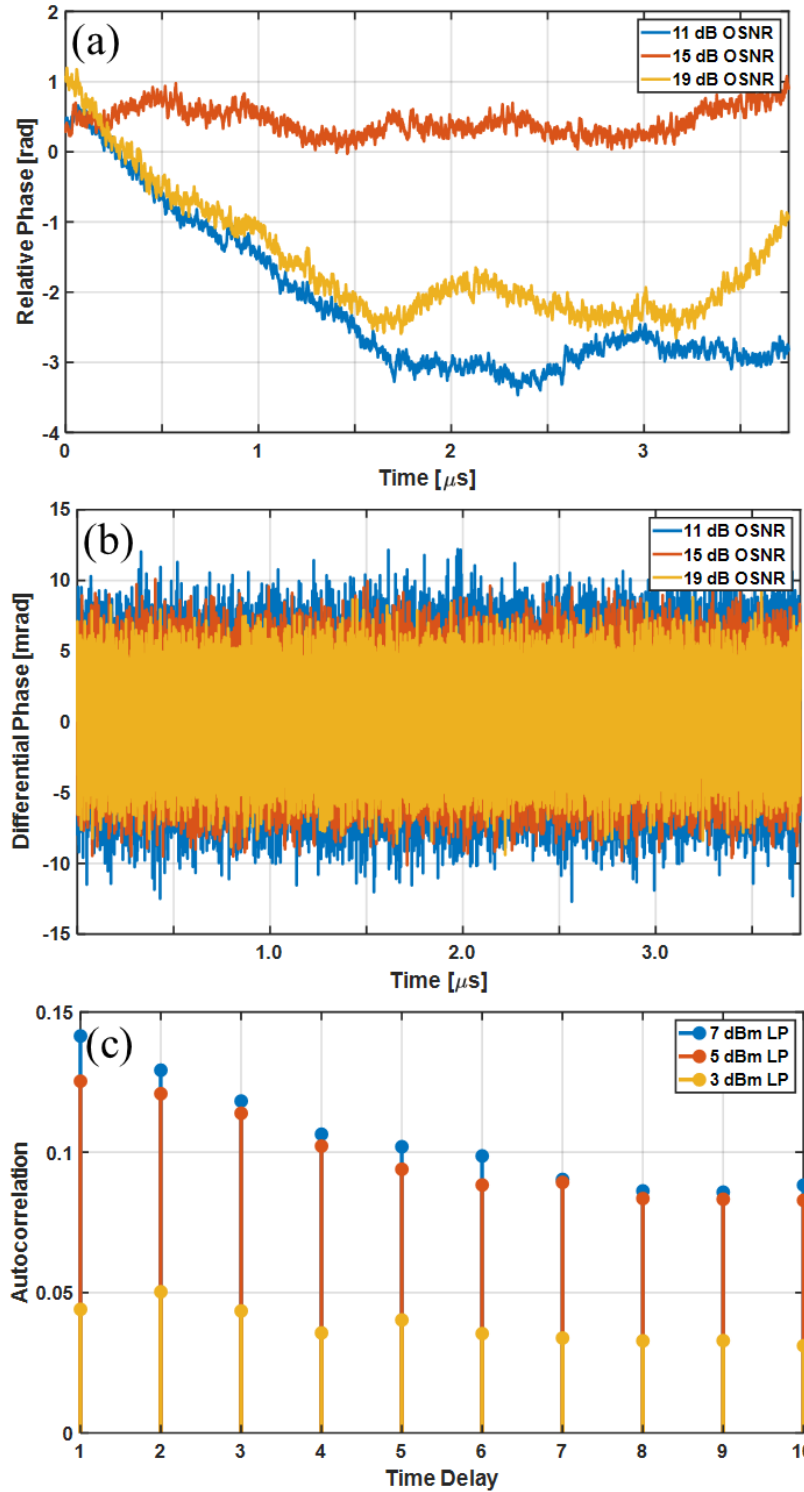


Figure 4.3: Demonstration of (a) the carrier phase estimate from a conventional CPR algorithm for OSNR of 11, 15, and 19 dB, (b) the resulting differential phase from each of the carrier phase estimates to be used as the feature of interest, (c) the autocorrelation of three differential phases with varying launch powers.

where  $\varphi(t)$  is the accumulated phase noise and  $\theta$  represents the random walk that results from a 0 mean Gaussian random variable.

Since each moment in time is theoretically independent from subsequent timings, we can extract an approximation of this random phase walk, Fig. 4.3(b), by simply taking the differential of the CPR estimate for two subsequently measured timings

$$\theta(t + 1) = \varphi(t + 1) - \varphi(t) \quad (4.6)$$

$$\theta(t + 1) = \sum_{k=0}^{t+1} \theta(k) - \sum_{j=0}^t \theta(j) \quad (4.7)$$

The CPR algorithm cannot discern optical noise that accumulated during transmission from the phase noise that accumulates from mismatched and fluctuating phase between the transmitter and LO. Thus, it attempts to account for all sources of phase noise. This enables us to develop and demonstrate an algorithmic approach to correlate the phase noise metrics from the CPR algorithm to total system noise and even correlate to specific noise types.

The two main sources of noise that are considered are linear and nonlinear noise: ASE noise sources present as a white Gaussian phase noise while nonlinear noise presents itself as a colored phase noise. In the absence of nonlinearities, the rms value of the random phase walk becomes a good proxy for measuring the linear noise of the system – this is possible since the phase noise contributions that result from the ASE are greater than the contributions that result from transmitter-induced phase noise.

Nonlinear noise results in similar variations within the phase noise estimation as ASE noise. Therefore, to differentiate between the two, it is imperative to exploit the colored nature of the noise by measuring the correlation, Fig. 4.3(c). It is noted that the transmitter-induced phase noise is also colored which creates an issue with differentiating between the two sources. However, since the transmitter-LO phase noise is modeled as a Wiener process, taking the differential does enable the phase noise to be decolored by reducing the signal from the random walk into its base components of iid zero mean Gaussian random variables.

#### 4.3.2 *Experimental Setup*

The method was experimentally validated by collecting waveforms using a 32 Gbaud DP-QPSK link with three channels spaced at 37.5 GHz around 1550 nm, Fig. 4.4(a). An ITLA 1550 nm laser source with <25 kHz linewidth was used. The data was demodulated offline using conventional receiver-side DSP [143]. The presence of side channels is essential to capture realistic nonlinear effects found within a typical link configuration. No fiber nonlinearity compensation was performed during demodulation.

The OSNR, which was used as one of the training targets, was measured using a conventional OSA approach where measured out-of-band optical noise was used to estimate the in-band optical noise. Note, adjacent channels were shifted during OSNR measurement to allow for noise floor interpolation while preserving the total power. The measurement was performed before the WSS to preserve the out-of-band noise floor which is used to estimate the in-band noise. OSNR was varied from 11 dB to 19 dB via ASE noise loading. The nonlinear noise (using launch power as the proxy and training

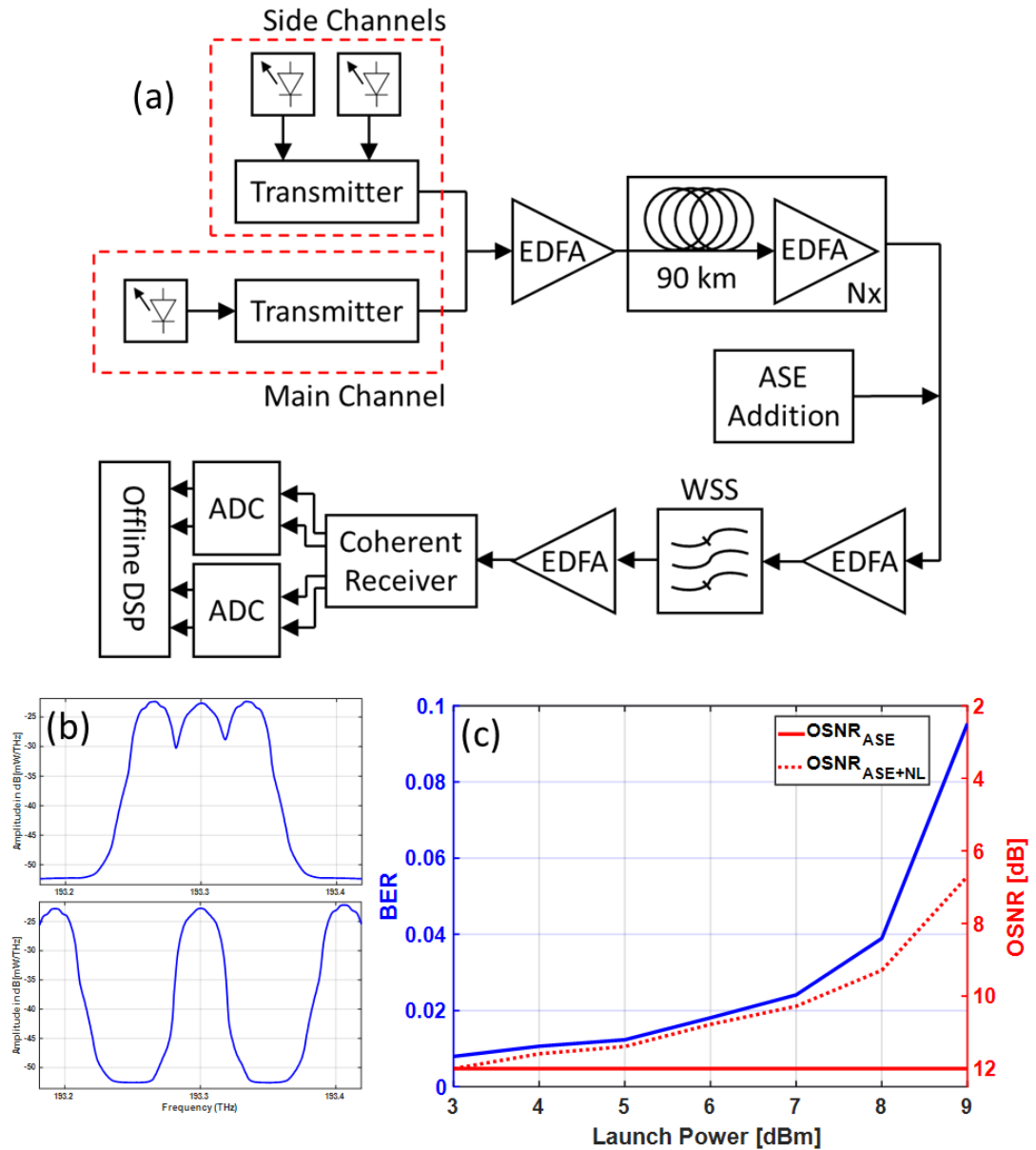


Figure 4.4: (a) Experimental setup used for verifying the proposed technique. The setup employed a 3-channel 32 Gbaud DP-QPSK signal over 270 km of SSMF. OSNR was varied via ASE noise loading, (b) example of channel spacing used for OSNR measurement, (c) demonstration of nonlinear penalties associated with increasing launch power for 12 dB OSNR.

target) was set via the EDFA before the first span and was varied from 3 dBm to 9 dBm.

A total of 63 cases were generated by spanning each combination of OSNR and launch power. Each case consisted of 150 waveforms. Note that with proper target labels and training paradigm, the launch powers can be directly mapped to the actual nonlinear penalty, Fig. 4.4(c).

### 4.3.3 Machine Learning Architecture Overview

A simple feedforward neural network is trained for regression using both the variance and correlation data from the differential of the CPR estimate, Fig. 4.5. The outputs are trained for both linear OSNR and launch power. The neural network has one hidden layer with 11 neurons – an extremely simple architecture. Thus, although, it may be possible to directly identify noise contributions from the differential of the CPR estimate, the simplicity of the algorithm alongside the potentially complex relationship between linear and nonlinear contributions readily lends itself to this ML approach.

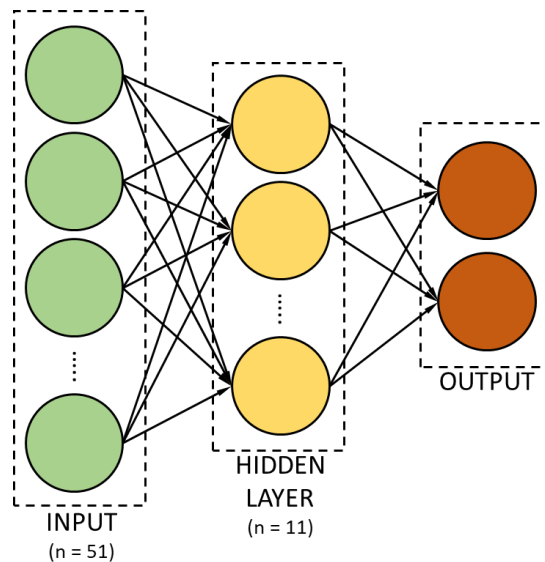


Figure 4.5: Simple FFNN with one hidden layer used to jointly estimate the linear and nonlinear noise. The input features are the first 50 coefficients of the autocorrelation from the differential phase noise as well as the RMS value of this phase noise metric.

Similarly, while it may be possible to directly use the differential of the CPR estimate as an input to a ML tool, this approach would drastically increase the complexity of the algorithm and may be prone to overfitting while providing little to no benefit to the accuracy of the method.

#### 4.3.4 Results

Figure 4.6 demonstrates the minimum, mean, and maximum error for the technique for various cases. Figure 4.6 (a)-(c) demonstrates the OSNR estimation accuracy for 11 dB to 19 dB for the following launch powers: 3, 6, and 9 dBm. The OSNR estimation was relatively consistent across all tested OSNR regardless of the launch power except for a slight increase in maximum error for higher OSNR which is due to approaching the noise floor of the phase noise. This noise floor occurs due to noise sources outside of the ASE noise which largely results from the optical amplifiers. These other noise sources include phenomenon such as thermal noise limits, transmitter impairments, and electrical noises which may result from components such as the AWG or oscilloscope. It is noted that extremely high OSNR is difficult to measure using a conventional approach due to this same effect therefore it is not an exclusive limitation of this method.

Figure 4.6 (d)-(f) demonstrates launch power estimation accuracy for 3 to 9 dBm for the following OSNR: 11, 15, and 19 dB. Launch power estimation demonstrates very low mean error for all cases,  $<0.1$  dB. Low maximum error of  $<0.5$  dB is demonstrated for nearly all cases. Thus, the technique has high accuracy for launch power estimation across all tested OSNR. All cases were tested; however, specific cases are demonstrated for brevity. The chosen cases evenly span the entire data set. Nonlinear estimation can be

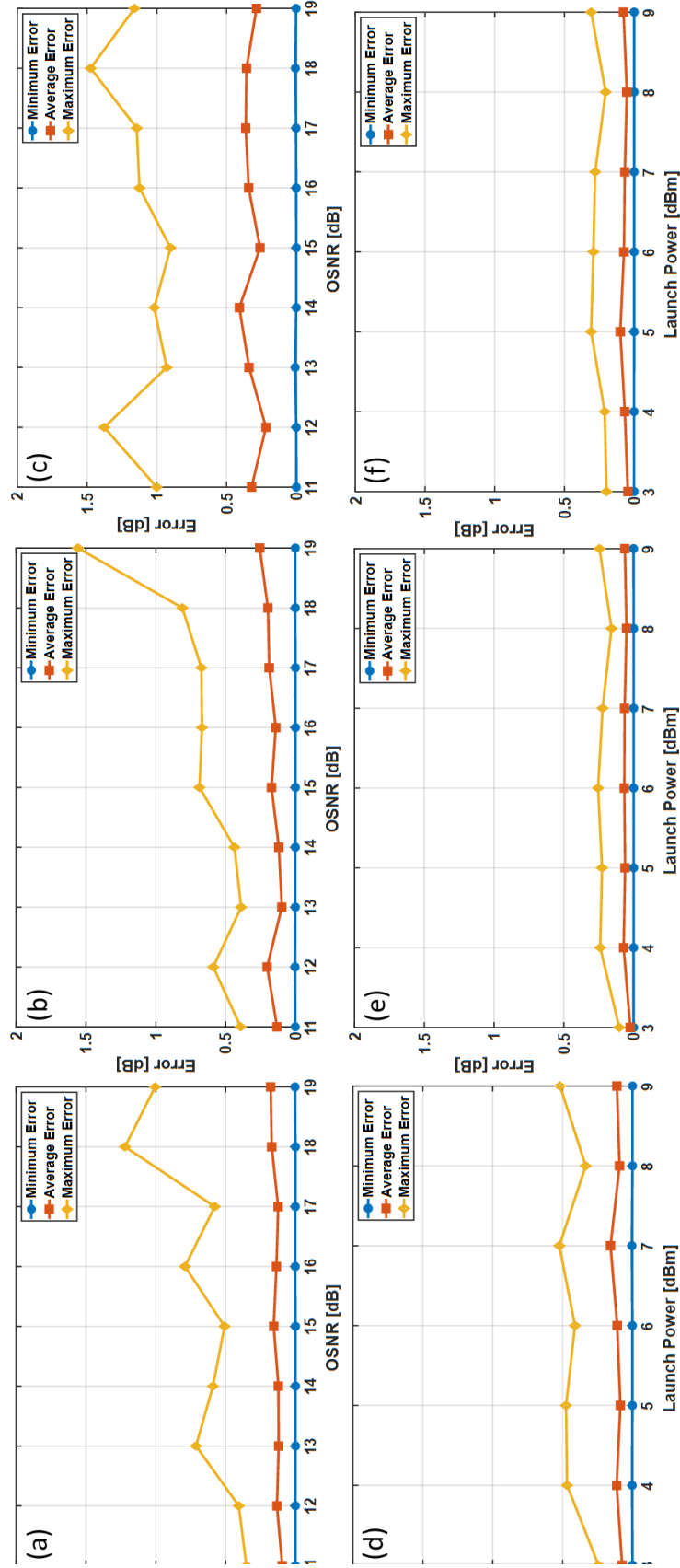


Figure 4.6: Minimum, average, and maximum error results for the proposed technique. Various test cases are shown: OSNR estimation error for launch power (a) 3 dBm, (b) 6 dBm, and (c) 9 dBm. Launch power estimation error for OSNR (d) 11 dB, (e) 15 dB, and (f) 19 dB.

performed primarily using the correlations found in the phase noise while OSNR estimation requires information from both the correlation as well as the absolute rms value of the phase noise. This is due to the added nonlinear phase noise that results from nonlinear contributions increasing the rms value.

#### **4.4 Optical Performance Monitoring via Constellation Diagrams**

In this section, we develop and experimentally verify another ML framework that leverages the constellation diagram to automate the measurement of the OSNR, GOSNR, and BER of an optical network. The constellation diagram is a readily accessible feature in modern optical networks which bypasses some disadvantages of the previously demonstrated method. Methods requiring real-time data need high speed channels which are limited due to the prohibitive cost of developing a compatible ASIC. Likewise, memory is often limited which drastically decreases the number of sampling points that can be used in the analysis. Furthermore, a large amount of data is required to train the ML which requires either significant effort before deployment or downtime afterwards. Therefore, we focus on a practical implementation where constellations are generated via a small number of constellation points and limited data is used for training the ML architecture.

##### *4.4.1 Experimental Setup*

Figure 4.7(a) depicts the optical testbed where two test channels from a commercial transceiver are configured to either 69.44-GBd polarization-division multiplexed (PDM) QPSK or 16-QAM modulation at a channel spacing of 100 GHz to avoid filter and crosstalk effects. The remainder of the 4.8-THz optical WDM bandwidth was filled with

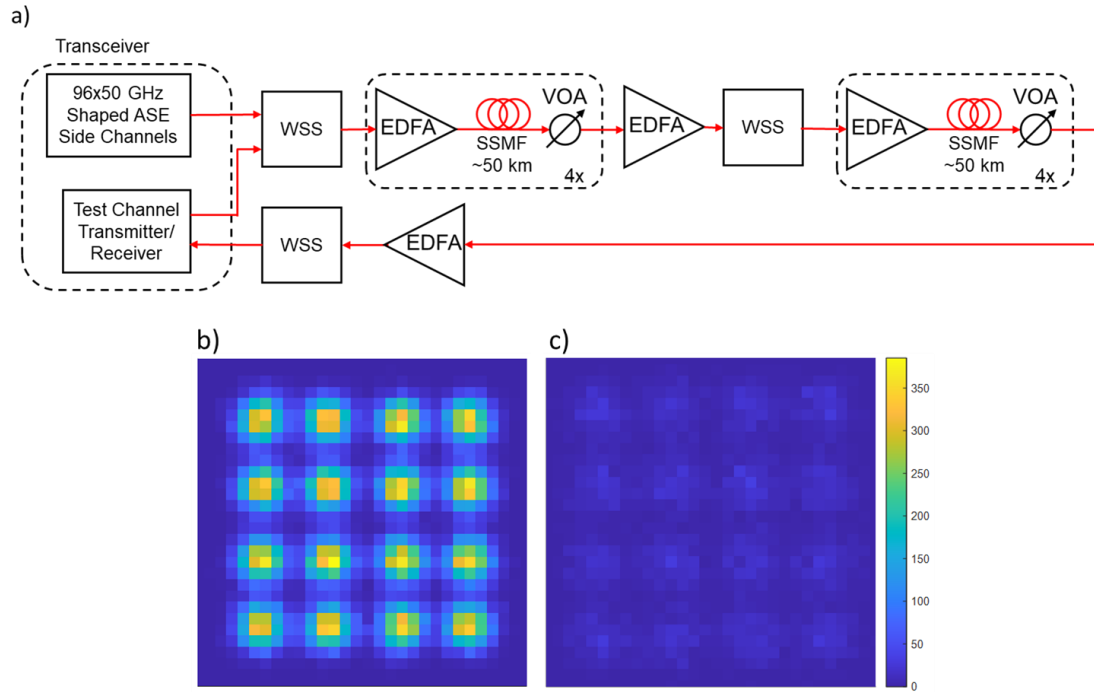


Figure 4.7: (a) Experimental setup which consists of 8 spans used to collect data for training and testing the CNN to estimate OSNR, GOSNR, and BER. (b) Example constellation density with 60,000 symbols demonstrating common laboratory test conditions, (c) example commercial constellation density with 6,144 symbols scaled to the 60,000-symbol constellation.

spectrally shaped ASE noise [144, 145] on a 50-GHz channel grid. A WSS is used to combine the channels and equalize the power per channel. The channels are transmitted through a link composed of eight 50-km spans of standard SSMF and EDFAs.

A WSS is used after 4 spans for equalization to minimize wavelength dependent variations in channel power. A variable optical attenuator (VOA) is present after each span to control the span loss which allows for nonlinearity to be varied independent of OSNR. The collected data includes 15 dB and 21 dB span losses, and four different launch powers spanning an 8-9 dB range across the linear and nonlinear regimes. An optical spectrum analyzer is used to monitor link conditions at various locations such as

OSNR (using signal on/off method), channel power, ripple, tilt, etc. GOSNR was measured from the corresponding back-to-back OSNR needed to achieve the same BER. After the 8-span link, a WSS was used to demultiplex the modulated test channels before the receiver. Data, in the form of constellation diagrams, was collected over eight link configurations with various amounts of ASE and nonlinear noise.

In a laboratory setting, data may be collected and processed with real-time symbols using tens of thousands of data samples [146]. In this work, constellation diagrams were generated from sparse constellations which were composed of 6,144 symbols per data acquisition. This drastically affects the constellation density which is one of the most essential features of the constellation, Fig. 4.7(b)-(c). Constellation density is used to measure the spread of the constellation points as well as the spreading symmetry. ASE and nonlinear noise contributions induce symmetric constellation spreading while nonlinear noise contributions alone cause asymmetric spreading.

#### *4.4.2 Machine Learning Architecture Overview*

Convolutional neural network approaches have been popularized as an extremely effective method for automated image processing and classification. Figure 4.8 depicts the CNN architecture that was used to estimate a variety of parameters such as the BER, OSNR, and GOSNR from the constellation diagrams. The architecture consists of three FELs each composed of a convolutional layer with a nonlinear function (leaky rectified linear unit) as well as an average pooling layer. The final FEL implements a global average pooling layer. The final FEL connects to a series of three FCLs which performs the regression between the extracted features and the target output (BER, OSNR, and

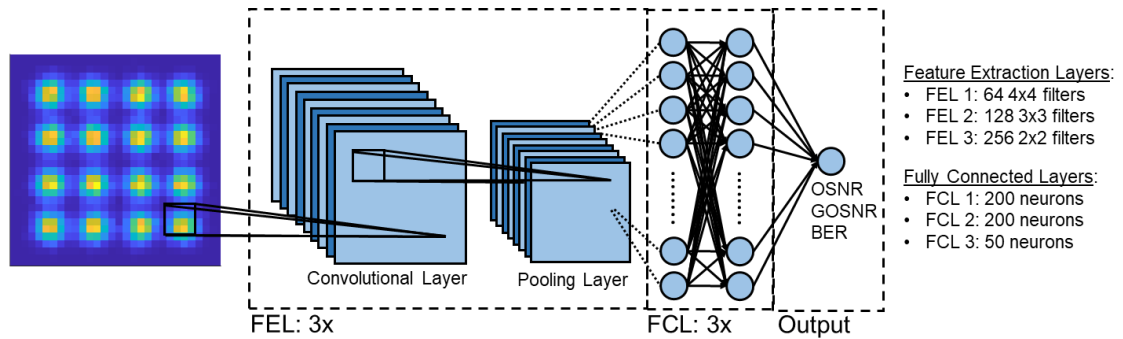


Figure 4.8: CNN architecture consisting of three FEL and three FCL. There is an implied leaky rectified linear unit between convolution and pooling layers to generate a nonlinear mapping. The input image is a constellation density plot. The same architecture was used for OSNR, GOSNR, and BER estimation.

GOSNR). The FCLs consist of 200 neurons for the first two layers and 50 neurons for the last layer. The data was divided 60/20/20% for training/testing/validation with a total of 6,400 constellations spanning eight configurations.

#### 4.4.3 Results

The eight link configurations were chosen as a minimalist data set that spans a variety of linear and nonlinear noise conditions – this tests the limit of data necessary to accurately assess link performance. OSNR, GOSNR, and BER were chosen as the performance parameters of interest. Figure 4.9(a)-(c) shows the results from training a CNN with constellation diagrams as the input and the performance parameters as output. These outputs were trained using independent CNNs. The ML algorithm accurately estimates the BER with a mean absolute percentage error of 6.3% and a maximum absolute percentage error of 18.4%. The GOSNR estimation had a mean absolute error of 0.16 dB and a maximum absolute error of 0.46 dB. This implies that despite the lower number of configurations, the CNN can still accurately identify the total signal noise. The GOSNR

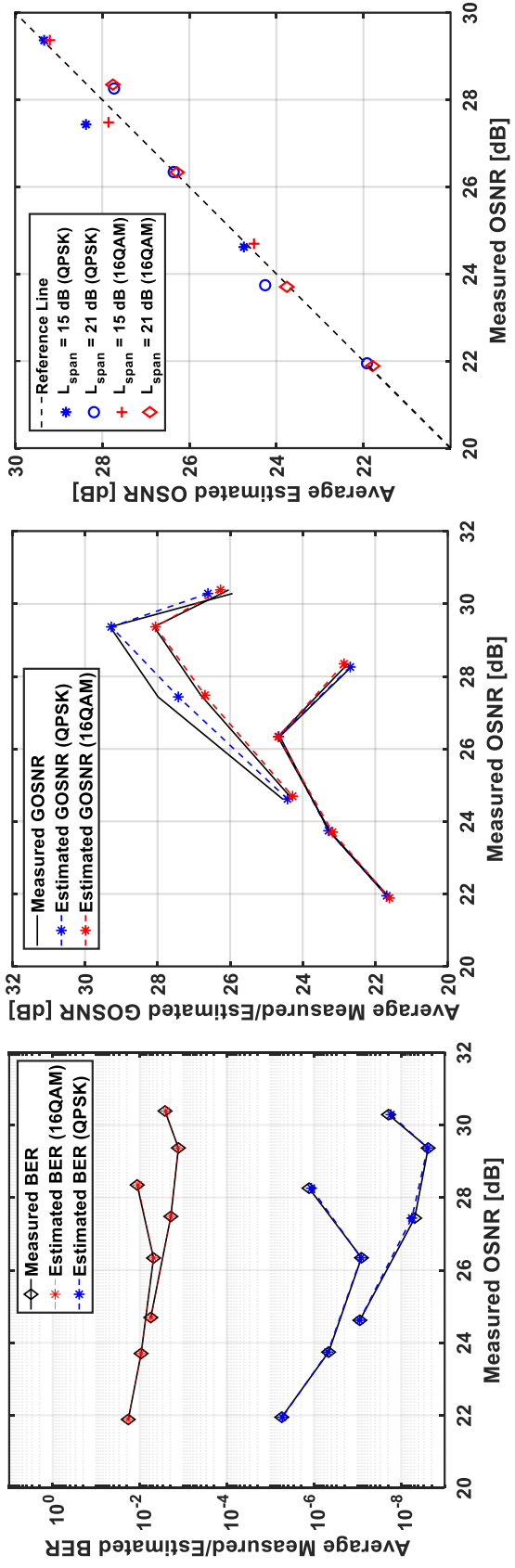


Figure 4.9: CNN estimation accuracy for both QPSK and 16-QAM modulation formats when trained on eight configurations which span a variety of linear noise and nonlinear noise conditions. (a) BER estimation accuracy, (b) GOSNR estimation accuracy, (c) OSNR estimation accuracy.

and BER are tightly correlated to the total spreading of the constellation which is apparent in the constellation density. It is expected that with more symbols, this estimation accuracy will be further improved due to increased statistical certainty.

The average OSNR estimation results are shown in Fig. 4.9(c). The estimations are compared to an ideal mapping between estimated and measured OSNR. The average estimated OSNR performs relatively well with some minor errors. It is noted that OSNR estimation is much more difficult than GOSNR and BER estimation as the OSNR estimation must separately identify the linear (ASE) contributions of the noise from the total signal noise (i.e., extract the linear noise from a combination of linear and nonlinear noise). This is exacerbated by the limited amount of training cases to learn this relationship. Nonetheless, the mean absolute error of the OSNR estimation was 0.57 dB with a maximum absolute error of 1.61 dB. The lower number of symbols in these test cases limits the statistics which are likely crucial to differentiate the linear and nonlinear noise as well as the fact that constellation density plots do not include temporal information which further obfuscates the issue. Increasing the number of symbols will reduce both the mean absolute error, and more importantly, the maximum error.

#### **4.5 Impairment Detection and Identification for Fiber Optic Networks**

While optical performance monitoring allows some prediction of the QoT, it does not allow for network operators to monitor the total network health. Network disruptions are often due to link impairments that degrade the signal quality. Certain disruptions may occur due to “hard failures” which result in instant and catastrophic network failures – these failures typically have specific and obvious causes such as fiber damage. Other

disruptions may result from “soft failures” which may gradually degrade the link performance. These degradations may occur within allocated margins and thus may not trigger alarms until the network is disrupted. Similarly, the demodulation algorithms may correct for acute disruptions in the network until the network performance degrades beyond the ability to compensate resulting in instant and catastrophic link failure.

One consequence of these effects being “hidden” is that the monitoring of such impairments may be difficult or nonintuitive without additional monitoring equipment or adapted monitoring strategies to account for these effects. This has spurred an entire branch of research dedicated to solving this dilemma. Many proposed approaches have advocated for the use of ML for impairment identification due to its ability to automate the modelling process. However, while ML-based monitoring techniques work well within their design space, the limits outside of this region is often not explored. Specifically, it is often not quantified how unexpected impairments, which sometimes may be similar in effect but different in origin, affect the technique. This also applies to performance monitoring techniques. In this section, we demonstrate an identification scheme for saturated, nonlinear electrical amplifiers in the presence of fiber nonlinearities using constellation-based ML to demonstrate the efficacy of ML, but also warn of blind over-reliance.

#### *4.5.1 Experimental Setup and ML Architecture*

Figure 4.4 depicts the experimental setup which was used to collect waveforms with varying amounts of fiber nonlinearities. Fiber nonlinearities were generated by varying the launch power into the first span with each subsequent span compensating for the fiber

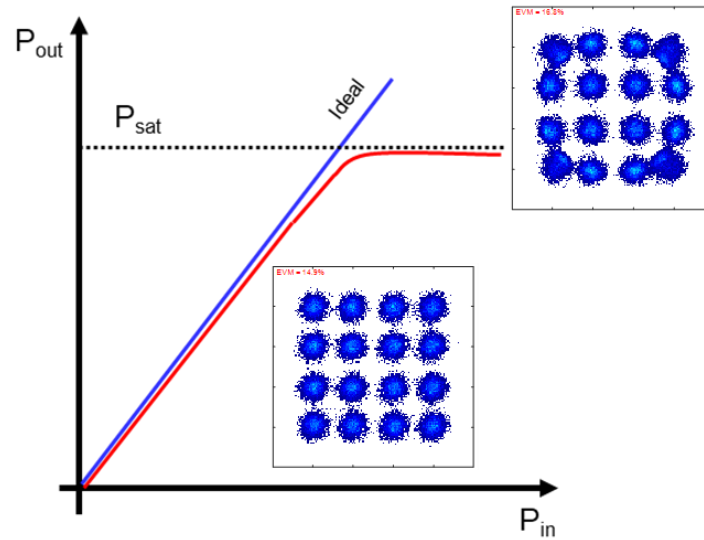


Figure 4.10: Waveform clipping to emulate saturated amplifier nonlinearities. Waveforms were clipped on both in-phase and quadrature components. Clipping amount was varied as a percentage of the max.

loss. Raw waveforms were collected and processed using offline DSP to generate the required constellation diagrams. Saturated amplifier nonlinearities were emulated onto the digital waveform during demodulation by using a soft roll-off clipping function on the waveform, Fig. 4.10. Clipping was measured and varied as a percentage of the maximum constellation value. Figure 4.11 differentiates between a fiber nonlinearity and amplifier nonlinearity constellation when each constellation has identical statistics: error vector magnitude (EVM) of  $\sim 18.2\%$  and BER of  $\sim 7 \times 10^{-3}$ . It is visually apparent that there are minor statistical differences between the fiber and amplifier nonlinearities – one major distinction is the presence of nonlinear phase noise which results from fiber nonlinearities while amplifier nonlinearities were simulated with a well-defined clipping function which depends only on the amplitude.

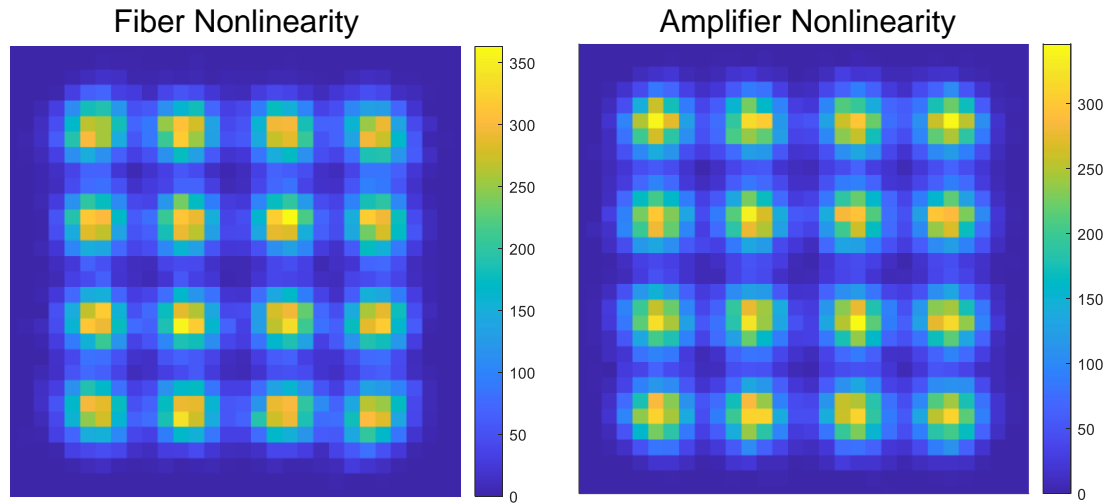


Figure 4.11: Constellation density plots for fiber and amplifier nonlinearities. Both constellations exhibit EVM of  $\sim 18.2\%$  and BER of  $\sim 7 \times 10^{-3}$ . Visually apparent statistical density differences on a per-cluster basis are observed.

The CNN depicted in Fig. 4.8 was used to perform the impairment identification with minimal modifications. This CNN was already designed and thus well-suited for constellation analysis. Algorithm outputs included both impairment identification and clipping estimation.

#### 4.5.2 Results

Figure 4.12 shows the confusion matrix for identifying amplifier and fiber nonlinearities with the previously mentioned waveform statistics resulting in an identification accuracy of 100%. This implies that there are distinct differences (in this simulated vs. reality case) which are sufficiently modelled using ML. Note that this analysis is such that the clipping is discernible and applied to a waveform with no fiber nonlinearity to allow for fair comparison between the two.

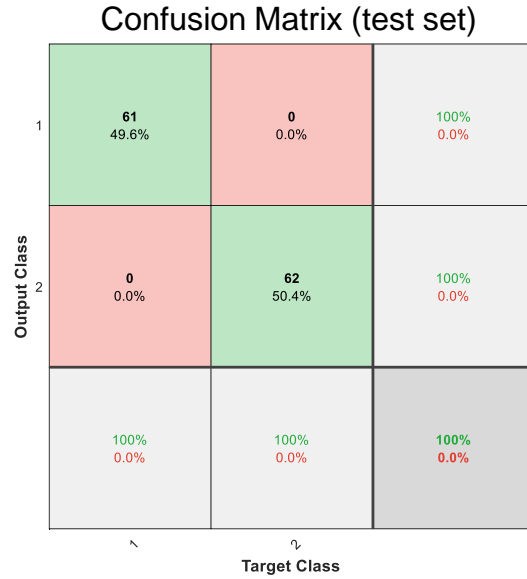


Figure 4.12: Confusion matrix for identifying amplifier and fiber nonlinearities. Impairment identification accuracy of 100% was demonstrated in this scenario.

Next, it is shown that it is possible to measure the level of amplifier nonlinearity in the presence of varying fiber nonlinearity, Fig. 4.13. The amplifier nonlinearities were emulated on experimental data which is also affected by fiber nonlinearities: LP was varied from 2 to 8 dBm in steps of 2 dBm while amplifier nonlinearities varied from 0% clipping to 70% clipping. Clipping estimation accuracy was within  $\pm 3.8\%$  with a maximum clipping estimation discrepancy of  $\pm 11.2\%$ . This is possible due to the discernible characteristics of each as confirmed during impairment identification.

Estimation accuracy was highest for higher clipping values and worse for low clipping, Fig. 4.14(a). This is intuitive as it is difficult to measure the lack of something. Despite this, estimation accuracy is still reasonably accurate for all tested cases. However, there was no reduction in accuracy when varying the fiber nonlinearities, Fig. 4.14(b). This is also expected based on the emulation assumptions where amplifier phase

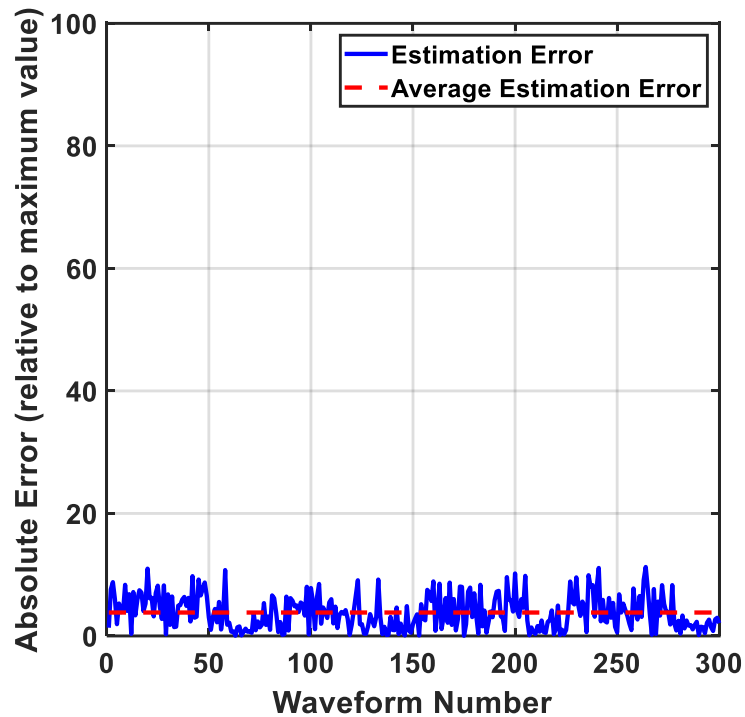


Figure 4.13: Clipping estimation accuracy for constellation-based ML method. Accurate average estimation within  $\pm 3.8\%$  was demonstrated.

effects are ignored and under the assumption that there is no mixing between amplifier and fiber nonlinearities.

Under this simplified proof of concept, amplifier nonlinearities were readily identified and estimated relative to fiber nonlinearities which further demonstrates the efficacy of a trained ML method. However, for example in Section 4.4, without accounting for these amplifier nonlinearities which affects the constellation, the ML model would report a low GOSNR potentially indicating a fiber nonlinearity problem to network operators. Therefore, it is important to always understand and consider the bounds of an ML model with respect to the full system. Ideally, impairment identification

schemes which provide coverage for all likely impairments should be implemented alongside these performance monitoring techniques.

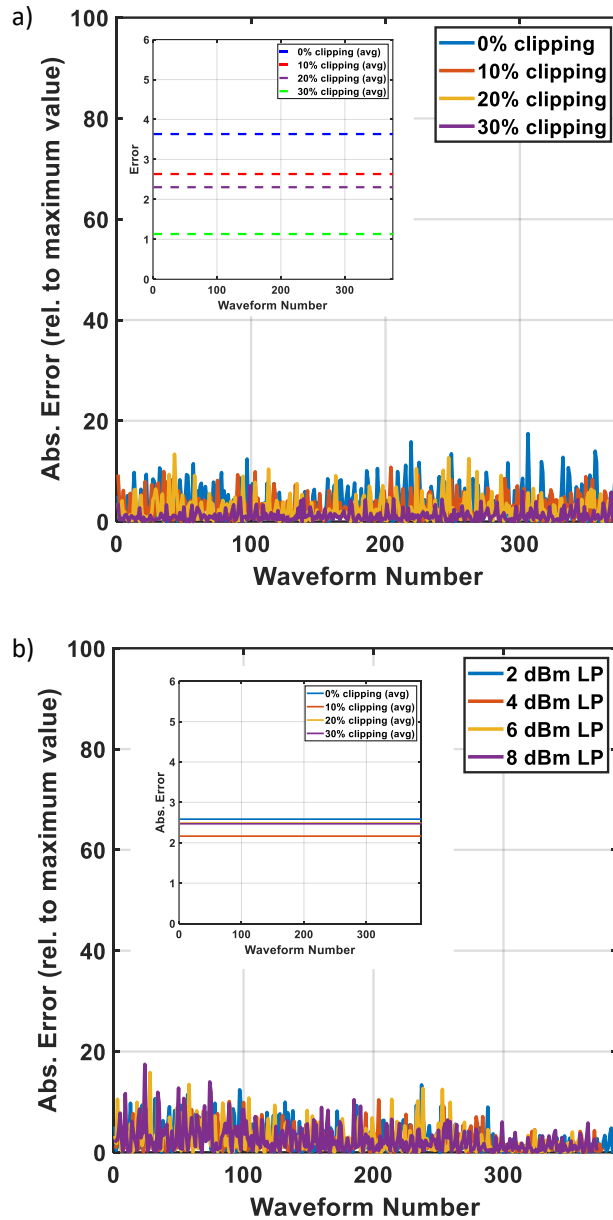


Figure 4.14: (a) Clipping estimation accuracy as a function of varying clipping percentage. Clipping estimation becomes less accurate as clipping decreases. (b) Clipping estimation accuracy as a function of LP. No dependence is shown.

## CONCLUSIONS

The internet has become a fundamental pillar that has revolutionized the way we live, work, and communicate. It serves as an inexhaustible source of information transfer globally. Commercially, it has supported unprecedented economic development and growth via digital markets. Socially, it has connected people across the world in real-time and assisted the exchange of ideas, cultures, and experiences. As the world continues to rely on the internet, the development of the fiber optic infrastructure which supports it is expected to continue as well. This dissertation offered a path forward to solve optical networking monitoring issues which are expected to plague these next generation optical networks while also supplying methodologies to enhance manufacturing processes.

In chapter 3, we introduced a method for accelerating the TDECQ calculation that also doubles as an impairment identification scheme to enable network operators to not only qualify the optical transmitters, but also to pinpoint which issues the transmitters may be having thereby drastically decreasing the necessary troubleshooting when there are product defects. This work resulted in an estimation accuracy within 0.2 dB from TDECQ calculated using the method depicted in the IEEE standard while also reducing the processing time by a factor of 1000 – runtime was reduced from ~55 seconds to ~0.1 seconds. The limits of ML training were explored by observing the potential dependence on specific impairments or even specific equipment used for training. This serves as a framework for future works where other necessary manufacturing measurements may be streamlined, accelerated, and enhanced using ML-based methods.

In chapter 4, we discussed optical performance monitoring techniques with respect to the OSNR and GOSNR of the optical networks. Linear and nonlinear noise are prime considerations for monitoring in these works due to their significant correlation with BER and overall system health. This work demonstrated two methods to predict these metrics using both outputs from conventional DSP as well as directly from the constellation diagram. Accuracy of the CPR-based method was shown to be within 0.45 dB for the OSNR estimation and launch power estimation, which was used as a proxy for the nonlinear noise, was estimated within 0.1 dB. The constellation-based method was tested on a link composed of commercial equipment and trained using limited data to demonstrate a practical application of ML. It was shown that GOSNR estimation can be performed within 0.16 dB while OSNR estimation can be performed with 0.5 dB. Likewise, impairment identification schemes were considered and an example of component-level impairment identification between amplifiers and fiber nonlinearities was demonstrated. Although a simplified example, 100% impairment identification was demonstrated as proof of concept. ML-based methods prove to be promising methods for monitoring next generation optical networks due to the ability to directly derive relationships between optical signals and their associated performance parameters without the need for a physical model. Likewise, methods demonstrated the ability to accurately estimate the extent of the impairment even in the presence of other similar impairments.

To advance the work in this dissertation, it is important to fully characterize the impact of varying impairments on the methodologies presented. ML is heavily dependent on the training data, and thus it is integral to use a complete data set relative to the

application as well as understand the implications of how different system parameters and impairments interact with the expected measurement results to achieve maximum performance. This continuation is applicable to all ML-based approaches. Other works may consider the benefits of employing ensemble techniques where multiple approaches measure the same parameters to achieve either higher accuracy or to alleviate limitations which may exist in certain techniques but not others. Likewise, as ML is often considered a tool which is device-specific, it warrants further study to determine the extent of generalizability these ML approaches may achieve – whether through transfer learning paradigms, or via generalized model development and sufficient training data.

## APPENDIX A. TRANSMITTER AND DISPERSION EYE CLOSURE QUATERNARY

Transmitter and dispersion eye closure quaternary (TDECQ) is a measurement methodology defined by the IEEE 802.3 standard [119]. TDECQ replaces the older PAM-2 procedures such as eye-masks and TDP tests. It is used to qualify optical PAM-4 transmitters in the worst-case scenario where the transmitter, channel, and receiver may all be manufactured by different vendors. TDECQ sets a baseline performance requirement to ensure interoperability between these different components.

TDECQ qualifies the performance of an optical transmitter by iteratively adding noise, denoted  $\sigma_G$ , alongside DSP-based equalization to reach a target SER. This process is shown in Fig. A.1. Note that SER is measured indirectly which avoids the computational burden associated with direct BER counting. Also, the receiver noise, denoted  $\sigma_S$ , is characterized so that it can be abstracted from the TDECQ calculation to

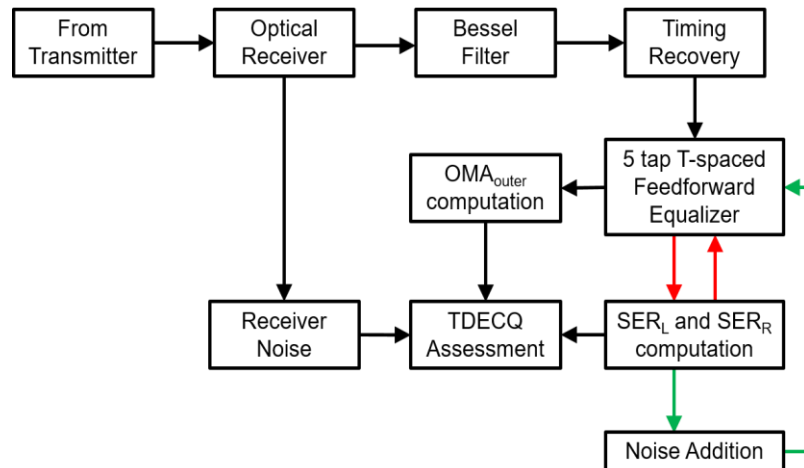


Figure A.1: Algorithmic flow chart for TDECQ measurements. PAM-4 transmitters are qualified relative to the amount of additional noise needed to reach a target SER.

allow for comparison with other transmitters. TDECQ is computed as

$$TDECQ = 10 \log_{10} \left( \frac{OMA}{6Q_t R} \right) \quad (A.1)$$

where  $Q_t = 3.414$ ,  $R = \sqrt{\sigma_s^2 + \sigma_G^2}$ , and OMA is the optical modulation amplitude which is a measure of the difference between the highest and lowest signal amplitude.

The OMA is calculated from the processed signal which undergoes a specific process. The transmitter is loaded with an SSPRQ bit pattern. SSPRQ is based on a truncated PRBS-31 pattern to allow for sufficient transmitter stress during testing while avoiding the need for the full-length pattern [147]. Once the pattern is captured at the receiver, it is filtered using a fourth order Bessel filter which has a bandwidth half the symbol rate. Then, a timing recovery algorithm is used to optimally resample the signal before being equalized by a 5-tap T-spaced feed forward equalizer (FFE). The equalizer tap weights must meet some criteria: the sum of all taps must be equal to 1, the maximum weight tap must occur within the first three taps, and the tap with maximum value should be at least 0.8. Then, two specific sequences of the SSPRQ pattern are identified: 7 consecutive maximum amplitude bits (defined as a value of 3) and 6 consecutive minimum amplitude bits (defined as a value of 0), Fig. A.2. Note that possible amplitude values are 0, 1, 2, and 3 for the PAM-4 signals discussed here. The center symbols of these sequences are then used to calculate the OMA. Note that this process is iterative with respect to the noise addition.

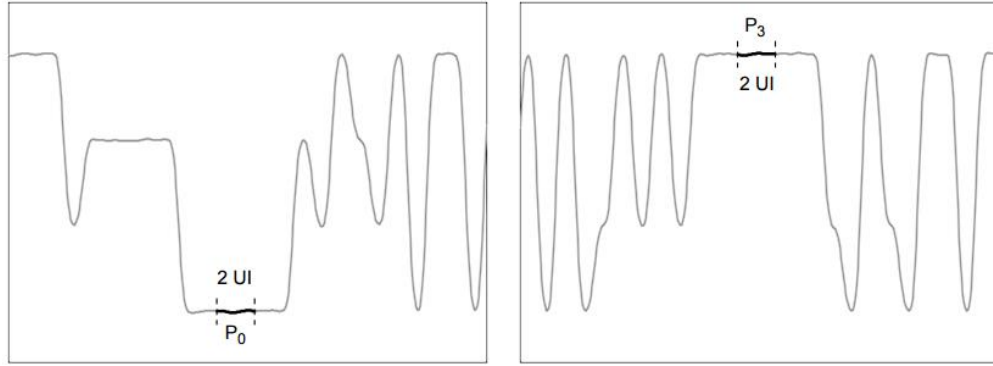


Figure A.2: Example sequences from SSPRQ pattern used to calculate the OMA. The central symbol of each batch is used as the minimum and maximum amplitudes [148].

It is crucial to manage the noise addition to reach the target SER of  $4.8 \times 10^{-4}$  as defined by IEEE standard. After equalization, an eye diagram is generated and centered using the average eye crossing times, Fig. A.3. Two vertical histograms are generated from this eye diagram at unit intervals (UI) of 0.45 and 0.55. Note that one UI is one symbol period. These histograms are used to measure two different SER values:  $SER_L$  and  $SER_R$ . The higher value of the two is chosen as the transmitter SER. Then, as noise is added, the algorithm iteratively optimizes the equalizer tap weights. Once the target SER is reached, the OMA along with added noise variance is used to calculate the TDECQ.

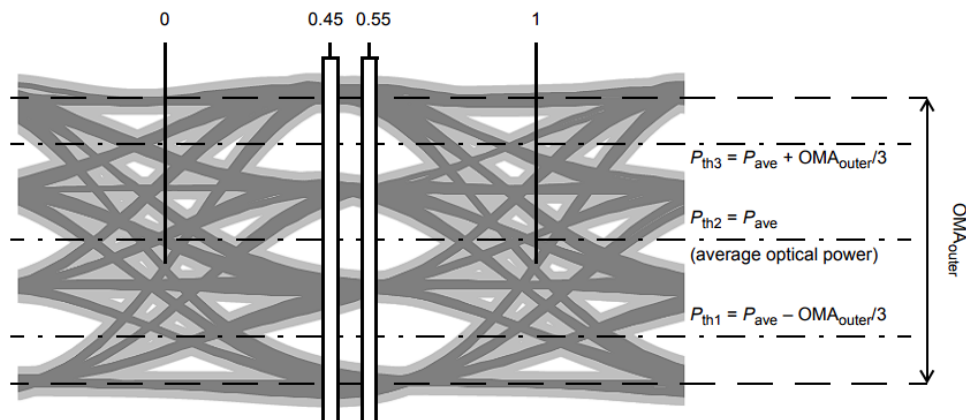


Figure A.3: Example of PAM-4 eye-diagram used to calculate the SER for TDECQ measurements [148]. Important metrics such as left and right histograms are shown.

## REFERENCES

- [1] Cisco Annual Internet Report (20182023) White Paper.
- [2] P. J. Winzer, D. T. Neilson, and A. R. Chraplyvy, "Fiber-optic transmission and networking: The previous 20 and the next 20 years [invited]," *Optics Express*, vol. 26, no. 18, p. 24190, 2018.
- [3] M. D. Al-Amri, M. El-Gomati, and M. S. Zubairy, *Optics in our time*. Cham: Springer International Publishing, 2018.
- [4] "Final telegram to be sent. stop," *The Guardian*, 10-Jul-2013. [Online]. Available: <https://www.theguardian.com/world/shortcuts/2013/jul/10/final-telegram-to-be-sent-india>. [Accessed: 17-Nov-2023]
- [5] A. Schawlow, "Lasers in historical perspective," *IEEE Journal of Quantum Electronics*, vol. 20, no. 6, pp. 558–561, 1984.
- [6] F. P. Kapron, D. B. Keck, and R. D. Maurer, "Radiation losses in glass optical waveguides," *Applied Physics Letters*, vol. 17, no. 10, pp. 423–425, 1970.
- [7] T. Miya, Y. Terunuma, T. Hosaka, and T. Miyashita, "Ultimate low-loss single-mode fibre at 1.55  $\mu\text{m}$ ," *Electronics Letters*, vol. 15, no. 4, p. 106, 1979.
- [8] R. S. Kerdock and D. H. Wolaver, "Atlanta fiber system experiment: results of the Atlanta experiment," in *The Bell System Technical Journal*, vol. 57, no. 6, pp. 1857-1879, July-Aug. 1978.
- [9] Jeff Hecht. City of Light. The Story of Fiber Optics. Oxford University Press, USA, 1999.
- [10] M. I. Schwartz, W. A. Reenstra, J. H. Mullins and J. S. Cook, "Atlanta fiber system experiment: The Chicago lightwave communications project," in *The Bell System Technical Journal*, vol. 57, no. 6, pp. 1881-1888, July-Aug. 1978.
- [11] R. Berry, D. Brace, and I. Ravenscroft. "Optical Fiber System Trials at 8 Mbits/s and 140 Mbits/s". In: *IEEE Transactions on Communications* 26.7 (1978), pp. 1020– 1027
- [12] Erik Agrell et al. "Roadmap on Optical Communications". In: *Journal of Optics* 18 (May 2016).
- [13] ITU-T G.655. *Characteristics of a non-zero dispersion-shifted single-mode optical fibre and cable*. [www.itu.int/rec/T-REC-G.655-200911-I/en](http://www.itu.int/rec/T-REC-G.655-200911-I/en). 2009.

- [14] A. R. Chraplyvy, A. H. Gnauck, R. W. Tkach and R. M. Derosier, "8\*10 Gb/s transmission through 280 km of dispersion-managed fiber," in *IEEE Photonics Technology Letters*, vol. 5, no. 10, pp. 1233-1235, Oct. 1993.
- [15] A. M. Vengsarkar et al. "Fundamental-mode dispersion-compensating fibers: design considerations and experiments". In: *Conference on Optical Fiber Communication*. Optical Society of America, 1994, ThK2.
- [16] A. M. Vengsarkar, A. E. Miller, and W. A. Reed. "Highly efficient single-mode fiber for broadband dispersion compensation". In: *Conference on Optical Fiber Communication/International Conference on Integrated Optics and Optical Fiber Communication*. Optical Society of America, 1993, PD13.
- [17] R. J. Essiambre, P. J. Winzer, and D. Grosz. "Impact of DCF properties on system design". In: *J Optic Comm* 3 (2006), pp. 221–291.
- [18] P. J. Winzer and R. J. Essiambre. "Advanced Optical Modulation Formats". In: *Proceedings of the IEEE* 94.5 (2006), pp. 952–985.
- [19] M. Nakazawa, K. Kikuchi, and T. Miyazaki, *High spectral density optical communication technologies*. Berlin: Springer Berlin, 2013.
- [20] K. Kikuchi, "Fundamentals of Coherent Optical Fiber Communications," *Journal of Lightwave Technology*, vol. 34, no. 1, pp. 157–179, 2016.
- [21] D. McGhan, C. Laperle, A. Savehenko, Chuandong Li, G. Mak and M. O'Sullivan, "5120 km RZ-DPSK transmission over G652 fiber at 10 Gb/s with no optical dispersion compensation," *OFC/NFOEC Technical Digest. Optical Fiber Communication Conference*, Anaheim, CA, pp. 3 pp. Vol. 5, 2005.
- [22] A. Splett, C. Kurtzke, and K. Petermann, "Ultimate transmission capacity of amplified optical fiber communication systems taking into account fiber nonlinearities," *Proc. European Conf. on Optical Comm. (ECOC)*, MoC2.4 (1993)
- [23] P. Poggiolini, G. Bosco, A. Carena, V. Curri, Y. Jiang, and F. Forghieri, "The GN model of fiber non-linear propagation and its applications," *J. Lightwave Technol.* 32(4), 694–721 (2014).
- [24] A. Carena, G. Bosco, V. Curri, Y. Jiang, P. Poggiolini, and F. Forghieri, "EGN model of non-linear fiber propagation," *Opt. Express* 22(13), 16335–16362 (2014).
- [25] R. Dar, M. Feder, A. Mecozzi, and M. Shtaif, "Accumulation of nonlinear interference noise in fiber-optic systems," *Opt. Express* 22(12), 14199–14211 (2014).

- [26] Q. Zhuge *et al.*, "Application of Machine Learning in Fiber Nonlinearity Modeling and Monitoring for Elastic Optical Networks," in *Journal of Lightwave Technology*, vol. 37, no. 13, pp. 3055-3063, 2019.
- [27] Y. Pointurier, "Machine learning techniques for quality of transmission estimation in optical networks," in *Journal of Optical Communications and Networking*, vol. 13, no. 4, pp. B60-B71, April 2021
- [28] S. Beppu, K. Kasai, M. Yoshida and M. Nakazawa, "2048 QAM (66 Gbit/s) single-carrier coherent optical transmission over 150 km with a potential SE of 15.3 bit/s/Hz," *OFC 2014*, San Francisco, CA, USA, 2014, W1A.6.
- [29] T. Okoshi and K. Kikuchi. *Coherent Optical Fiber Communications*. Springer, 1988.
- [30] K. Schuh *et al.* "15.4 Tb/s transmission over 2400 km using polarization multiplexed 32-Gbaud 16-QAM modulation and coherent detection comprising digital signal processing". In: *2011 37th European Conference and Exhibition on Optical Communication*. 2011, pp. 1–3.
- [31] P. J. Winzer *et al.* "56-Gbaud PDM-QPSK: coherent detection and 2,500-km transmission". In: *2009 35th European Conference on Optical Communication*. 2009, pp. 1–2.
- [32] G. Raybon *et al.* "Single-carrier all-ETDM 1.08-Terabit/s line rate PDM-64-QAM transmitter using a high-speed 3-bit multiplexing DAC". In: *2015 IEEE Photonics Conference (IPC)*. 2015, pp. 1–2.
- [33] A. Ghazisaeidi *et al.* "Advanced C+L-Band Transoceanic Transmission Systems Based on Probabilistically Shaped PDM-64QAM". In: *Journal of Lightwave Technology* 35.7 (2017), pp. 1291–1299.
- [34] "IEEE Standard for Digitizing Waveform Recorders," in *IEEE Std 1057-2017 (Revision of IEEE Std 1057-2007)*, 26 Jan. 2018.
- [35] A. Yariv, P.E.E.A. Yariv, and P. Yeh. *Photonics: Optical Electronics in Modern Communications*. Oxford series in electrical and computer engineering. Oxford University Press, 2007.
- [36] Govind P. Agarwal. *Fiber-Optic Communication Systems*. Wiley, 2010.
- [37] D. Gloge. "Weakly Guiding Fibers". In: *Appl. Opt.* 10.10 (1971), pp. 2252–2258.
- [38] P. S. Henry and S. D. Personick, Eds., *Coherent Lightwave Communications*, IEEE Press, Piscataway, NJ, 1990.

- [39] D. Marcuse. "Gaussian approximation of the fundamental modes of graded-index fibers". In: *J. Opt. Soc. Am.* 68.1 (1978), pp. 103–109.
- [40] Max Born et al. *Principles of Optics: Electromagnetic Theory of Propagation, Interference and Diffraction of Light*. 7th ed. Cambridge University Press, 1999
- [41] Yoshiaki Tamura et al. "Lowest-Ever 0.1419-dB/km Loss Optical Fiber". In: *Optical Fiber Communication Conference Postdeadline Papers*. Optical Society of America, 2017, Th5D.1.
- [42] John A. Buck. *Fundamentals of Optical Fiber*. Wiley, 2004.
- [43] R. Ramaswami, K. N. Sivarajan, and G. H. Sasaki. *Optical Networks: A Practical Perspective*. Morgan Kaufmann, 2010.
- [44] G. P. Agrawal, *Nonlinear Fiber Optics*, 3rd ed., Academic Press, San Diego, CA, 2001.
- [45] C. R. Menyuk, "Polarization mode dispersion in optical communication systems," *Conference on Lasers and Electro-Optics (CLEO 2000). Technical Digest. Postconference Edition. TOPS Vol.39 (IEEE Cat. No.00CH37088)*, San Francisco, CA, USA, 2000.
- [46] A. Mecozzi and M. Shtaif, "Polarization dependent loss and its impact in optical communications systems," *Optical Fiber Communication Conference, 2004*.
- [47] M. R. Phillips, S. L. Woodward and R. L. Smith, "Cross-Polarization Modulation: Theory and Measurement in Subcarrier-Modulated WDM Systems," in *Journal of Lightwave Technology*, vol. 24, no. 11, pp. 4089-4099, Nov. 2006.
- [48] G. R. Walker, R. C. Steele, and N. G. Walker. "Optical amplifier noise figure in a coherent optical transmission system". In: *Journal of Lightwave Technology* 8.9 (1990), pp. 1409–1413.
- [49] R. Essiambre et al. "Capacity Limits of Optical Fiber Networks". In: *Journal of Lightwave Technology* 28.4 (2010), pp. 662–701.
- [50] "IEEE Draft Standard for Ethernet Amendment: Physical Layers and Management Parameters for 50 Gb/s, 200 Gb/s, and 400 Gb/s Operation over Single-Mode Fiber". In: *IEEE P802.3cn/D3.0, July 2019* (2019), pp. 1–87.
- [51] D. T. Neilson et al. "Wavelength selective switching for optical bandwidth management". In: *Bell Labs Technical Journal* 11.2 (2006), pp. 105–128.
- [52] M. Filer and S. Tibuleac. "Generalized weighted crosstalk for DWDM systems with cascaded wavelength-selective switches". In: *OFC/NFOEC*. 2012, pp. 1–3.

- [53] Kasap S. O. *Optoelectronics and Photonics: Principles and Practices*. Prentice Hall 2001.
- [54] S. Kumar and M. Jamal Deen. *Fiber Optic Communications: Fundamentals and Applications*. Wiley, 2014.
- [55] S. T. Le, V. Aref and J. Cho, "Single-Ended Coherent Receiver," in *Journal of Lightwave Technology*, vol. 40, no. 5, pp. 1382-1399, 2022.
- [56] Gengchen Liu et al. "Demonstration of a carrier frequency offset estimator for 16-/32-QAM coherent receivers: a hardware perspective". In: *Opt. Express* 26.4 (2018), pp. 4853–4862.
- [57] W. R. Peng, I. Morita, H. Tanaka, "Hybrid QAM Transmission Techniques for Single-Carrier Ultra-Dense WDM Systems," *Proc. Opto-Electron. Commun. Conf.*, Kaohsiung, pp. 824-825, 2011.
- [58] D. Welch, A. Napoli, J. Back, W. Sande, J. Pedro, F. Masoud, C. Fludger, T. Duthel, H. Sun, S. J. Hand, T.-K. Chiang, A. Chase, A. Mathur, T. A. Eriksson, M. Plantare, M. Olson, S. Voll, and K.-T. Wu, "Point-to-multipoint optical networks using coherent digital subcarriers," *Journal of Lightwave Technology*, vol. 39, no. 16, pp. 5232–5247, 2021.
- [59] Tao Liu and Ivan B. Djordjevic. "Optimal signal constellation design for ultra-high-speed optical transport in the presence of nonlinear phase noise". In: *Opt. Express* 22.26 (2014), pp. 32188–32198.
- [60] Lotfollah Beygi, Erik Agrell, and Magnus Karlsson. "Optimization of 16-point Ring Constellations in the Presence of Nonlinear Phase Noise". In: *Optical Fiber Communication Conference/National Fiber Optic Engineers Conference 2011*. Optical Society of America, 2011, OThO4.
- [61] Fred Buchali et al. "Rate Adaptation and Reach Increase by Probabilistically Shaped 64-QAM: An Experimental Demonstration". In: *Journal of Lightwave Technology* (Dec. 2015).
- [62] P. Schulte and G. Bcherer. "Constant Composition Distribution Matching". In: *IEEE Transactions on Information Theory* 62.1 (2016), pp. 430–434.
- [63] J. Fickers, A. Ghazisaeidi, M. Salsi, G. Charlet, F. Horlin, P. Emplit, and S. Bigo, "Design rules for pulse shaping in PDM QPSK and PDM 16QAM Nyquist WDM 33 coherent optical transmission systems," *European Conference and Exhibition on Optical Communication*, 2012.

- [64] K. Roberts, Chuandong Li, L. Strawczynski, M. O'Sullivan, and I. Hardcastle, "Electronic precompensation of optical nonlinearity," *IEEE Photonics Technology Letters*, vol. 18, no. 2, pp. 403–405, 2006.
- [65] M. S. Faruk and S. J. Savory, "Digital signal processing for coherent transceivers employing multilevel formats," *Journal of Lightwave Technology*, vol. 35, no. 5, pp. 1125–1141, 2017.
- [66] T. Xu, G. Jacobsen, S. Popov, J. Li, E. Vanin, K. Wang, A. T. Friberg, and Y. Zhang, "Chromatic dispersion compensation in coherent transmission system using digital filters," *Opt. Express* **18**, 16243-16257 (2010).
- [67] T. Xu, G. Jacobsen, S. Popov, M. Forzati, J. Martensson, M. Mussolin, J. Li, K. Wang, Y. Zhang, A. T. Friberg, "Frequency-Domain Chromatic Dispersion Equalization Using Overlap-Add Methods in Coherent Optical System," in *J. Opt. Commun.* 32 (2011), pp. 131-135.
- [68] F. Gardner, "A BPSK/QPSK Timing-Error Detector for Sampled Receivers," in *IEEE Transactions on Communications*, vol. 34, no. 5, pp. 423-429, May 1986.
- [69] J. D. H. Alexander, "Clock recovery from random binary signals" in *Electronics Letters*, vol. 11, pp. 541-542, 1975.
- [70] K. Mueller and M. Muller, "Timing Recovery in Digital Synchronous Data Receivers," in *IEEE Transactions on Communications*, vol. 24, no. 5, pp. 516-531, May 1976.
- [71] D. Godard, "Passband Timing Recovery in an All-Digital Modem Receiver," in *IEEE Transactions on Communications*, vol. 26, no. 5, pp. 517-523, May 1978.
- [72] M. Oerder and H. Meyr, "Digital filter and square timing recovery," in *IEEE Transactions on Communications*, vol. 36, no. 5, pp. 605-612, May 1988.
- [73] Y. Ainhoren, S. Engelberg and S. Friedman, "The cocktail party problem [instrumentation notes]," in *IEEE Instrumentation & Measurement Magazine*, vol. 11, no. 3, pp. 44-48, June 2008.
- [74] J.G. Proakis. *Digital Communications*. McGraw-Hill series in electrical and computer engineering: communications and signal processing. McGraw-Hill, 2001. ISBN: 9780071181839.
- [75] K. Kikuchi, "Polarization-demultiplexing algorithm in the digital coherent receiver," *2008 Digest of the IEEE/LEOS Summer Topical Meetings*, Acapulco, Mexico, 2008, pp. 101-102.

- [76] C. Yuxin et al. "Mode demultiplexing based on multimodulus blind equalization algorithm". In: *Optics Communications* 324 (2014), pp. 311–317.
- [77] K. Kikuchi, "Performance analyses of polarization demultiplexing based on constant-modulus algorithm in digital coherent optical receivers," *Opt. Express* 19, 9868-9880 (2011).
- [78] S. S. Haykin. *Unsupervised Adaptive Filtering: Blind source separation*. Wiley-Interscience publication. Wiley, 2000.
- [79] H. Zhang, Z. Tao, L. Liu, S. Oda, T. Hoshida and J. C. Rasmussen, "Polarization demultiplexing based on independent component analysis in optical coherent receivers," *2008 34th European Conference on Optical Communication*, Brussels, Belgium, 2008, pp. 1-2.
- [80] P. Johannisson et al. "Convergence Comparison of the CMA and ICA for Blind Polarization Demultiplexing". In: *IEEE/OSA Journal of Optical Communications and Networking* 3.6 (2011), pp. 493–501.
- [81] A. Leven et al. "Frequency Estimation in Intradynne Reception". In: *IEEE Photonics Technology Letters* 19.6 (2007), pp. 366–368.
- [82] A. Tarighat et al. "Digital adaptive phase noise reduction in coherent optical links". In: *Journal of Lightwave Technology* 24.3 (2006), pp. 1269–1276
- [83] B. Widrow, J. McCool, and M. Ball. "The complex LMS algorithm". In: *Proceedings of the IEEE* 63.4 (1975), pp. 719–720.
- [84] E. Ip and J. M. Kahn. "Compensation of Dispersion and Nonlinear Impairments Using Digital Backpropagation". In: *Journal of Lightwave Technology* 26.20 (2008), pp. 3416–3425.
- [85] T. Liu, Y. Wang and J. Zhou, "A Machine Learning Method for Fiber Nonlinear Compensation," *2020 Chinese Automation Congress (CAC)*, Shanghai, China, 2020, pp. 3708-3711.
- [85] T. Liu, Y. Wang and J. Zhou, "A Machine Learning Method for Fiber Nonlinear Compensation," *2020 Chinese Automation Congress (CAC)*, Shanghai, China, 2020, pp. 3708-3711.
- [86] C. Häger, H. D. Pfister, R. M. Büttler, G. Liga and A. Alvarado, "Revisiting multi-step nonlinearity compensation with machine learning," *45th European Conference on Optical Communication (ECOC 2019)*, Dublin, Ireland, 2019, pp. 1-4.

- [87] E. Giacomidis, A. Matin, J. Wei, N. J. Doran, L. P. Barry and X. Wang, "Blind Nonlinearity Equalization by Machine-Learning-Based Clustering for Single- and Multichannel Coherent Optical OFDM," in *Journal of Lightwave Technology*, vol. 36, no. 3, pp. 721-727, 2018.
- [88] X. Lin *et al.*, "Perturbation Theory-Aided Learned Digital Back-Propagation Scheme for Optical Fiber Nonlinearity Compensation," in *Journal of Lightwave Technology*, vol. 40, no. 7, pp. 1981-1988, 2022.
- [89] Z. Yuan and X. Zhao, "Introduction of forward error correction and its application," *2012 2nd International Conference on Consumer Electronics, Communications and Networks (CECNet)*, Yichang, China, 2012, pp. 3288-3291.
- [90] W.S. McCulloch and W Pitts. "A logical calculus of the ideas immanent in nervous activity". In: *Bulletin of Mathematical Biophysics* 5 (Dec. 1943).
- [91] M. Minsky and S.A Papert. *Perceptrons*. Jan. 1969. ISBN: 9780262130431
- [92] A. L. Fradkov, "Early History of Machine Learning," In: *International Federation of Automatic Control*, vol. 53, iss. 2, pp. 1385-1390, 2020.
- [93] Rumelhart, D., Hinton, G. & Williams, R. *Learning representations by back-propagating errors. Nature* **323**, 533–536 (1986).
- [94] Jeffrey Dean and Sanjay Ghemawat. 2008. *MapReduce: simplified data processing on large clusters*. *Commun. ACM* 51, 1 (January 2008), 107–113.
- [95] F. N. Khan, Q. Fan, C. Lu and A. P. T. Lau, "Machine Learning-Assisted Optical Performance Monitoring in Fiber-Optic Networks," *2018 IEEE Photonics Society Summer Topical Meeting Series (SUM)*, Waikoloa, HI, USA, 2018, pp. 53-54.
- [96] W. S. Saif, M. A. Esmail, A. M. Ragheb, T. A. Alshawi and S. A. Alshebeili, "Machine Learning Techniques for Optical Performance Monitoring and Modulation Format Identification: A Survey," in *IEEE Communications Surveys & Tutorials*, vol. 22, no. 4, pp. 2839-2882, 2020.
- [97] F. N. Khan, C. Lu and A. P. T. Lau, "Optical Performance Monitoring in Fiber-Optic Networks Enabled by Machine Learning Techniques," *2018 Optical Fiber Communications Conference and Exposition (OFC)*, San Diego, CA, USA, 2018, pp. 1-3.
- [98] S. Varughese, D. Lippiatt, T. Richter, S. Tibuleac and S. E. Ralph, "Identification of Soft Failures in Optical Links using Low Complexity Anomaly Detection," *2019 Optical Fiber Communications Conference and Exhibition (OFC)*, San Diego, CA, USA, 2019, pp. 1-3.

- [99] T. B. Anderson, A.0 Kowalczyk, K. Clarke, S. D. Dods, D. Hewitt, and J. C. Li, "Multi Impairment Monitoring for Optical Networks," *J. Lightwave Technol.* **27**, 3729-3736 (2009).
- [100] H. Lun *et al.*, "A GAN Based Soft Failure Detection and Identification Framework for Long-Haul Coherent Optical Communication Systems," in *Journal of Lightwave Technology*, vol. 41, no. 8, pp. 2312-2322, 2023.
- [101] Ma, W., Liu, Z., Kudyshev, Z.A. *et al.* Deep learning for the design of photonic structures. *Nat. Photonics* **15**, 77–90 (2021).
- [102] Z. Liu, D. Zhu, L. Raju, and W. Cai, "Tackling Photonic Inverse Design with Machine Learning," In: *Advanced Science*, vol. 8, no. 5, 2021.
- [103] E. Wong and L. Ruan, "Towards 6G: Machine Learning Driven Resource Allocation in Next Generation Optical Access Networks (Invited)," *2022 European Conference on Optical Communication (ECOC)*, Basel, Switzerland, 2022, pp. 1-3.
- [104] S. K. Singh and A. Jukan, "Machine-learning-based prediction for resource (Re)allocation in optical data center networks," in *Journal of Optical Communications and Networking*, vol. 10, no. 10, pp. D12-D28, Oct. 2018.
- [105] T.M Mitchell. *Machine Learning*. 1997. ISBN: 0-07-115467-1.
- [106] Karl Pearson F.R.S. "LIII. On lines and planes of closest fit to systems of points in space". In: *The London, Edinburgh, and Dublin Philosophical Magazine and Journal of Science* **2.11** (1901), pp. 559–572.
- [107] V.N. Vapnik and A.Y. Chervonenkis. "On the uniform convergence of relative frequencies of events to their probabilities". In: *Measures of Complexity*, Jan. 2015, pp. 11–30.
- [108] Ian Goodfellow, Yoshua Bengio, and Aaron Courville. *Deep Learning*. [www.deeplearningbook.org](http://www.deeplearningbook.org). MIT Press, 2016.
- [109] Bernhard E. Boser, Isabelle M. Guyon, and Vladimir N. Vapnik. "A Training Algorithm for Optimal Margin Classifiers". In: *Proceedings of the Fifth Annual Workshop on Computational Learning Theory. COLT 92*. Pittsburgh, Pennsylvania, USA: Association for Computing Machinery, 1992.
- [110] C.M. Bishop. *Pattern Recognition and Machine Learning*. Information science and statistics. Springer (India) Private Limited, 2013.
- [111] Rasmussen, Carl E. and Christopher K. I. Williams. "Gaussian processes for machine learning." *Adaptive computation and machine learning* (2005).

- [112] Hofmann, Thomas et al. "Kernel methods in machine learning." *Annals of Statistics* 36 (2007): 1171-1220.1
- [113] Yann Lecun. "Generalization and network design strategies". In: *Connectionism in perspective*. Ed. by R. Pfeifer et al. Elsevier, 1989.
- [114] Alex Graves et al. *A Novel Connectionist System for Unconstrained Handwriting Recognition*. 2008.
- [115] Justin Lavrencik et al. "168Gbps PAM-4 Multimode Fiber Transmission through 50m using 28GHz 850nm Multimode VCSELs". In: *Optical Fiber Communication Conference (OFC) 2020*. Optical Society of America, 2020, W1D.3.
- [116] H. Yu et al. "400Gbps Fully Integrated DR4 Silicon Photonics Transmitter for Data Center Applications". In: *Optical Fiber Communication Conference (OFC) 2020*. Optical Society of America, 2020, T3H.6.
- [117] IEEE 802.3bs –IEEE Draft Standard for Ethernet Amendment 10: Media Access Control Parameters, Physical Layers and Management Parameters for 200 Gb/s and 400 Gb/s Operation.
- [118] IEEE 802.3cd/D3.5, Sept 2018 –IEEE Approved Draft Standard for Ethernet Amendment: Media Access Control Parameters for 50 Gb/s and Physical Layers and Management Parameters for 50 Gb/s, 100 Gb/s, and 200 Gb/s Operation.
- [119] J. King, D. Leyba and G. D. LeCheminant, "TDECQ (transmitter dispersion eye closure quaternary) replaces historic eye-mask and TDP test for 400 Gb/s PAM4 optical transmitters," *2017 Optical Fiber Communications Conference and Exhibition (OFC)*, Los Angeles, CA, USA, 2017, pp. 1-3.
- [120] S. Varughese *et al.*, "Accelerating TDECQ Assessments using Convolutional Neural Networks," *2020 Optical Fiber Communications Conference and Exhibition (OFC)*, San Diego, CA, USA, 2020, pp. 1-3.
- [121] S. Varughese, A. Melgar, V. A. Thomas, P. Zivny, S. Hazzard and S. E. Ralph, "Accelerating Assessments of Optical Components Using Machine Learning: TDECQ as Demonstrated Example," in *Journal of Lightwave Technology*, vol. 39, no. 1, pp. 64-72, 2021.
- [122] Jiuxiang Gu, Zhenhua Wang, Jason Kuen, Lianyang Ma, Amir Shahroudy, Bing Shuai, Ting Liu, Xingxing Wang, Gang Wang, Jianfei Cai, and Tsuhan Chen. 2018. Recent advances in convolutional neural networks. *Pattern Recogn.* 77, C (May 2018).

- [123] Acacia Communications Inc. (Maynard, MA), "Optical signal-to-noise ratio (OSNR) monitoring and measurement in optical communication systems," 0365165, 2015.
- [124] Zhenhua Dong, Alan Pak Tao Lau, and Chao Lu, "OSNR monitoring for QPSK and 16-QAM systems in presence of fiber nonlinearities for digital coherent receivers," *Opt. Express* 20, 19520-19534 (2012)
- [125] B. Nebendahl *et al.*, "Quality Metrics in optical modulation analysis: EVM and its relation to Q-factor, OSNR, and BER," *2012 Asia Communications and Photonics Conference (ACP)*, Guangzhou, China, 2012, pp. 1-3.
- [126] S. J. Savory and F. J. V. Caballero, "Machine Learning Based Noise Estimation in Optical Fiber Communication Networks," *2018 IEEE Photonics Society Summer Topical Meeting Series (SUM)*, Waikoloa, HI, USA, 2018, pp. 57-58.
- [127] A. Salehiomran, G. Gao and Z. Jiang, "Linear and nonlinear noise monitoring in coherent systems using fast BER measurement and neural networks," *45th European Conference on Optical Communication (ECOC 2019)*, Dublin, Ireland, 2019, pp. 1-3.
- [128] D. Wang *et al.*, "Convolutional Neural Network-Based Deep Learning for Intelligent OSNR Estimation on Eye Diagrams," *2017 European Conference on Optical Communication (ECOC)*, Gothenburg, Sweden, 2017, pp. 1-3.
- [129] M. Al-Nahhal, I. Al-Nahhal, O. A. Dobre, X. Lin, D. Chang and C. Li, "Joint Estimation of Linear and Nonlinear Coherent Optical Fiber Signal-to-Noise Ratio," in *IEEE Photonics Technology Letters*, vol. 35, no. 1, pp. 23-26, 2023.
- [130] H. Lun *et al.*, "Soft Failure Identification for Long-haul Optical Communication Systems Based on One-dimensional Convolutional Neural Network," in *Journal of Lightwave Technology*, vol. 38, no. 11, pp. 2992-2999, 2020.
- [131] M. Mayrock and H. Haunstein, "Impairment Identification in an Optical Transparent Network Using OFDM Transmission," *2008 ITG Symposium on Photonic Networks*, Leipzig, Germany, 2008, pp. 1-5.
- [132] Y. Xu *et al.*, "Deep Transfer Learning Based Multi-impairment Diagnosis for PAM-4 Optical Communication Systems," *2019 18th International Conference on Optical Communications and Networks (ICOON)*, Huangshan, China, 2019.
- [133] S. Varughese, D. Lippiatt, T. Richter, S. Tibuleac and S. E. Ralph, "Low Complexity Soft Failure Detection and Identification in Optical Links using Adaptive Filter Coefficients," *2020 Optical Fiber Communications Conference and Exhibition (OFC)*, San Diego, CA, USA, 2020, pp. 1-3.

- [134] A. Jedidi and M. Abid, "Optimal crosstalk monitoring and identification method for All-Optical Networks," *2009 IFIP International Conference on Wireless and Optical Communications Networks*, Cairo, Egypt, 2009, pp. 1-5.
- [135] Mas, Carmen et al. "Fault localization for optical networks." In: *Photonics East-All-optical networking: architecture, control and management*, pp. 408-419, 1998.
- [136] H. Lun *et al.*, "ROADM-Induced Anomaly Localization and Evaluation for Optical Links Based on Receiver DSP and ML," in *Journal of Lightwave Technology*, vol. 39, no. 9, pp. 2696-2703, 2021.
- [137] Z. Li, Y. Zhao, Y. Li, S. Rahman, X. Yu and J. Zhang, "Demonstration of Fault Localization in Optical Networks Based on Knowledge Graph and Graph Neural Network," *2020 Optical Fiber Communications Conference and Exhibition (OFC)*, San Diego, CA, USA, 2020, pp. 1-3.
- [138] Z. Li *et al.*, "Fault Localization based on Knowledge Graph in Software-Defined Optical Networks," in *Journal of Lightwave Technology*, vol. 39, no. 13, pp. 4236-4246, 2021.
- [139] S. K. Orappanpara Soman, A. Amari, O. A. Dobre and R. Venkatesan, "Second-Order Perturbation Theory-Based Digital Predistortion for Fiber Nonlinearity Compensation," in *Journal of Lightwave Technology*, vol. 39, no. 17, pp. 5474-5485, 2021.
- [140] C. Lin *et al.*, "Adaptive digital back-propagation for optical communication systems," *OFC 2014*, San Francisco, CA, USA, 2014, pp. 1-3.
- [141] H. Ghozlan and G. Kramer, "Models and Information Rates for Wiener Phase Noise Channels," in *IEEE Transactions on Information Theory*, vol. 63, no. 4, pp. 2376-2393, 2017.
- [142] R. Tkach and A. Chraplyvy, "Phase noise and linewidth in an InGaAsP DFB laser," in *Journal of Lightwave Technology*, vol. 4, no. 11, pp. 1711-1716, 1986.
- [143] S. Varughese, J. Langston, V. A. Thomas, S. Tibuleac and S. E. Ralph, "Frequency Dependent ENoB Requirements for M-QAM Optical Links: An Analysis Using an Improved Digital to Analog Converter Model," in *Journal of Lightwave Technology*, vol. 36, no. 18, pp. 4082-4089, 2018.
- [144] T. Richter, J. Pan and S. Tibuleac, "Comparison of WDM Bandwidth Loading Using Individual Transponders, Shaped, and Flat ASE Noise," *2018 Optical Fiber Communications Conference and Exposition (OFC)*, San Diego, CA, USA, 2018, pp. 1-3.

- [145] S. Searcy, T. Richter and S. Tibuleac, "Experimental Study of Bandwidth Loading with Modulated Signals vs. ASE Noise in 400ZR Single-Span Transmission," *2022 Optical Fiber Communications Conference and Exhibition (OFC)*, San Diego, CA, USA, 2022, pp. 1-3.
- [146] H. J. Cho, S. Varughese, D. Lippiatt, R. DeSalvo, S. Tibuleac, and S. E. Ralph, "Optical performance monitoring using digital coherent receivers and convolutional neural networks," *Opt. Express* 28, 32087-32104 (2020).
- [147] SSPRQ test pattern. [http://www.ieee802.org/3/bs/public/adhoc/smf/16\\_04\\_19/anslow\\_01\\_0416\\_smf.pdf](http://www.ieee802.org/3/bs/public/adhoc/smf/16_04_19/anslow_01_0416_smf.pdf).
- [148] "IEEE Standard for Ethernet - Amendment 10: Media Access Control Parameters, Physical Layers, and Management Parameters for 200 Gb/s and 400 Gb/s Operation". In: *IEEE Std 802.3bs-2017 (Amendment to IEEE 802.3-2015 as amended by IEEE's 802.3bw-2015, 802.3by-2016, 802.3bq-2016, 802.3bp-2016, 802.3br-2016, 802.3bn-2016, 802.3bz-2016, 802.3bu-2016, 802.3bv-2017, and IEEE 802.3- 2015/Cor1-2017)*, (2017), pp. 1–372.